The development of undoped alkaline silicate and doped alkaline aluminate phosphors for white phosphorescence, dosimetry, and Persistent luminescence applications

by

Manaka Mmakgabo Colen

submitted in accordance with the requirements for

the degree of

Doctor of Philosophy

In

Physics

At the

University of South Africa

Supervisor: Prof M.S Dhlamini

Co-supervisor: Prof B.M Mothudi

March 2022

DECLARATION

Name: Manaka Mmakgabo Colen

Student number: 49131257

Degree: PhD (Physics)

Exact wording of the title of the thesis as appearing on the electronic copy submitted for examination:

The development of undoped alkaline silicate and doped alkaline aluminate phosphors for white phosphorescence and Persistent luminescence applications

I declare that the above thesis is my own work and that all the sources that I have used or quoted have been indicated and acknowledged by means of complete REFERENCES.

I further declare that I submitted the thesis to originality checking software and that it falls within the accepted requirements for originality.

I further declare that I have not previously submitted this work, or part of it, for examination at Unisa for another qualification or at any other higher education institution.

(The thesis will not be examined unless this statement has been submitted.)

_____ ____27/05/2022_____

SIGNATURE DATE

ACKNOWLEDGEMENTS

- Above all, I forward my gratitude to my God, for all the strength he provided me throughout the duration of this work.
- I am immensely greateful to my supervisor Prof M.S Dhlamini for the exceptional supervision, guidance, and support throughout the course of my research.
- I am very appreciative of my parents, brothers and sisters for the encouragement and moral support they showed to me throughout this work.
- I am very appreciative of Unisa Student Funding for funding this research.
- I would also like to express my acknowledge and appreciation for all the suggestions that contributed to the success of this work from my fellow researchers.
- I also thank Prof Chithambo and his students for introducing me to the TL system and helping me with the TL measurements at the Rhodes University.

ABSTRACT

The undoped $SrSiO_3/SiO_2$ phosphors prepared by both co-precipitation and hydrothermal methods at different Sr/Si molar ratios are reported. Undoped and Mn doped $BaAl_2O_4$ phosphor synthesized using combustion method are also reported. The X-ray diffraction measurements confirmed hexagonal phases of the $SrSiO_3$, SiO_2 and $BaAl_2O_4$:Mn in the prepared phosphors. The particle morphology of the prepared phosphors was observed to be somewhat agglomerated partcles in the alkaline silicate phosphors, whereas nano-sheets with uneven morphology with both nano-rods and hexagonal particles were observed in the $BaAl_2O_4$:Mn phosphor. EDS measurements confirmed the presence of Sr, Si, and O in the $SrSiO_3/SiO_2$ phosphors, together with their homogenous dispersion in the phosphors. The presence of Ba, Al, O, and Mn in the $BaAl_2O_4$:Mn phosphor was also confirmed by EDS measurement.

PL measurements confirmed that the undoped phosphors possess room temperature phosphorescence properties with a 2:1 Sr/Si molar ratio sample prepared by co-precipitation method showing excellent white phosphorensce. A combination of two emission bands (495 and 687 nm) make up a white phosphorescence that cover a wide range of the spectrum, making this phosphor a potential candidate in solid state lighting applications. These emission bands were attributed to the intrinsic defects in the prepared $SrSiO_3/SiO_2$ phosphors. PL measurements also confirmed green room temperature phosphorescence from the $BaAl_2O_4$:Mn phosphor.

Thermoluminescence studies showed more than one overlaping peaks in all samples except for the 2:1 Sr/Si molar ratio sample which showed only one peak at 100 ^oC. For this reason, further thermoluminescence studies on this phosphor were carried out to assess prospects of applications in dosimetry. In addition to the observation of a single peak in this phosphor, linearity in a wide range of dose in it also proved that this has a potential for application in dosimetry. Also, the

emission band of this phosphor at 495 nm falls within the dosimetric requirement of emission range of 400 – 500 nm. Both the methods used to calculate the activation energy, the initial rise and variable heating rate yielded comparable results.

Contents

DECLARATION ii

ACKNOWLEDGEMENTS iii

ABSTRACT iv

CHAPTER 1 1

BACKGROUND 1

1.1. Luminescence 1

1.1.1. Chemoluminescence 1

1.1.2. Electroluminescence 1

1.1.3. Triboluminescence 1

1.1.4. Cathodoluminescence 1

1.1.5. Bioluminescence 1

1.1.6. Radioluminescence 1

1.1.7. Sonoluminescence 2

1.1.8. Photoluminescence 2

1.2. Radiative and non-radiative transitions 9

1.3. The Frank-Condon principle 10

1.4. Luminescence lifetime 12

1.5. Energy transfer (radiative and non-radiative) 16

1.5.1. Radiative mechanism 17

1.5.2. Non-radiative mechanism 17

1.6. The luminescence quantum yield (ϕ_l) 18

1.7. The Bandgap of a material 19

1.8. Defects in semiconductors 20

1.8.1. Zero-dimensional (Point) Defects 20

1.8.2. One-dimensional defects (Dislocations) 22

1.8.3. Two-dimensional defects 23

1.8.4. Three-dimensional (volume) defects 24

1.9. Electronic Transitions of Mn^{2+} Ion 24

REFERENCES 26

CHAPTER 2 31

Experimental Techniques 31

2.1. Introduction 31

2.1.1. Nucleation theory 31
2.1.1. Heterogeneous nucleation 34
2.1.2. Homogeneous nucleation 34
2.1.2.1. Homogeneous nucleation rate 37
2.2. Synthesis methods. 43
2.2.1. Precipitation Method 43
2.2.2. Combustion synthesis method 44
2.2.3. Hydrothermal Synthesis Method 46
2.3. Characterization techniques 48
2.3.1. Scanning Electron Microscope 48
2.3.2. X- Ray Diffraction 51
2.3.5. Photoluminescence Spectroscopy 56
2.3.5.1. Excitation and emission spectra 58
2.3.5.2. Lifetime measurements 59
2.3.5.2.1. TCSPC mode 59
2.3.5.2.2. *Phos-mode* 59
2.3.5.2.3. Kinetic mode 60
2.3.6. Quantum yield measurements 60
2.3.7. Thermoluminescence spectrometer 63
REFERENCES 65
CHAPTER 3 71
Structure, Morphology, and defects of $SrSiO_3/SiO_2$ phosphor 71
3.1. INTRODUCTION 71
3.2. EXPERIMENTAL 72
3.2.1. Sample preparation using co-precipitation method 72
3.2.2. Sample preparation using hydrothermal method 72
3.3. RESULTS AND DISCUSSION 73
3.3.1. Sample structure 73
3.3.2. Fourier transform infrared spectroscopy 75
3.3.3. Sample morphology 81
3.3.3.1. Scanning electron microscope 81
3.3.3.2. Energy-dispersive X-ray spectroscopy 83
3.4. CONCLUSION 84
REFERENCES 86
CHAPTER 4 90

Effect of non-stoichiometry on white phosphorescence and Thermoluminescence properties of $SrSiO_3/SiO_2$ phosphor 90

4.1. INTRODUCTION 90

4.2. EXPERIMENTAL 91

4.2.1. Sample preparation with co-precipitation 91

4.2.2. Characterization 91

4.3. RESULTS AND DISCUSSION 92

4.3.1. Sample structure 92

4.3.2. Fourier transform infrared spectroscopy (FTIR) 93

4.3.3. Photoluminescence properties of the SrSiO3/SiO2 phosphor material 93

4.3.4. Decay curves of the $SrSiO_3/SiO_2$ phosphor material 98

4.3.5. Thermoluminescence properties of the $SrSiO_3/SiO_2$ phosphor material 100

4.3.5.1. *General properties of a glow curve* 100

4.3.5.2. *Dose response.* 102

4.3.5.3. *Heating rate response from the $SrSiO_3/SiO_2$ phosphors* 107

4.4. Conclusion 114

REFERENCES 116

CHAPTER 5 121

Thermoluminescence investigation of the $SrSiO_3/SiO_2$ phosphor with 2:1 Sr/Si molar ratio for dosimetry applications 121

5.1. Introduction 121

5.2. Experimental 122

5.2.1. Sample preparation 122

***5.2.2.1. Sample structure.* 123**

***5.2.2.2. Fourier transform infrared spectroscopy (FTIR).* 123**

5.3. Results and discussion 123

***5.3.1. General properties of a glow curve* 123**

***5.3.2. Dose response* 124**

***5.3.3. Heating rate response* 126**

5.3.4. Kinetic analysis on a glow curve 127

***5.3.4.1 . The Initial Rise Method* 127**

***5.3.4.2. Chen's Peak Shape Method.* 129**

***5.3.4.3. The Variable heating rate method.* 130**

***5.3.4.4. The Hoogenstraaten's Method* 132**

5.4. Conclusions 133

REFERENCES **135**

CHAPTER 6 ..... **138**

Photoluminescence and thermoluminescence properties of Manganese doped $BaAl_2O_4$ phosphor **138**

6.1. Introduction **138**

6.2. Experimental **140**

6.2.1. Sample preparation **140**

6.2.2. Characterization **141**

6.3. Results and discussion **142**

6.3.1. X-ray diffraction studies **142**

6.3.2. Scanning electron microscopy and EDX studies **143**

6.3.3. X-ray photoelectron spectroscopy studies **144**

6.3.4. Steady state photoluminescence and Phosphorescence decay curves **146**

6.3.5. Thermoluminescence Studies **149**

6.3.5.1. *General properties of a glow curve of $BaAl_2O_4$: 2%Mn spinel phosphor* **149**

6.3.5.2. *Kinetic analysis of a TL glow curve of $BaAl_2O_4$: 2%Mn spinel phosphor* **155**

6.4. Conclusions **157**

REFERENCES **159**

CHAPTER 7 ..... **161**

Summary and Conclusion **161**

Key Terms: **162**

Future Prospects **163**

Acronyms **164**

PUBLICATIONS **165**

LIST OF FIGURES

Figure 1.2: The OTOR model illustrating thermoluminescence [9] **5**

Figure 1.3: A change in position of temperature at maximum intensity T_m as a function of heating rate β. **6**

Figure 1.8: A schematic of the difference between a direct gap and an indirect gap **20**

Figure 2.1: The Gibbs free-energy curves for solidification during synthesis process- When a liquid is cooled below the melting temperature, there is a driving force for solidification [5] **32**

Figure 2.2: Nucleation and grain growth processes during synthesis process [7]. **33**

Figure 2.3: A schematic showing free energy as a function of nucleus size during homogeneous nucleation [10]. 35
Figure 2.4: Schematic representation of the LaMer model of nucleation and growth [9]. . 39
Figure 2.5: Schematic illustration of co-precipitation method procedure of synthesizing nanomaterials. 44
Figure 2.6: A typical combustion synthesis process of ceramic oxide powders [30]. 45
Figure 2.7: A Schematic representation of a typical Teflon-lined stainless steel autoclave used for hydrothermal synthesis in the lab [35]. 47
Figure 2.8: A schematic diagram of Scanning Electron Microscope illustrating the electron beam path starting from the electron gun to the specimen and all the basic components [39]. 49
Figure 2.9: A schematic illustration of the interaction between the surface and the sample to produce different signals for surface analysis [40]. 50
Figure 2.10: A schematic illustration of a typical X-ray diffractometer [47]. 52
Figure 2.11: A schematic illustration of X-ray photoelectron spectroscopy [51]. 53
Figure 2.12: A schematic Diagram of an FTIR spectrometer with the IR source, interferometer, and the detector [57] 55
Figure 2.13: A schematic Diagram of a Fluorolog®-3 spectrometer, showing the path of a photon beam from the photon source (xenon lamb) until to the PMT detector [62]. 57
Figure 2.14: The Quanta-φ integrating sphere used for the quantum yield measurements [70]. 61
Figure 2.15: A schematic representation of TL reader sowing basic components [72]..... 64
Figure 3.1: XRD standard files of SiO_2 (a) and $SrSiO_3$ (b), together with XRD parttens of $SrSiO_3$/ SiO_2 phosphors prepared by co-precipitation method at Sr/Si molar ratio of 2:1 (c), 1:2 (d), 1:1 (e), 2.5:1 (f), and 3.5: 1 (g). (h) represents an XRD partten of $SrSiO_3$/ SiO_2 phosphors prepared by hydrothermal method at 2:1 molar ratio. 75
Figure 3.2: FTIR Spectra of phosphors prepared at 1:2 (a) and 1:1 (b) Sr/Si molar ratio by co-precipitation. The inserts in both (a) and (b) are plots to show peaks in the regions where weaker peaks were suppressed by the intense one at 1074 cm^{-1}. 77
Figure 3.3: FTIR Spectra of phosphor prepared at 2:1 Sr/Si molar ratio by co-precipitation (a) and hydrothermal method(b). The inserts in both (a) and (b) are plots to show peaks in the regions where weaker peaks were suppressed by the intense on. 79
Figure 3.4: Plot of FTIR Spectra in the range 500 – 2000 cm^{-1} of phosphors prepared by co-precipitation method at 2:1 and 2.5:1 Sr/Si molar ratio and phosphor prepared at 2:1 molar ratio by hydrothermal method (a). (b) is a plot of FTIR Spectra of all samples in the range 500 – 2000 cm^{-1}. The two plots are solely to make explicit the absense of the 705 cm^{-1} peak in the hydrothermal sample. 80
Figure 3.5: FTIR Spectra of phosphors prepared at 2.5:1 (a) and 3.5:1 (b) Sr/Si molar ratio by co-precipitation method. The inserts in both (a) and (b) are plots to show peaks in the regions where weaker peaks were suppressed by the intense one at 1074 cm^{-1}. 81
Figure 3.6: SEM low magnification (X 80) images of the $SrSiO_3$/ SiO_2 phosphors prepared by co-precipitation method at Sr/Si molar ratio of 2:1 (a), 1:2 (b), 1:1 (c) 2.5:1 (d) 3.5:1 (e) and hydrothermal method at 2:1 molar ratio (f). 82
Figure 3.7: SEM high magnification (X 5000) images of the $SrSiO_3$/SiO_2 phosphors prepared by co-precipitation method at Sr/Si molar ratio of 2:1 (a), 1:2 (b), 1:1 (c) 2.5:1 (d) 3.5:1 (e) and by hydrothermal method 2:1 (f) 83

Figure 3.8: EDS spectrum of the $SrSiO_3/SiO_2$ phosphors (a), elemental distribution frames of strontium (b), silicon(c), and oxygen (d)..... 84
Figure 4.1: Phosphorescence spectra of the $SrSiO_3/SiO_2$ phosphors prepared by co-precipitation method at Sr/Si molar ratio of 2:1 (a), 1:2 (b), 1:1 (c) 2.5:1 (d) 3.5:1 (e) and hydrothermal method at 2:1 (f). 96
Figure 4.2: Plots of phosphorescence spectra of the $SrSiO_3/SiO_2$ phosphors demonstrating strontiium concentration quenching. (a) is a demostration of concentration quenching using only plots of samples where Sr content was increased, while (b) represents PL plots of all samples ploted on the same set of axis. 97
Figure 4.3: CIE 1931 chromaticity coordinates of the $SrSiO_3/SiO_2$ phosphors prepared by co-precipitation method at Sr/Si molar ratio of 1:1 (a), 2:1 (b), 2.5:1 (c), 3.5:1 (d), 1:2 (f) and hydrothermal method at a ratio of 2:1 (e). The white circle inside the red plot triangle represents white light. CIE coordinates were calculated using the software GoCIE obtained from http://www.geocities.com/krjustin/gocie.html. 98
Figure 4.4: Phosphorescence decay curves of the $SrSiO_3/SiO_2$ phosphors prepared by co-precipitation method at Sr/Si molar ratio of 2.5:1 (a), 1:1 (b), 1:2 (c) 2:1 (d), 3.5:1 (e) and hydrothermal method at 2:1 (f). The solid black dots represent the experimental data, and the solid orange line is the fit of the data by third exponential model..... 100
Figure 4.5: Thermoluminescence spectra of the $SrSiO_3/SiO_2$ phosphors prepared by co-precipitation method at Sr/Si molar ratio of 2:1 (a), 1:2 (b), 1:1 (c) 2.5:1 (d) 3.5:1 (e) and hydrothermal method at a ratio of 2:1 (f). 102
Figure 4.6: Dose response curves of the $SrSiO_3/SiO_2$ phosphors prepared at Sr/Si molar ratio of 2:1 by co-precipitation method (a). (b) is a plot showing changes in both maximum intensity I_m and temperature at maximum intensity T_m with irradiation dose. 103
Figure 4.7: Dose response curves of the $SrSiO_3/SiO_2$ phosphors prepared at Sr/Si molar ratio of 1:2 by co-precipitation method (a). (b) is a plot showing changes in both maximum intensity I_m and T_m with irradiation dose. (c) is a plot of TL response to dose illustating a dose range beyond wich a high TL output from this phosphor saturates a detector..... 104
Figure 4.8: Dose response curves of the $SrSiO_3/SiO_2$ phosphors prepared at Sr/Si molar ratio of 1:1 by co-precipitation method (a). (b) is a plot showing changes in both maximum intensity I_m and temperature at maximum intensity T_m with irradiation dose. 105
Figure 4.9: Dose response curves of the $SrSiO_3/SiO_2$ phosphors prepared at Sr/Si molar ratio of 2.5:1 by co-precipitation method (a). (b) is a plot showing changes in both maximum intensity I_m and temperature at maximum intensity T_m with irradiation dose. 106
Figure 4.10: Dose response curves of the $SrSiO_3/SiO_2$ phosphors prepared at Sr/Si molar ratio of 3.5:1 by co-precipitation method (a). (b) is a plot showing changes in both maximum intensity I_m and temperature at maximum intensity T_m with irradiation dose. 107
Figure 4.11: Heating rate response curves from raw data of the $SrSiO_3/SiO_2$ phosphors prepared at Sr/Si molar ratio of 2:1 by co-precipitation method (a). (b) is plot of the data used in (a) but normalized with respect to heating rate β. (c) is a plot of temperature at maximum T_m against heating rate, whereas (d) is a plot showing the behaviours of both maximum intensity I_m and peak area as heating rate is increased. 109

Figure 4.12: Heating rate response curves of the $SrSiO_3/SiO_2$ phosphors prepared at Sr/Si molar ratio of 1:2 by co-precipitation method (a). (b) is plot of the data used in (a) but normalized with respect to heating rate β. (c) is a plot of temperature at maximum T_m against heating rate, whereas (d) is a plot showing the behaviours of both maximum intensity I_m and peak area as heating rate is increased..... 110
Figure 4.13:: Heating rate response curves of the $SrSiO_3/SiO_2$ phosphors prepared at Sr/Si molar ratio of 1:1 by co-precipitation method (a). (b) is plot of the data used in (a) but normalized with respect to heating rate β. (c) is a plot of temperature at maximum T_m versus heating rate, whereas (d) is a plot showing the behaviours of both maximum intensity I_m and peak area as heating rate is increased..... 111
Figure 4.14: Heating rate response curves of the $SrSiO_3/SiO_2$ phosphors prepared at Sr/Si molar ratio of 2.5:1 by co-precipitation method (a). (b) is plot of the data used in (a) but normalized with respect to heating rate β. (c) is a plot of temperature at maximum T_m versus heating rate, whereas (d) is a plot showing the behaviours of both maximum intensity I_m and peak area as heating rate is increased..... 112
Figure 4.15: Heating rate response curves from raw data and normalized data (a) and (b) respectively, of the $SrSiO_3/SiO_2$ phosphors prepared at Sr/Si molar ratio of 3.5:1 by co-precipitation method. (c) is a plot of temeprature at maximum intensity T_m as a function of heating rate, wheas (d) is a plot showing the behaviours of both maximum intensity I_m and peak area..... 114
Figure 5.1: Thermoluminescence spectrum of the $SrSiO_3/SiO_2$ phosphors synthesized by hydrothermal method at 2:1 Sr/Si molar ratio. The insert is a PL spectrum of the same phosphor showing emission peak at 495 nm..... 124
Figure 5.2: Dose response curves of the $SrSiO_3/SiO_2$ phosphors prepared at Sr/Si molar ratio of 2:1 by hydrothermal method (a). (b) and (c) are the plots of maximum intensity I_m and temperature at maximum intensity T_m both as functions of irradiation dose..... 125
Figure 5.3: Heating rate response curves from raw and normalized data (a) and (b) respectively of the $SrSiO_3/SiO_2$ phosphors prepared at Sr/Si molar ratio of 2:1 by hydrothermal method. (c) is a plot of temperature at maximum intensity T_m as a function of heating rate. (d) is a plot of both maximum intensity I_m and Peak area as functions of heating rate..... 127
Figure 5.4: glow curve of a 2:1 Sr/Si molar ratio $SrSiO_3/SiO_2$ phosphor prepared by hydrothermal method plotted as ln(I) vs. 1/T for calculation of the activation energy by the initial rise method. (a) is a recorded 100 °C TL glow peak, (b) is a plot of the whole data plotted as ln(I) vs. 1/T, (c) and (d) are plots of 10 % of maximum TL intensity, and (e) and (f) are plots of 15 % of the maximum TL intensity. 129
Figure 5.5: A Schematic representation of the peak shape method used for evaluation of the kinetic order..... 130
Figure 5.6: The plot of change in both the temperature at maximum intensity T_m and maximum intensity I_m with the heating rate..... 131
Figure 5.7: *The Hoogenstraaten's Method plotted for calculation of activation energy E.* . 133
Figure 6.1: Powder X-ray diffraction patterns of the as-prepared undoped $BaAl_2O_4$ (a), and $BaAl_2O_4$: 2%Mn spinel phosphors (b), along with $BaAl_2O_4$ standard file at the bottom..... 142
Figure 6.2: Field Emission Scanning Electron Microscope (FE-SEM) images of $BaAl_2O_4$: 2%Mn Phosphor acquired at different magnifications (a) X 9 500 and (b) X 22 000. 143

Figure 6.3: EDS spectrum from Ba-rich sites, together with its FE-SEM electron image and table1 showing quantitative results of each element in $BaAl_2O_4$: 2%Mn Phosphor (a). EDS spectrum from Ba-deficient sites, together with its FE-SEM electron image and table 2 showing quantitative results of each element in $BaAl_2O_4$: 2%Mn Phosphor (b). 144
Figure 6.4: XPS survey spectrum of $BaAl_2O_4$: 2%Mn spinel Phosphor (a), along with deconvoluted high-resolution XPS spectra of Ba 3d (b), Al 2p (c), O 1s (d), and Mn 2p (e). 146
Figure 6.5: Phosphorescence excitation spectrum (left), and emission spectrum (right) of Manganese ions in the $BaAl_2O_4$: 2%Mn spinel phosphor acquired at room temperature, both plotted on a linear scale. (b) the excitation spectrum associated with the 685 nm emission of Mn^{4+} ions. (c) is a magnification of the 685 nm of Mn^{4+} emission observed in (a), also plotted on a linear scale. (d) is a decay curve associated with the 512 nm emission of $BaAl_2O_4$: 2%Mn phosphor acquired at room temperature, plotted on a logarithmic scale. 148
Figure 6.6: The CIE 1931 chromaticity coordinates of $BaAl_2O_4$:2%Mn phosphor prepared by combustion method. The white circle inside the red plot triangle represents white light. CIE coordinates presented here were calculated using the software GoCIE obtained from http://www.geocities.com/krjustin/gocie.html. 149
Figure 6.7:A glow curve of $BaAl_2O_4$: 2%Mn spinel phosphor acquired at a constant heating rate of 2.5 $^oC/s$ after a beta irradiation of 180 Gy (a), before thermal cleaning with all three peaks (I, II, and III) present. The insert (I) shows two remaining peaks (II and III) after removal of peak (I) by thermal cleaning. Insert (II) represent the last peak (III) after the removal of the two peaks (I and II) by thermal cleaning. A glow curve showing an isolated peak (b). 151
Figure 6.8: The dependence of TL Intensity I_m (a) and (b), and temperature at maximum intensity T_m (c) of $BaAl_2O_4$: 2%Mn spinel phosphor on irradiation dose at a constant heating rate of 2.5 $^oC/s$. 152
Figure 6.9: The effect of heating rate on TL glow curves for $BaAl_2O_4$: 2%Mn spinel phosphor exposed to a 180 Gy beta dose. (a) is the obtained raw experimental data, while (b) is the normalized TL data. (c) and (d) are the temperature at maximum (T_m) and TL intensity at maximum (I_m) respectively as functions of heating rate. (e) shows the peak are as a function of heating rate. 155
Figure 6.10: TL glow curves of $BaAl_2O_4$: 2%Mn spinel phosphor plotted for activation energy calculations using (a), the peak shape method, and (b), and (c), the initial rise method. 157

LIST OF TABLES

Table 3. 1: ***The average crystallite sizes of the prepared phosphors.*** 70
Table 5. 1: ***Calculated activation energies for a single peak in the 2:1 Sr/Si molar ratio $SrSiO_3/SiO_2$ phosphor prepared by hydrothermal method.*** 129
Table 6. 1: ***Calculated Activation energies (E in eV) of the prominent peak using Chen's and the initial rise method.*** 153

CHAPTER 1

BACKGROUND

1.1. Luminescence

A phosphor is any material from which energy in the form of light is emitted following the stoppage of excitation [1]. This emission of light is a phenomenon referred to as luminescence. It is manifested when electrons from higher energy states recombine with holes in lower energy states in a phosphor material, following excitation of such material [2]. The energy of the emitted luminescence is according to Stoke's law lower than the excitation wavelength [1]. Among different types of luminescence phenomena which are classified in accordance with the methods of excitation listed below, only Photoluminescence and Thermoluminescence fall within the domain of this work and will be discussed in depth.

1.1.1. **Chemoluminescence** — Chemical energy is used to trigger this type of luminescence.

1.1.2. **Electroluminescence** — This type of luminescence involves excitation by electric field.

1.1.3. **Triboluminescence** — Mechanical energy is used in this case for excitation.

1.1.4. **Cathodoluminescence** — This involves excitation by a beam of electrons.

1.1.5. **Bioluminescence** — Biochemical Energy is used in this case for excitation.

1.1.6. **Radioluminescence** — This involves excitation by nuclear radiation such as X-rays, β-particles, γ-rays etc.

1.1.7. **Sonoluminescence —** Sound waves are used as a means of excitation in this type of luminescence.

1.1.8. **Photoluminescence** — A material exhibits this type of luminescence after being excited with photons of light. It is also divided into two subgroups namely:

1.1.8.1. ***Fluorescence***, a phenomenon which involves an allowed transition between an excited singlet and a ground singlet state and it lasts for a relatively shorter time, less than $1x10^{-8}$ s. Essentially, a material gets excited by absorbing photons. This absorption promotes electrons to the highest vibrational levels of the excited singlet state as shown in **figure 1.1**. The electrons then relax back to the lowest vibrational level of this state. Subsequent relaxations to the highest vibrational levels of the ground state results in the emission of photons with longer wavelengths than those of the absorbed photons as fluorescence [3,4].

1.1.8.2. ***Phosphorescence***, a phenomenon which involves a forbidden transition between an excited singlet state and a triplet state, and it has a lifetime of more than $1x10^{-8}$ s. This is a delayed emission of light by a phosphor material, which results from the electrons transitioning from the lowest triplet state of the phosphor material to the ground state. A phosphor absorbs photons, and its electrons get promoted to the highest vibrational levels of the excited singlet state as shown in **figure 1.1**.

The relaxation of these electrons to the lowest vibrational levels of the excited singlet state is followed by intersystem crossing to the triplet state as shown in **figure 1.1**. Subsequent relaxations of these electrons from the lowest vibrational level of the lowest triplet state to the highest vibrational level of the ground state results in the emission of photons with longer wavelengths than the absorbed ones known as phosphorescence [3,4].

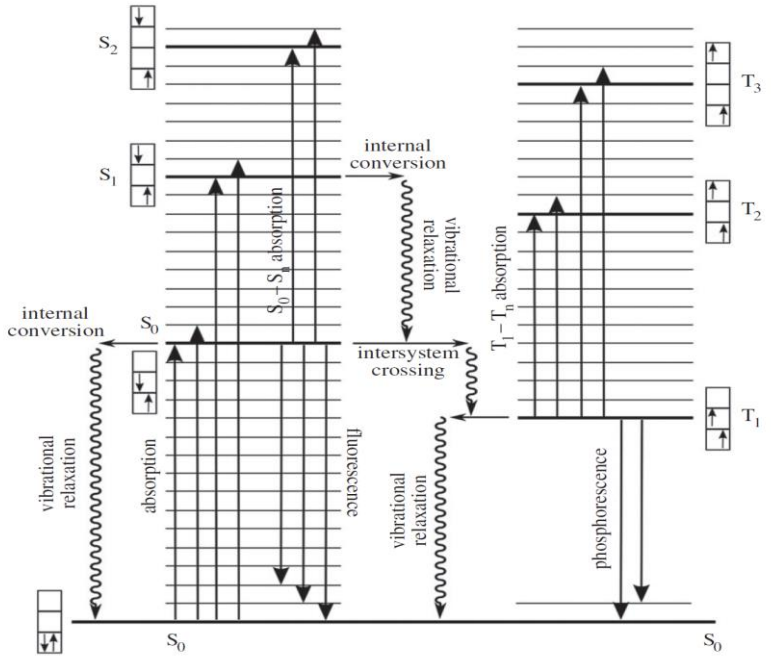

Figure 1.1: Jablonski representation of the fates of excited states of polyatomic molecules. S denotes singlet (spin paired) states, T denotes triplet states with unpaired spins, thus paramagnetic states. Solid lines represent radiative processes, wavy lines non-radiative. The occupancy of molecular orbitals and spin of electrons is indicated in the boxes [5].

1.1.9. ***Themoluminescence*** — This phenomenon involves excitation with photons and a subsequent thermal stimulation of relaxations.

1.1.9.1. *Definition*

This phenomenon essentially manifests when either an insulating or semiconducting material that was pre-exposed to some form of ionizing radiation is heated. The primary ionizing radiations are X-rays and radioactive elements. The intensity of emitted light is directly proportional to the ionizing radiation dose received by the sample during exposure. One interesting feature of this phenomenon is that, once heated to emit light, the material cannot be made to exhibit thermoluminescence again by simply cooling the sample and reheating it. It must be re-bombarded with some form of ionizing energy [6]. Exposure to radiation is a means to fill traps within the bandgap of the material with electrons,

while heating is for triggering the relaxation of these electrons to give out emission of light as thermoluminescence [6]. The light intensity of the TL emission is then measured and recorded by a device such as photomultiplier tube against temperature to produce what is known as a glow curve. The flashes on the glow curve represent glow peaks [7].

1.1.9.2. *Early discovery*

The discovery of thermoluminescence phenomenon dates back to the 1663 period when Sir Robert Boyle first observed this phenomenon from a diamond which he had held for some time upon his warm part of his body. A glimmering light from the diamond was also observed when Sir Robert Boyle developed some curiosity to test this phenomenon with various other sources such as candle, a heated metal, and friction [8]. However, the idea was not fully understood until du Fay interpreted this phenomenon as delayed phosphorescence. In the 19^{th} century, Henri Becquerel further observed this phenomenon in phosphorescent samples. Wiedemann and Schmidt also explored this phenomenon on the detection of cathode rays and UV light. They observed an intense emission with long storage life in Manganese-doped CaF_2 and in mineral fluorite after irradiating them with cathode rays [8].

1.1.9.3. *Thermoluminescence model*

To get a clear understanding of the process by which TL phenomenon take place in a thermoluminescent material, a simple model comprising of two localized levels, and isolated electron trap T and a recombination center RC can be adopted. This model shown in **figure 1.2** is widely known as one-trap-one-recombination center model or the OTOR model [9].

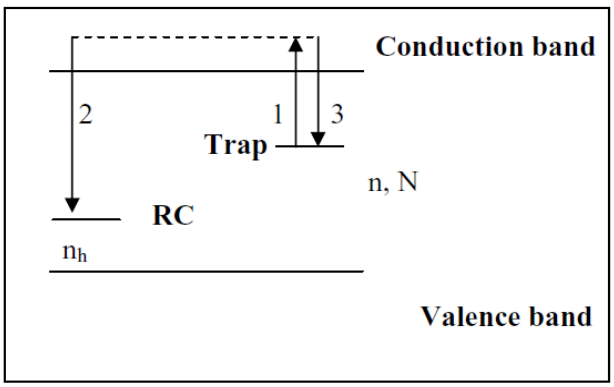

Figure 1.2: The OTOR model illustrating thermoluminescence [9]

N denotes the total concentration of traps, n the concentration of filled traps, and n_h the concentration of trapped holes in the recombination centre (RC). During the TL experiments, a sample is usually exposed to some form of excitation energy. This promotes electrons into the conduction band of a thermoluminescent material. The promoted electrons later drop into localized metastable states called traps. Heating the material at a linear rate from room temperature to higher temperature, usually 500 ^{o}C, gives the electrons in traps thermal energy to transition into the conduction band as illustrated by transition 1 in **figure 1.2**. Once these electrons are in the conduction band, they have two fates namely: recombination with holes in the recombination centre (transition 2) and getting re-trapped into the electron trap (transition 3). The recombination of conduction band electrons and holes in the recombination centre emit light with the intensity according to equation 1.1 [9].

$$I(t) = -dn_h/dt \tag{1.1}$$

The intensity of this emitted light is plotted against the sample temperature during thermoluminescence experiments, and the resulting graph is known as thermoluminescence glow curve. The heating temperature needs to be lower than the one that can initiate visible incandescence [6]. Usually, during

thermoluminescence experiments, the sample is heated using a linear heating rate β according to equation 1.2.

$$\beta = \frac{dT}{dt} \tag{1.2}$$

Where T and t are temperature and time respectively. However, when heating a thermoluminescent material with this linear heating rate during experiment, there is usually a temperature lag between the heating element and the sample. In other words, the temperature recorded by TL reader, which is that of the heating element, is usually not the same as that of the sample, instead it is higher [10]. This tends to shift the temperature at maximum intensity T_m to higher temperatures as shown in **figure 1.3** below.

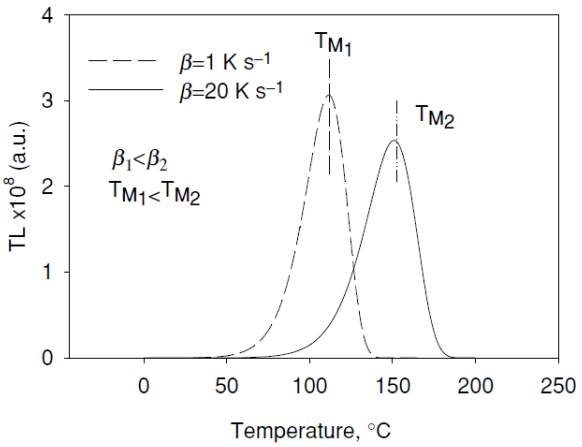

Figure 1.3: A change in position of temperature at maximum intensity T_m as a function of heating rate β.

Another interesting observable feature is the decline of thermoluminescence intensity at elevated heating rates. This is known to occur by virtue of a phenomenon referred to as thermal quenching [11]. This phenomenon is known to suppress TL efficiency η_{TL} according to equation 1.3.

$$\eta_{TL} = \frac{P_r}{P_r + P_{nr}} \tag{1.3}$$

Where P_r is the probability of luminescence transitions, which unlike the probability of non-radiative transitions P_{nr}, is temperature independent. Essentially, at higher temperatures, the competition between radiative and non-radiative transitions tend to favour the non-radiative transitions and this suppresses luminescence efficiency, hence a decrease in TL intensity [6].

TL experiments are usually carried out to measure and analyse the glow curves, with the main objective of extracting parameters which can be utilized for describing a thermoluminescence process in a phosphor material exhibiting a thermoluminescence phenomenon. These parameters are the activation energy *E* for the TL traps, which is also known as trap depth, the frequency factor s, the order of kinetics *b* of the TL process, the capture cross-section for the traps and recombination centers, and the concentrations of these traps and centers [12].

The order of kinetics which is followed by a thermoluminescence glow curve is of paramount importance in that once known, it is easy to know which exponential equation governs the TL process and therefore other parameters can then be evaluated from that basis [6]. One way of evaluating the order of kinetics is by observing the behaviour of T_m as the concentration of trapped electrons n_o change. If during thermoluminescence measurement the temperature T_m at maximum TL intensity is independent upon the initial concentration of trapped electrons as shown in **figure 1.4**, then that glow curve is known to follow a first order of kinetics [6].

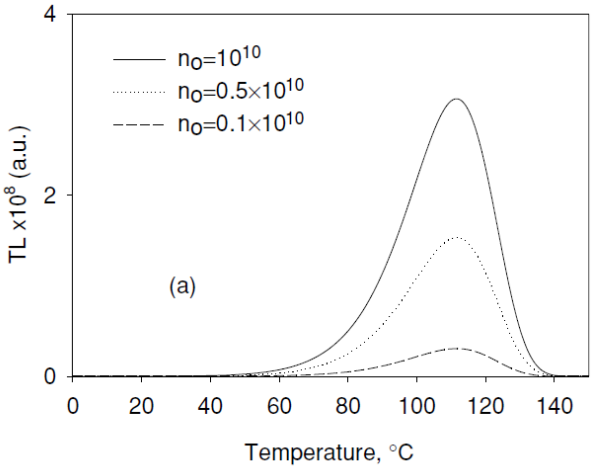

Figure 1.4: First order TL glow peaks with T_m independent of initial concentration of trapped electrons [9].

The TL processes of such glow curves are governed by a first order equation below.

$$I(t) = -\frac{dn}{dt} = nSe^{-E/KT} \tag{1.4}$$

On the other hand, a glow curve for which T_m is dependent upon the initial concentration, and shifts towards elevated temperatures with the drop in concentration of trapped electrons as depicted in **figure 1.5**, TL processes responsible for that glow curve are known to follow a second order kinetics [9].

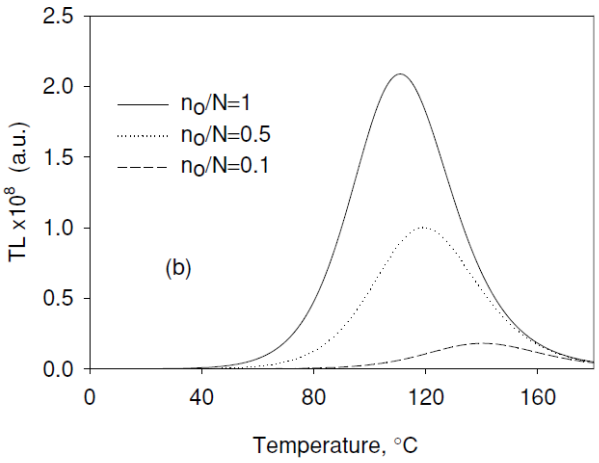

Figure 1.5: Second order TL peaks with temperature at maximum T_m depending on the initial concentration of trapped electrons [9].

The TL process of such curves is governed by second order kinetics in equation 1.5.

$$I(t) = -\frac{dn}{dt} = \frac{n^2}{N} Se^{-\frac{E}{KT}} \tag{1.5}$$

A second order kinetics is the result of the emission of photons in the form of light being delayed by the re-trapping of electrons in the traps and this is mostly noticeable on the descending part of the TL glow curve [9].

1.2. Radiative and non-radiative transitions

In a luminescent material, whether or not the luminescence process (fluorescence or phosphorescence) will take place following excitation, the process is dictated by the spin selection rule for electronic transitions i.e. absorption and emission. The rule requires that the spin multiplicity remain unchanged for the initial and final electronic states for transitions to be deemed "spin-allowed" [13]. This all depends on the likelihood for one transition to take

place. For instance, spin-allowed transitions like fluorescence are more probable to occur than spin-disallowed transition such as phosphorescence [13,14].

Following excitation, the stored energy is not only given off as photons (radiative) or luminescence. There are also non-radiative processes also known as vibrational relaxations which take place very rapidly ($\sim 10^{-14}$ to 10^{-12}) after excitation and before luminescence can take place. They essentially take place when an excited material relaxes rapidly from a higher vibrational level of excited state to the lowest vibrational level of that excited state.

Such processes are of two types, namely internal conversion, and intersystem crossing [13]. Internal conversion involves a rapid non-radiative relaxion from a higher-energy excited singlet state (S_2 in **figure 1.1**) to the lower-energy singlet excited state (S_1 in **figure 1.1**) [13,14]. Intersystem crossing on the other hand is a process that involves non-radiative transition from electronic states of unlike spin multiplicity such as S_1 and T_1 in **figure 1.1** [13]. Since the spin multiplicity is not conserved in this process, intersystem crossing is a less probable process compared to internal conversion, and it therefore takes place very slowly ($\sim 10^{-8}$ s) than internal conversion. This process becomes likely in the presence of heavy atoms such as transition metals, where the interaction between spin angular momentum and orbital angular momentum (spin-orbit coupling) becomes significant. Such an interaction usually results in a change in spin. In transition metal complexes, the probability of intersystem crossing increases as one proceeds from complexes of the 3d-block elements to those of 4d and 5d-blocks [13].

1.3. The Frank-Condon principle

This is a very useful principle that can be used as a complementary model to explain why the absorption transitions in the jablonski diagram (**figure 1.1**) are depicted from singlet ground to higher vibrational levels of singlet excited states ($S_o \rightarrow S_n$) than the lowest vibrational level (v=0). It also explains why there is no direct transition from a singlet ground state to any of the triplet states in **figure**

1.1. Essentially, the electronic absorption of light takes place within a very short period (~ 10^{-15} s).

Considering that this time is extremely short, the nuclei are presumed to be frozen (not have enough time to move) during this time of light absorption [13,15]. For this reason, the transitions between various electronic levels in **figure 1.1** are depicted as vertical transitions. These vertical transitions are assuming the Frank-Condon principle depicted in **figure 1.6**, which is an assumption that there is no (or negligible) nuclear displacement during electronic transitions. In other words, this principle requires that the nuclear geometries before and after light absorption be similar [13,15].

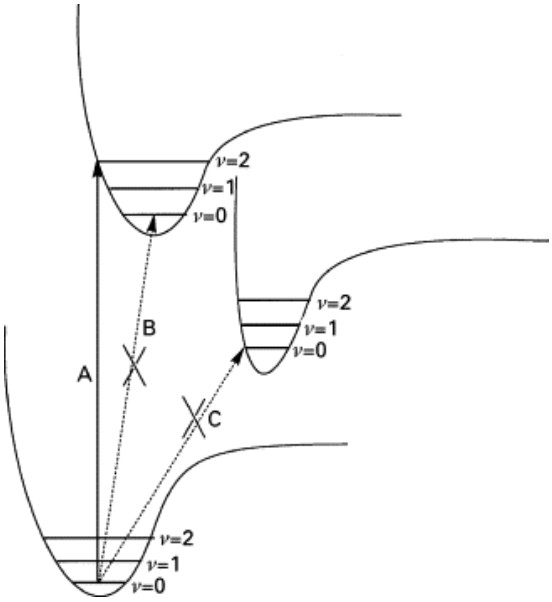

Figure 1.6: A schematic representation of the Frank-Condon principle illustrating allowed and disallowed transitions in a molecule [16].

Upon the absorption of photons by electrons, a redistribution of an electronic cloud within the molecular orbitals results, and this usually results in the differences between the electronic excited and ground states geometries [17, 18,19,20]. In other words, electronic excitation would be accompanied by a

change in nuclei positions when they take place if photon absorption was not very short. Now, since the Frank-Condon principle neglects this change of nuclei position, only transition A (vertical) in **figure 1.6** is allowed. Transition C is disallowed as it is to an excited state that is to a large extend displaced from the ground state. Transition B is also disallowed, due to its termination in the lowest vibrational level of the excited state [13].

1.4. Luminescence lifetime

It is a common knowledge that some luminescent phosphor materials do exhibit both fluorescence and phosphorescence during luminescence measurement. It is therefore necessary in this case when doing the analysis, to do spectral assignment after doing spectral acquisition, i.e. assign the luminescence bands either as fluorescence or phosphorescence. This is done by carrying out lifetime measurements, a measure of the average time a luminescent species spends in the relevant excited electronic state before it can relax to the ground state [13].

As a general guideline, phosphorescence lifetimes are usually longer (on the order of microsecond and longer), while fluorescence lifetimes are shorter, on the sub-microsecond level (nanosecond, picosecond etc) [21]. This simply means that when doing spectral assignment, a luminescence band (or peak) corresponding to a transition whose excited state lifetime is longer is typically assigned as phosphorescence and conversely, the band corresponding to a transition whose excited state lifetime is shorter is assigned to fluorescence [21,13].

Essentially, lifetime measurements are experimentally acquired using a pulsed laser source. Typically, if a molecule A is bombarded with this pulsed laser source, this leads to a population of the excited electronic state of A by electrons. Once the excited electronic state $^*A$ is populated with electrons, the electrons from this state can decay back to the ground state either radiatively (emitting energy in the form of photons) or non-radiatively (without photon emission) [13]. There are therefore different ways in which to model (do curve fitting) the lifetime data

following the lifetime measurements of **A* depending on the number of pathways through which the molecule **A* can decay [13,15].

For instance, when a molecule has only a single pathway of decay, i.e. **A* only decays by emitting photons (fluorescence or phosphorescence), it's decay can be characterized by a first order process in equation 1.6 below [13].

$$^*A \rightarrow A + h\upsilon \tag{1.6}$$

h and υ denote plank's constant and photons frequency respectively. The decay rate of **A* can therefore be expressed as:

$$\frac{-d[^*A]}{dt} = k_l[^*A] \tag{1.7}$$

where k_l denotes the rate constant of luminescence decay, the reciprocal ($1/k_l$) of which is the luminescence (fluorescence or phosphorescence) lifetime τ_l.

Equation 1.7 can be integrated to:

$$[^*A] = [^*A]_o \exp(-t/\tau_l) \tag{1.8}$$

Therefore, plotting In[**A*] as a function of time *t* should yield a straight line with a slope of $1/\tau_l$ from which the lifetime can be calculated [13].

The decay of **A* is however not always only through the emission of photons. Instead, it is sometimes accompanied by energy release through vibrations (non-radiative decay). In this case a molecule has two pathways of decay, and it can be described by equation 1.9 [13].

$$^*A \rightarrow A + vibrational\ energy \tag{1.9}$$

The rate of decay of *A in this case can be written as:

$$\frac{-d[^*A]}{dt} = k_l[^*A] + k_{nr}[^*A] = (k_l + k_{nr})[^*A] \tag{1.10}$$

Therefore the lifetime τ can be written as $\tau = \frac{1}{(k_l + k_{nr})}$, the reciprocal of the sum of k_l and non-radiative constant k_{nr}. It is worth noting at this stage that the non-radiative rate constant generally tends to decrease at lower temperature value. So, as the temperature (*T*) approaches absolute zero, the lifetime τ approaches $1/k_l$. This simply means that if $1/\tau_l$ is plotted as a function of *T*, then k_l can be determined as the value of the intercept through the extrapolation of the graph to *T*=0 *k*. From the value of k_l, the luminescence lifetime of a particular transition can be determined as $1/k_l$ [13]. The model explained above only hold in the case when a luminescence material only shows a single-exponential decay.

However, some luminescent materials such as biological tissues exhibit multicomponent decays. Such complex luminescence decays are commonly modelled using the multi-exponential decay functions such as $F_{m-\exp}(t,\lambda)$ in equation 1.11 [17,22].

$$F_{m-\exp}(t,\lambda) = I(\lambda)\sum a_i(\lambda)\exp(-t/\tau_i) \qquad (1.11)$$

Where a_i and τ_i are the fitting parameters, amplitudes of the exponential components at time zero, and decay times respectively. $I(\lambda)$ is the total amplitude, which is normalized, and because of this, luminescence lifetime analysis gives only amplitude fractions. There are however instances where a luminescent material has more than just one type of emitting species (or states) or one type of emitting species which is surrounded by different environments. Such materials often have more complex luminescence decay profiles, and therefore their decay processes cannot be described as simply as explained above. Instead, they are commonly described by average lifetime equations. The first of the most commonly used average lifetimes is the "*intensity average lifetime*" $\langle\tau\rangle_i$ below [22,23].

If the fractional contribution F_{int} of each decay to the total integrated intensity $\int I(t)dt$ can be written as:

$$F_{\text{int}} = \frac{a_i \tau_i}{\sum a_i \tau_i} \tag{1.12}$$

Then the intensity averaged lifetime can be calculated as:

$$\langle \tau \rangle_i = \sum F_{\text{int}} . \tau_i = \frac{\sum a_i . \tau_i^2}{\sum a_i . \tau_i} \tag{1.13}$$

F_{int} defines the percentage of photons which belong to one decay relative to the total number of emitted photons. Equation 1.13 is based on the observation that the luminescence intensity contribution of a component, *i*, is proportional to the product $a_i \tau_i$. t denotes time, and τ is the luminescence lifetime. This is the average lifetime of a collection of different excited states populations, where the lifetime of each population is weighted by the relative contribution of that population to the total luminescence (fluorescence or phosphorescence) [22,23].

The alternative type of average lifetime that is commonly used is the amplitude averaged lifetime. Like above, if the amplitude fractional contribution can be written as:

$$F_{amp} = \frac{a_i}{\sum a_i} \tag{1.14}$$

then the amplitude average lifetime $\langle \tau \rangle_{amp}$ can then be written as:

$$\langle \tau \rangle_{amp} = \sum F_{amp} . \tau_i = \frac{\sum a_i . \tau_i}{\sum a_i} \tag{1.15}$$

Here the meaning of F_{amp} is dependent upon the physical origin of different time decays τ_i. For instance, if the decay is from a mixture of emitting species in a luminescent material, each fraction F_{amp} is related to the relative concentration of the individual species. If on the contrary, the decay comes from the same emitting

species in different environments, F_{amp} represents the population of each conformer [22,23]. A more related luminescence property to the lifetime is the quantum yield, which is discussed later.

1.5. Energy transfer (radiative and non-radiative)

Upon exposure of an atom or a molecule to some form of excitation source, one of the process through which the atom can later relax back to its ground state is energy transfer, where the excited atom or molecule (donor) transfers part of its excitation energy during its lifetime to another atom that has a weak absorption band in that relevant pumping band (acceptor) as shown in **figure 1.7** [4,24].

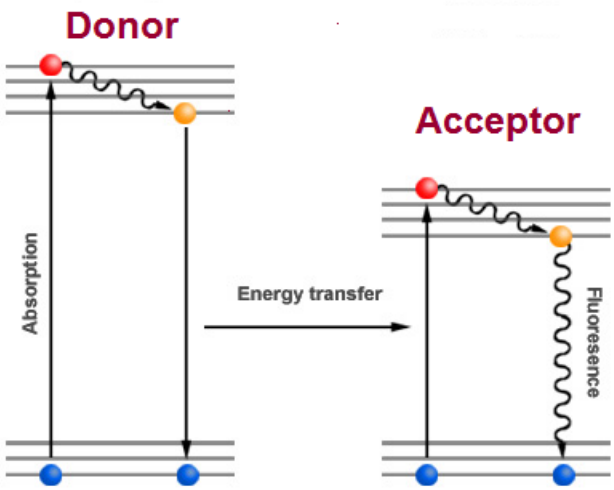

Figure 1.7: A schematic illustration of energy transfer taking place between a donor and an acceptor molecule [25].

During this process, the donor promotes the acceptor to its excited state by returning to the ground state. In the case where the acceptor is a luminescence species, it can emit photons following excitation by the donor (energy transfer) and this type of luminescence is referred to as sensitized luminescence. In this case, the donor is called the sensitizer species [4,24]. There are two ways in which energy transfer can take place in a material, namely radiative and non-radiative mechanisms.

1.5.1. Radiative mechanism

In this mechanism as shown from equation 1.16 to 1.18, a donor molecule (Don) at ground state typically absorbs energy (or light) and get promoted to its excited state (Don^*). It then emits at shorter wavelength that overlaps with the absorption spectrum of the acceptor molecule. These emitted photons are then re-absorbed by the acceptor at its ground state (Acc) and the acceptor ion gets promoted to its excited state (Acc^*) with a subsequent emission of photons that is enhanced [4,24,17].

$$Don + h\upsilon \rightarrow Don^* \tag{1.16}$$

$$Don^* \rightarrow Don + h\upsilon \tag{1.17}$$

$$Acc + h\upsilon \rightarrow Acc^* \tag{1.18}$$

The efficiency of radiative energy transfer is dependent upon the quantum yield of the donor luminescence and the absorbance of the acceptor molecule at the donor emission wavelength. In this mechanism, a donor molecule and the acceptor molecule do not need to significantly interact, therefore energy transfer taking place via this mechanism can do so over extremely large separations between donor and acceptor molecule [4,24,17].

1.5.2. Non-radiative mechanism

Contrary to the radiative mechanism, a non-radiative energy transfer involves an efficient absorption of excitation energy by the donor ion or molecule and subsequently transfers part of that energy to the neighbouring acceptor ion. The acceptor in this case has no or small absorption bands within the emission bands of the donor ion [4,24,17].

Energy transfer taking place through this mechanism can be described as shown in equation 1.19 below.

$$Don^* + Acc \rightarrow Don + Acc^* \tag{1.19}$$

No photons are emitted by the donor in this mechanism. Since this mechanism is a non-radiative energy transfer process, it is accompanied by a decrease in the lifetime of the excited state of the donor ion. There are two channels through which the non-radiative energy transfer takes place namely; the Förster resonance and the Dexter exchange mechanism. The Förster resonance mechanism requires an electrostatic interaction between the donor (Don) and the acceptor (Acc), which means that this mechanism does not necessarily require a very close contact between the donor and the acceptor. It is also described by classical theory as an interaction between two oscillating dipoles. Through this mechanism, energy transfer may take place over donor-acceptor distances as long as 50 to 100 Å [4,24,17].

The efficiency of the energy transfer which take place through this mechanism is very much dependent on the transition energies of the donor and that of the acceptor. That is to say, the transition energy from the excited state of the donor to the ground state of the donor ($Don^* \rightarrow Don$) must be almost identical to that of the acceptor from its ground to the excited state ($Acc \rightarrow Acc^*$), hence the name "*resonance mechanism*". If there exists a small difference between these transition energies, the presence of phonons may assist for energy transfer to take place, a process called "*phonon-assisted*" energy transfer. In this case the phonons energies are required to be high enough to overcome the difference between these transition energies [4,24,17].

The Dexter exchange mechanism on the other hand requires a direct contact between the donor and the acceptor ions or molecules. In other words, there has to be an overlap between orbitals of a donor molecule and those of an acceptor molecule [4,24,17].

1.6. The luminescence quantum yield (ϕ_l)

This is defined as the ratio of the number of emitted photons to the number of absorbed photons by a luminescent material as described in equation 1.16 [13,18].

$$\Phi_l = \frac{\sum K_{rad}}{\sum K_{rad} + \sum K_{n-rad}} \quad (1.16)$$

Where K_{rad} denotes the luminescence (fluorescence and phosphorescence) rate constant, and K_{n-rad} is the rate constants of all the non-radiative processes (vibrational relaxation, internal conversion, and intersystem crossing) as depicted in **figure 1.1**. The maximum value of luminescence quantum yield is by definition, equal to one. However, due to a considerable number of non-radiative processes which lead to a decline in the number of photons which are emitted, the practically measured quantum yield is less than one [13,18].

1.7. The Bandgap of a material

Firstly, and importantly, it is worth highlighting what qualifies a material to be a semiconductor, as opposed to other types of materials. In a solid material, there exist a lower band of states containing as many states as electrons (completely filled with electrons) referred to as the valence band, together with the upper one which contains no electrons, referred to as the conduction band [26]. Now the energy gap between these two bands and the relative availability of electrons in them are key in determining whether the material is a semiconductor, an insulator, or a metal. For instance, the energy gap (band gap) of a semiconductor is usually in the range of 0.5 to 5.0 eV, while in an insulator material it usually extends over 5 eV. For a metal it is 0 eV [27]. There are two types of band gaps in a semiconductor material categorized according to the position of the top of the valence band relative to the bottom of the conduction band in a momentum space (k-space). In an indirect band gap, the top of the valence band and the bottom of the conduction band of a semiconductor lie at different points in momentum space as shown schematically in the **figure 1.8** [27].

On the contrary, in the case of a direct band gap the top on the valence band and bottom of the conduction band lie at the same point in momentum space as shown schematically in the **figure 1.8**. Of interest among these two types of band gaps is a direct one, because materials with direct band gap have an important

consequence for optical applications of semiconductors, because of a higher probability of electronic transitions across the band gap in them as opposed to materials with indirect band gap [27].

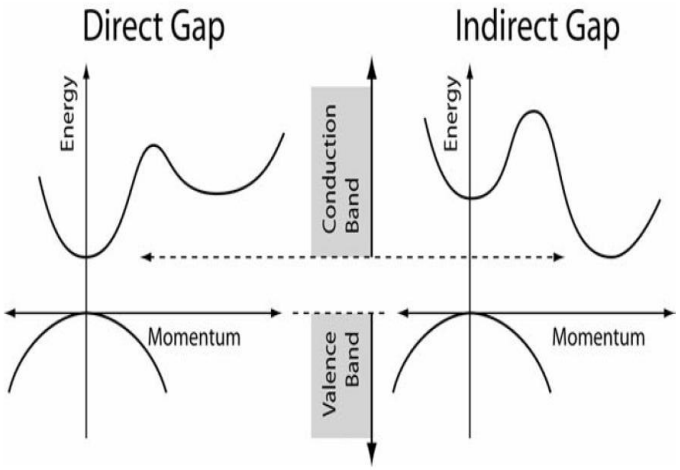

Figure 1.8: A schematic of the difference between a direct gap and an indirect gap Semiconductor [28].

1.8. Defects in semiconductors

Like any other semiconductor materials, defects in phosphors, particularly those introduced during the growth process play a pivotal role in determining their physical properties such as absorption and emission wavelengths, and mechanical properties [29]. Some native defects on the other hand are usually a setback on the performance of semiconductor devices. Various types of defects which are likely to form in silicate matrices and affect the performance of these phosphors are outlined according to their dimensions below.

1.8.1. Zero-dimensional (Point) Defects

In a crystalline material, point defects also known as zero-dimensional or atomic-size defects are defects that exist at, or around a single lattice point as shown in **figure 1.9** [30]. These are types of defects, the total concentration of which usually goes to the minimum level, but never reach zero [31]. This is attributed to the

increase of configurational entropy, which leads to a decrease in total Gibbs energy. In simple terms, point defects are inevitable during crystal growth [31]. When an atom in a crystal lattice is removed from its repetitive lattice site, the point defect is referred to as a vacancy as shown in **figure 1.9** (a). If on the other hand, an atom occupies a lattice site different from its repetitive site as shown in **figure 1.9** (b), the point defect is referred to as an interstitial defect, and there are two ways in which this can take place depending on atoms species.

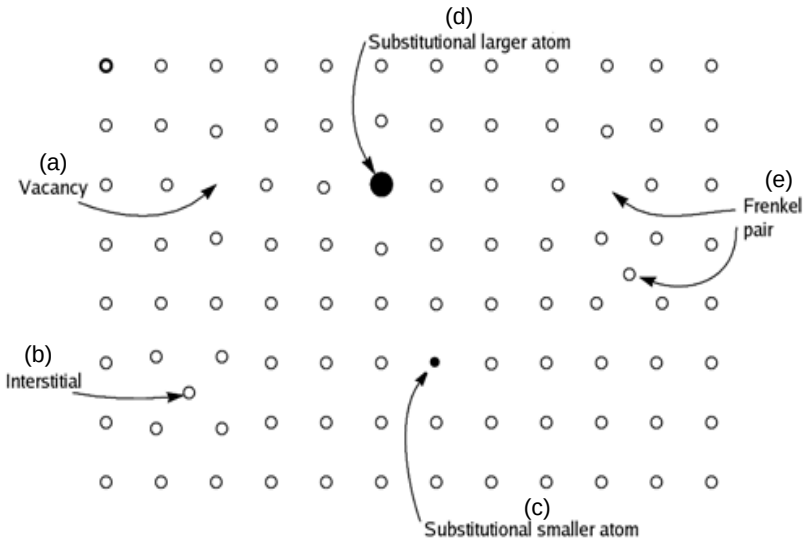

Figure 1.9: A Schematic illustration of point defects in a crystalline solid [32].

If an interstitial atom is of different species as the atoms in the lattice, it is called an extrinsic defect or simply an interstitial impurity. An intrinsic defect results when an interstitial atom is of the same species as those of the lattice. A point defect may also form when an impurity resides in a substitutional lattice site as shown in **figure 1.9** (c) and (d) [33,34].

Some types of point defects are commonly formed in ionic solids through the association of intrinsic, extrinsic, substitutional, or interstitial. For instance, a point defect such as a Frenkel pair may result if an atom is displaced from its regular site to an interstitial site leaving a vacancy behind. This atom in the

interstitial site together with the vacancy form a Frenkel pair as depicted in **figure 1.10** [35].

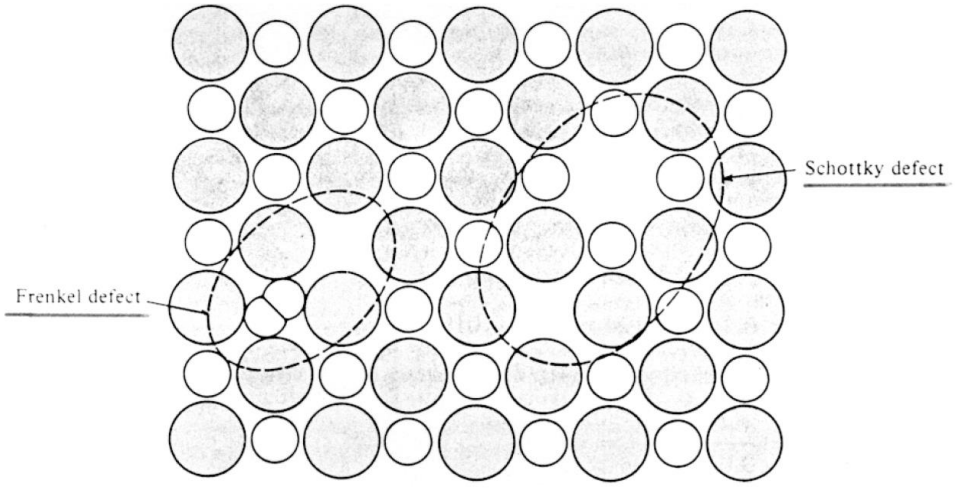

Figure 1.10: A Schematic interpretation of Schottky and Frenkel defects in a crystalline solid [36].

Alternatively, Schottky defects may be formed from balanced populations of cation and anion vacancies in a crystal [33,34]. A simple example is when a vacant cationic site in a crystal is balanced by a vacant anionic site as illustrated in **figure 1.10**, to retain electrical neutrality [37]. In such a crystal, one Schottky defect is formed by one cation vacancy plus one anion vacancy. Schottky defects are generally formed at the surface, block boundaries, and at dislocations followed by diffusion into the bulk [38].

1.8.2. One-dimensional defects (Dislocations)

One dimensional defects are line defects which form and extend along a line or a curve in a crystal lattice of a material [39]. These types of defects result when a plane of atoms is out of place from its original position. One simple way of understanding how they form is by imagining cutting a crystal along a plane and slipping one half across the other buy a lattice vector.

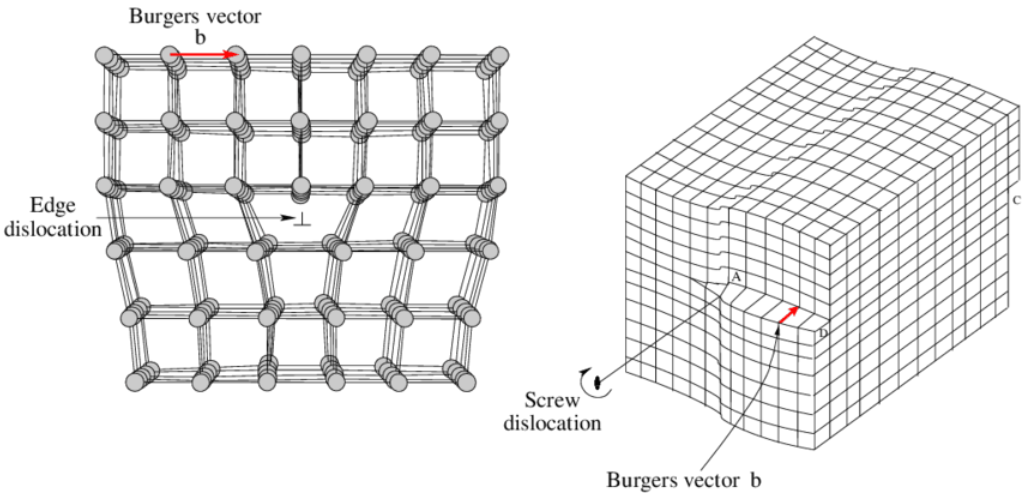

Figure 1.11: A illustration of screw and edge dislocations in a crystalline solid with burgers vector b [40].

If the two halves were to be fit back together, they will not leave a defect. On the contrary, a boundary of the cut will leave dislocation if the cut does not go fully through the crystal [41]. The boundary of the cut is then referred to as the dislocation line, and vector of the slip is the Burgers vector [41]. There are two types of dislocations, namely, screw and edge dislocations as shown in **figure 1.11**.

In the case where this vector is perpendicular to the dislocation line, the dislocation is referred to as the edge dislocation. Screw dislocation results when the burgers vector is parallel to the dislocation line [39].

1.8.3. Two-dimensional defects

These are planar defects or surface imperfections that expand indefinitely along two directions in a solid material. Although they are referred to as planar defect, their planes do not need to be flat [42]. There are a number of different types of planar defects. For instance, regions with the same composition and crystal structure but with different orientation can be separated by interfaces in a solid material, and these types of interfaces are one type of planar defect referred to as grain boundaries. Grain boundaries are often found in polycrystalline materials

[42,43]. Secondly, in a solid material, phase boundaries are essentially interfaces that isolate regions with distinct compositions and crystal structures. The crystals on both sides of the phase boundary may or may not be of the same orientation.

There is also a situation in a solid material in which a mistake in the perfect stacking order of a crystal happens, and that results in another type of planar defect called stacking fault. An antiphase boundary is also possible in a solid material where an interface isolating regions of a crystal with the same composition, crystal structure, and orientation, but with a mistake in the ordering pattern at the boundary. Lastly, magnetic and ferroelectric domain boundaries are one of the types of planar defects found in a solid material [42].

1.8.4. Three-dimensional (volume) defects

In a semiconductor, any volume that differs from the rest of the crystal in composition, structure, and/or orientation is referred to as a volume defect [44]. These are defects which form from clusters of vacancies that may grow and ultimately collapse to form dislocation loops. Situations such as precipitation of impurities into a separate phase, and impurity atoms, formation of large three-dimensional aggregates by vacancies are also possible in a semiconductor material.

Volume defects include second phase particles (precipitates), intrinsic vacancy conglomerates (microvoids), cracks and foreign particles (inclusions) [42,45]. It is worth emphasizing that, it is imperative in the application of semiconductors in various electronic devices to control the influence of surface, interface, and grain boundaries on properties of semiconductors and electronic devices, as they can sometimes have a detrimental effect.

1.9. Electronic Transitions of Mn^{2+} Ion

Mn^{2+} is well known by emissions which can be influenced by the crystal field ranging from green to orange-red regions of the visible spectrum due to the

$^4T_1(^4G) \rightarrow {}^6A_1(^6S)$ transition [46], which suggests that the emission color of the Mn^{2+} ion is influenced by the environment surrounding it. When Mn^{2+} is octahedrally coordinated, the crystal field effect is strong and the $^4T_1(^4G) \rightarrow {}^6A_1(^6S)$ transition tends to result in red or orange emissions. On the contrary, when Mn^{2+} is tetrahedrally coordinated, the $^4T_1(^4G) \rightarrow {}^6A_1(^6S)$ green emission may result [47]. This type of behaviour broadens the applications of Mn^{2+} doped phosphor materials in fluorescent lamps, cathode ray tubes, and white light emitting diodes [48]. **Figure 1.12** depicts a schematic diagram of Mn^{2+} energy levels and electronic transitions taking place in the d orbital of Mn^{2+} ion.

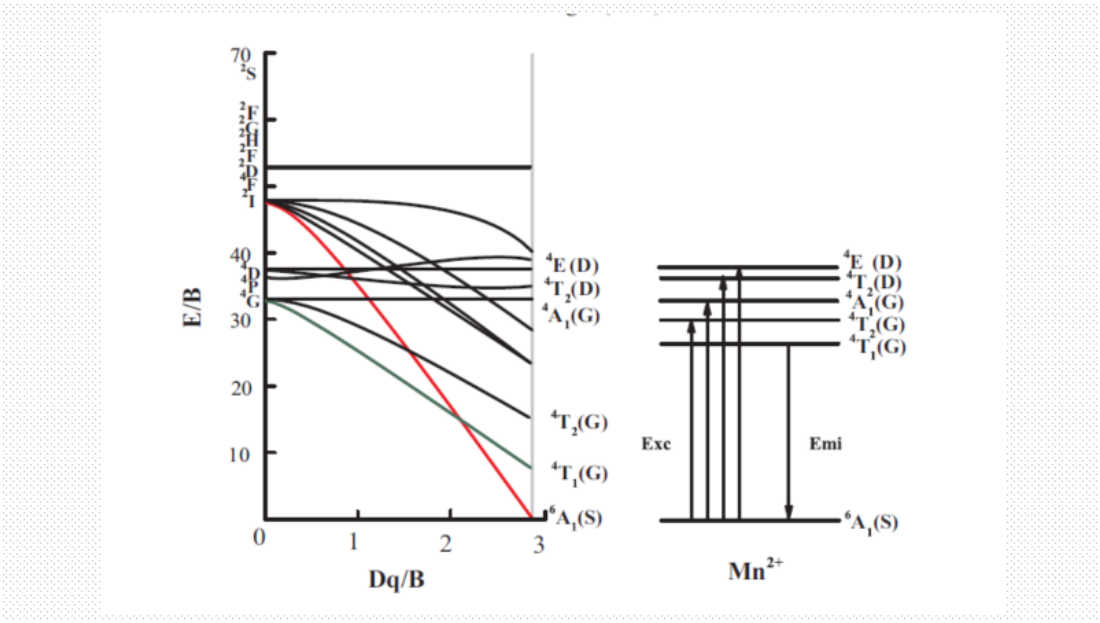

Figure 1.12: A schematic diagram showing energy levels of the Mn^{2+} ion [49].

During excitation, electrons will enter the conduction band of the host material and the lowest excited state $^6T_1$ leaving behind holes in the valence band and the ground state $^6A_1$ of Mn^{2+}. The subsequent recombination of these electrons with holes in the ground state of Mn^{2+} results in photoluminescence.

REFERENCES

1. K. N. Shinde, S.J. Dhoble, H.C. Swart, K. Park, Phosphate Phosphors for Solid-State Lighting, Springer-Verlag, Berlin, 2012.

2. W. M. Yen, M. J. Weber, Inorganic Phosphors: Compositions, Preparation and Optical Properties, CRC Press, New York, 2004.

3. D. L Dexter, A theory of sensitized luminescence in solids, Journal of Chemical Physics J. Chem. Phys, 21 (1953) 836-50.

4. John C. Lindon, Geoge E. Tranter, David W. Koppenaal, Encyclopedia of Spectroscopy and Spectrometry, Academic Press, UK, 2016.

5. D. Phillips, A lifetime in photochemistry; some ultrafast measurements on singlet states. Proc. R. Soc. 472, 2016.

6. S.W.S Mckeever, Thermoluminescence of Solids, Cambridge University Press, USA, 1985.

7. C. M Sunta, Unraveling Thermoluminescence, Springer, New York, 2014.

8. M. Oberhofer, A. Scharmann, Techniques and Management of Personnel Thermoluminescence Dosimetry Services, Springer Science & Business Media, Luxembourg, 1993.

9. Pagonis, G. Kitis, C. Furetta, Numerical and Practical Exercises in Thermoluminescence, Springer, USA, 2006.

10. Rasheedy M.S, Amry A.M.A, On the frequency factor obtained in case of thermoluminescence second order kinetics, J. Lumin. 63 (1995) 149 –154.

11. Reuven Chen, S. W. S. McKeever, Theory of Thermoluminescence and Related Phenomena, World Scientific, Singapore, 1997.

12. S. bhushman, P.K. Dewangan, Luminescence and Its Applications 97: Proceedings of the National Conference on Luminescence and Its Applications 97 (NCLA-97), Allied Publishers, Mumbai, 1997.

13. John C Lindon, George E. Tranter, David W. Koppenaal, Encyclopedia of Spectroscopy and Spectrometry, Academic Press, UK, 2016.

14. E. W. Williams, R. Hall, Luminescence and the Light Emitting Diode: The Basics and Technology of LEDS and the Luminescence Properties of the Materials, Pergamon Press Ltd, U.K, 2016.

15. Nicholas J. Turro, Modern Molecular Photochemistry, University Science Books, USA, 1991.

16. https://ars.els-cdn.com/content/image/3-s2.0-B0122266803001605-gr2.gif?_/27/03/2019/ 13:51.

17. Joseph R. Lakowicz, Principles of Fluorescence Spectroscopy, Springer Science & Business Media, USA, 2007.

18. M. Sauer, J. Hofkens, J. Enderlein, Handbook of Fluorescence Spectroscopy and Imaging: From Ensemble to Single Molecules, WILEY-VCH Verlag GmbH & Co.KGaA, Germany, 2011.

19. Bernard Valeur, Mário Nuno Berberan-Santos, Molecular Fluorescence: Principles and Applications, John Wiley & Sons, Germany, 2013.

20. D. R. Vij, N. Singh, Luminescence and Related Properties of II-VI Semiconductors, Nova Publishers, New York, 1998.

21. E. Roland Menzel, Laser Spectroscopy: Techniques and Applications, CRC Press, New York, 1994.

22. A. Sillen and Y. Engelborghs, The Correct Use of “Average” Fluorescence Parameters, J. Photochem. Photobiol. 67(5) (1998) 475-486.

23. M. Gabba, Interdomain Functional Dynamics of Phosphoglycerate Kinase Studied by Single-Molecule FRET, Jülich, FDorschungszentrum Jülich GmbH, Jülich, Jülich, 2014.

24. Yehoshua Y. Kalisky, The Physics and Engineering of Solid State Lasers, SPIE Press, USA, 2006.

25. https://arxiv.org/ftp/arxiv/papers/0908/0908.1815.pdf/2019/05/28

26. Jacques I. Pankove, Optical Processes in Semiconductors, Courier Corporation, New Jersey, 2012.

27. David C. Jiles, Introduction to the Electronic Properties of Materials, 2nd Edition, CRC Press, London, 2001.

28. http://www.springer.com/9780387256535-c1.pdf/2019/02/08.

29. Johann-Martin Spaeth, Harald Overhof, Point Defects in Semiconductors and Insulators: Determination of Atomic and Electronic Structure from Paramagnetic Hyperfine Interactions, Springer, Verlag Berlin, Heidelberg New York, 2003.

30. Golla Eranna, Crystal Growth and Evaluation of Silicon for VLSI and ULSI, CRC Press, New York, 2015.

31. Peter Rudolph, Handbook of Crystal Growth: Bulk Crystal Growth, Elsevier, USA, 2015.

32. https://en.wikipedia.org/wiki/Crystallographic_defect#/media/File:Defecttypes.png/2019/01/29.

33. C. N. R. Rao, J. Gopalakrishnan, New directions in solid state chemistry. 2nd edition, Edition en anglais, Cambridge University Press, United Kingdom, 1997.

34. M. Lannoo, Point Defects in Semiconductors I: Theoretical Aspects, Springer, Verlag Berlin Heidelberg, 1981.

35. Harald Ibach, Hans Lüth, Solid-State Physics: An Introduction to Principles of Materials Science, Springer-Verlag Berlin Heidelberg, 2009.

36. https://www.ece.uvic.ca/~ece220/lecture%20notes/ELEC%20220%20Lecture%204%20of%207.pdf/02/05/2019.

37. Andrew Putnis, An Introduction to Mineral Sciences, Cambridge University Press, UK, 1992.

38. Elena R. Dobrovinskaya, Leonid A. Lytvynov, Valerian Pishchik, Sapphire: Material, Manufacturing, Applications, Springer Science & Business Media, New York, 2009.

39. Rajiv Asthana, Ashok Kumar, Narendra B. Dahotre, Materials Processing and Manufacturing Science, Elsevier, UK, 2006.

40. https://www.researchgate.net/figure/Edge-and-screw-dislocations_fig12_313979031/02/05/2019.

41. Daniel M. Fleetwood, Ronald D. Schrimpf, Defects in Microelectronic Materials and Devices, CRC Press, US, 2008.

42. Wei Cai, William D. Nix, Imperfections in Crystalline Solids, Cambridge University Press, United Kingdom, 2016.

43. H. V. Keer, Principles of the Solid State, New Age International, New Delhi, 1993.

44. B.G. Yacobi, Semiconductor Materials: An Introduction to Basic Principles, Kluwer Academic Publishers, New York, 2004.

45. https://www.researchgate.net/publication/303783422_Chapter_defect_formation_during_the_crystal_growth_from_melt/2019/02/07.

46. J. C. Krupa, N. A. Kulagin, Physics of Laser Crystals, Kluwer Academic Publishers, USA, 2003.

47. N Xei, J. Liu, Y Huang, S Kim, H. J. Seo, J.Ceram Internat, 38 (2012)1489-1495.

48. G. S. R. Raju, J. Y. Park, H. C. Jung, B. K. Moon, J. H. Jeong, Curr. Appl. Phys. 9 (2009) 92-95.

49. Cuili Chen, Peiqing Cai, Lin Qin, Jing Wang, Shala Bi, Yanlin Huang, Hyo Jin Seo, Luminescence properties of sodalite-type $Zn_4B_6O_{13}:Mn^{2+}$, Journal of Luminescence, 199 (2018) 154-159.

CHAPTER 2

Experimental Techniques

2.1. Introduction

Inorganic nanomaterials are generally synthesized using two approaches viz. the top-down (physical methods) and the bottom-up (chemical methods), and both approaches play a pivotal role in modern industry and nanotechnology [1]. Typical examples of top-down method involve Attrition or milling, mechanical alloying, severe plastic deformation and lithography. On the other hand, synthesis approaches such as colloidal or wet chemical route, chemical vapor deposition, and green chemistry are typical examples of bottom-up approach [2,3]. Essentially, the bottom-up approach can be thought of as the building up of a material from the bottom: atom-by-atom, molecule-by-molecule, or cluster by cluster [2]. Phosphor materials in this work are synthesized through this bottom-up route.

This is because there is no suitable machinery to synthesise materials at nanoscale level using the top-down approach. On the contrary however, the bottom-up approach is driven mainly by the reduction of Gibbs free energy, so that the produced nanostructures are closer to a thermodynamic equilibrium state, which provides the ability to obtain nanostructures with controlled distribution of defects and more homogeneous chemical composition [2]. To understand and optimize the processes involved in the bottom-up approach to be used in this study, it is imperative for one to have a sound understanding of the theoretical description of such processes. Nucleation theory discussed in the next section is one tool that is very handy in this regard.

2.1.1. Nucleation theory

Nucleation is according to Mulin's 1961 definition, a process of generating a new phase from one phase [4]. In the bottom-up synthesis approach this means

crystallization from a solution, which is also known as phase separation or birth of new crystals [4]. Essentially, to understand the process by which nucleation takes place, the Gibbs free-energy curves in **figure 2.1** can be taken as an example.

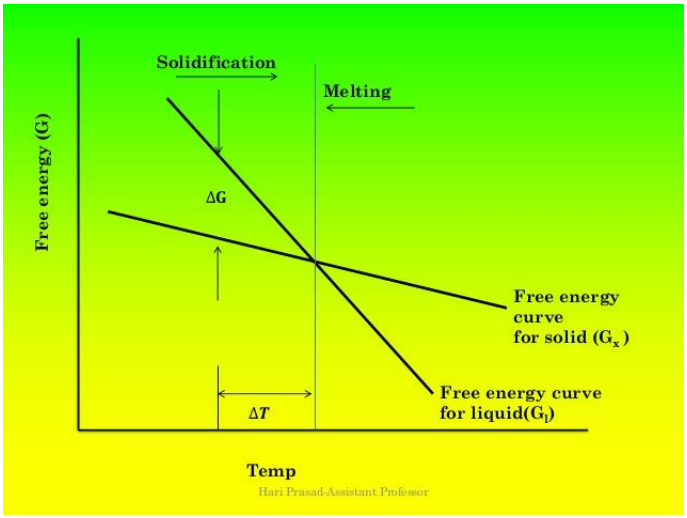

Figure 2.1: The Gibbs free-energy curves for solidification during synthesis process- When a liquid is cooled below the melting temperature, there is a driving force for solidification [5].

At a given temperature, a thermodynamically stable state is the one that has the lowest Gibbs free energy, G. Also, for transformation to take place from one state to another, say liquid-to-solid, there must be an equilibrium temperature where both states have the same Gibbs free energy. For a transformation from liquid-to-solid, this temperature is the melting point as shown in the **figure 2.1**. When comparing the two states (liquid and solid), a liquid has a higher internal energy (heat of fusion) and higher entropy owing to its random structure. As temperature declines towards the melting temperature, T_m, the liquid phase tends to have more order, with a decreased randomness, and the free energy for the liquid rises more faster than that of a solid. At the melting point, the free energy of both liquid and solid are equal. At this stage solidification does not take place however, and this is because the change in free-energy (ΔG) which must be negative is zero. It is only below the melting point that solidification or nucleation

starts to take place. At this state the change in free-energy can be written as in equation 2.1 [6].

$$\Delta G = G_{solid} - G_{liquid} < 0 \tag{2.1}$$

Just below the melting point, solidification occurs at very slow rate, because the free-energy change or driving force is very small. Conversely, at considerable amounts of undercooling, also known as supercooling (T_m - T or ΔT), the driving force is greater, and this results in higher solidification rates. Basically, solidification begins on a small scale at first, with groups of atoms joining together in clusters as illustrated in **Figure 2.2.**

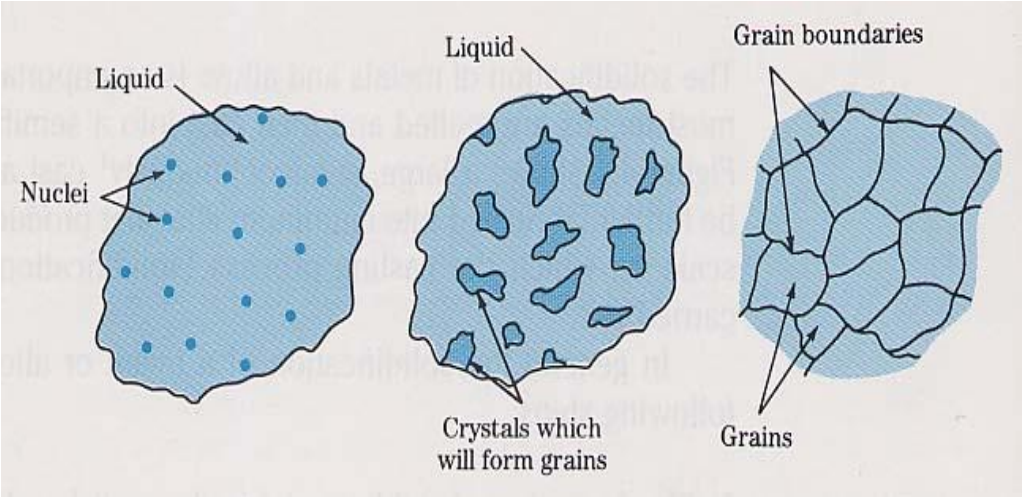

Figure 2.2: Nucleation and grain growth processes during synthesis process [7].

As the temperature falls during solidification process, atoms in the liquid start to get less agitated and slow down into random aggregations of atoms to form into small crystalline regions known as embryos. At this state, these embryos are not yet big enough to become stable and grow, so they constantly form and then re-melt. As temperature declines even further ultimately, some of these embryos reach a critical size and become nuclei which are stable and capable of growing into crystals. These crystals then ultimately grow further until they contact each

other to form grains as shown in **Figure 2.2**. This process of forming nuclei from a solution and grow them may either take place spontaneously or through external stimulation means such as agitation, mechanical shock, scratching of the side of the containing vessel etc. It is hardly possible, however, to determine whether or not nucleation took place due to these external induction means [4,6]. In other words, nucleation can take place via two routes, namely homogeneous and heterogeneous nucleation as discussed below.

2.1.1. Heterogeneous nucleation

This is a type of nucleation which manifests when a solid nucleates from the liquid at certain preferential areas within the bulk of the liquid, with the probability of nucleation not the same throughout the volume of the liquid. In other words, the probability for nucleation to take place at certain areas is more than other areas [2,8].

2.1.2. Homogeneous nucleation

Conversely, nucleation can take place spontaneously in every part of the bulk of the liquid, and this is known as homogeneous nucleation. This is to say that there are no preferential areas in the bulk of the liquid during nucleation. Also, the probability of nucleation is the same throughout the volume of the liquid. Homogeneous nucleation is usually known to take place very rarely and can only be made to take place in carefully controlled laboratory conditions [2,8].

As described in section 2.1.1, in any type of nucleation, embryos grow in nuclei, and nuclei grow to form crystals which will grow to form grains. Now during synthesis, the most important part is whether or not the formed nuclei will survive (grow into crystals). To establish this in a homogeneous nucleation, a formed spherical nucleus of radius *r* within the bulk of the liquid can be taken as an example. For the formation of this nucleus however, there must be an interface between the liquid and solid formed, and because of this, the free energy of the system tends to increase [9]. Also, there must be a surface energy (surface

tension) E_s associated with this sphere of surface area $4\pi r^2$ which is given in equation 2.2.

$$E_S = 4\pi r^2 \sigma \tag{2.2}$$

where σ is the surface energy per unit area, which tends to increase the free energy of the system as depicted in the **Figure 2.3**.

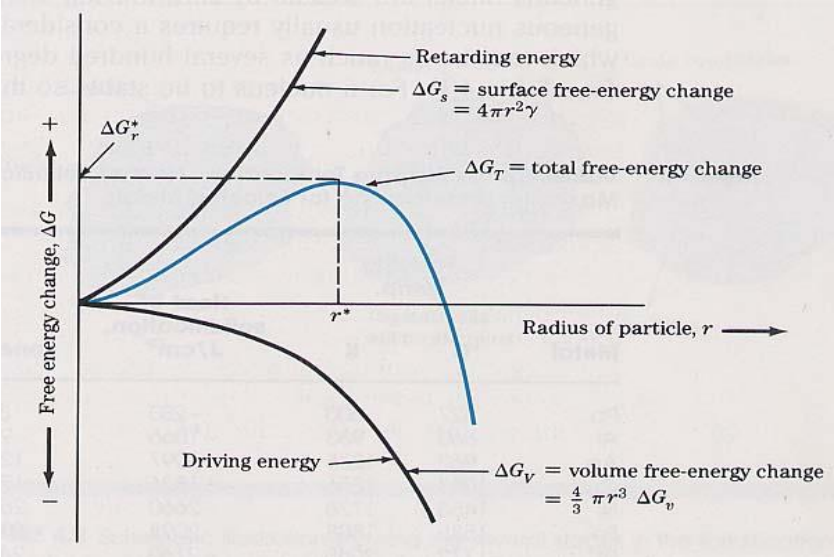

Figure 2.3: A schematic showing free energy as a function of nucleus size during homogeneous nucleation [10].

The contrary holds however, where the free energy of the system decreases as the liquid transforms to solid. The free energy that is responsible for this reduction in the overall free energy as shown in the **Figure 2.3** is known as the volume free energy G_v or rather the energy gained per unit volume by the phase change, which is independent of the radius [9]. For a spherical nucleus of volume $4/3\pi r^3$ this energy is given by $4/3\pi r^3 G_v$. This means for the formation of a spherical nucleus of radius r, the total quantity of work required to form this nucleus is equal to change ΔG in energy of the system as in equation 2.3.

$$W = \Delta G = -\frac{4}{3}\pi r^3 G_v + 4\pi r^2 \sigma \tag{2.3}$$

A closer look at figure 2.3 shows that, for very small, nucleated particles, when increasing them in size from radius *r* to *dr*, more energy is spent on creating surface rather than getting energy from the change in volume. Creating the surface requires energy, it does not give back energy, and this is an unfavourable thing to happen. Beyond the critical radius r^*, which is at the maximum point of ΔG_T curve, the energy that is spent to create the surface is relatively small compared to the energy to be found from transforming a liquid phase to a solid phase. Therefore, these small nucleated particles need to be greater than the critical radius r^* in order for transformation to proceed. In other words, an initial nucleus must be bigger than the critical radius in order for it to grow further. Conversely, if it is smaller than the critical radius, it will shrink. From here, it is then easy to work out what the size r^* and the energy of formation W^* of the critical nucleus must be, by finding the maximum of the ΔG_T curve by differentiating it as in equation 2.4 and replacing r with r^*.

$$d\Delta G/dr = 0 \Rightarrow Gv = 8\pi r\sigma/4\pi r \Rightarrow r^* = 2\sigma/Gv \tag{2.4}$$

Finding what W* is, the value of r* can be substituted back into the original equation 2.3 to yield equation 2.5.

$$W^* = -\frac{4}{3}\pi(2\sigma/G_v)^3 G_v + 4\pi(2\sigma/G_v)^2\sigma = \frac{16\pi}{3}\frac{\sigma^3}{G_v} \tag{2.5}$$

To nucleate one phase from another, usually the critical parameter to play around with is temperature. Now to have a clear insight of what happens as the temperature is varied one can think from a thermodynamic point of view, a driving force, through the help of Gibbs free energy ΔG in equation 2.6 [6,9].

$$\Delta G = \Delta H - T\Delta S \tag{2.6}$$

where ΔH is the enthalpy, T is the temperature, and ΔS is the entropy. Now at the equilibrium temperature, T_e, that is at the phase boundary, ΔG=0.

Therefore,

$$\Delta H = T_e \Delta S \tag{2.7}$$

Substituting this back into equation (2.6) then gives equation (2.8),

$$\Delta G = T_e \Delta S - T\Delta S = \Delta S(T_e - T) = \Delta S \Delta T \tag{2.8}$$

ΔT is the undercooling, also known as the super-cooling. Now from here it becomes simple to tell what happens as the temperature changes. For instance, as the undercooling becomes very small, or the temperature T approaches the transformation temperature, G_v in equation (2.5) becomes very small. In other words there is less or no driving force. So, with less driving force, *W** and *r** become very large, in other words the nuclei that need to be processed are very large, which may not necessarily be there. At small undercooling, there might not be any new phase forming. There must be some super-cooling or driving force in order for small nuclei that already formed to act as nucleation sites to grow new particles.

The other way to say this is, if there are no particles to nucleate new particles from, nucleation becomes very difficult, and if there are some particles in a solution to act as nucleation sites, then nucleation becomes very simple. This is the reason why homogeneous nucleation is very difficult compared to heterogeneous nucleation [6,9].

2.1.2.1. Homogeneous nucleation rate

Usually, during the bottom-up synthesis, the formation of dimensional shapes (morphologies) of these nanomaterials from a solution state can be controlled by two ways viz. thermodynamic or kinetic route [11]. The morphologies that are thermodynamically controlled essentially form when the reaction was driven by the chemical potential of the reaction solution, and this chemical potential has a

direct relation with the temperature and supersaturation of the solution [11]. The kinetically controlled morphologies on the other hand, are usually acquired with the help of the variation of reaction conditions, which will be discussed in detail in the next sections.

Basically, these morphologies form when freshly produced embryos and already formed embryos (small number) are in rapid collision in local, high supersaturated regions for nucleation to occur [9]. Although, the growth of nuclei that are formed in kinetically controlled synthesis processes contributes largely to the formation of morphologies with anisotropic shapes, a combined effect of both the kinetically and thermodynamically controlled synthesis processes play a significant role in dictating the final shapes of the formed nanostructures [9].

2.1.3. Factors that affect dimensional shape of nanomaterials

2.1.3.1. Kinetic factors

(a). Supersaturation

Supersaturation of a reaction solution in a synthetic process of nanomaterials is normally defined as the difference between the solution concentration and the equilibrium concentration ($\Delta C = C - C_{eq}$) [12]. In a reaction solution which is composed of precursor monomers together with reductants, solvents, stabilizer, etc., this refers to a precursor monomer concentration in a single or multi precursor monomer solution system [9]. In synthetic processes of nanomaterials, supersaturation plays a monumental role in determining the nucleation and growth rates, and hence the final shapes on the nanoparticles. The LaMer diagram in **Figure 2.4** schematically demonstrates how supersaturation plays a role in dividing nucleation and growth of nanoparticles into two separate stages in order to achieve monodispersed nanoparticles from a solution state system [9,13].

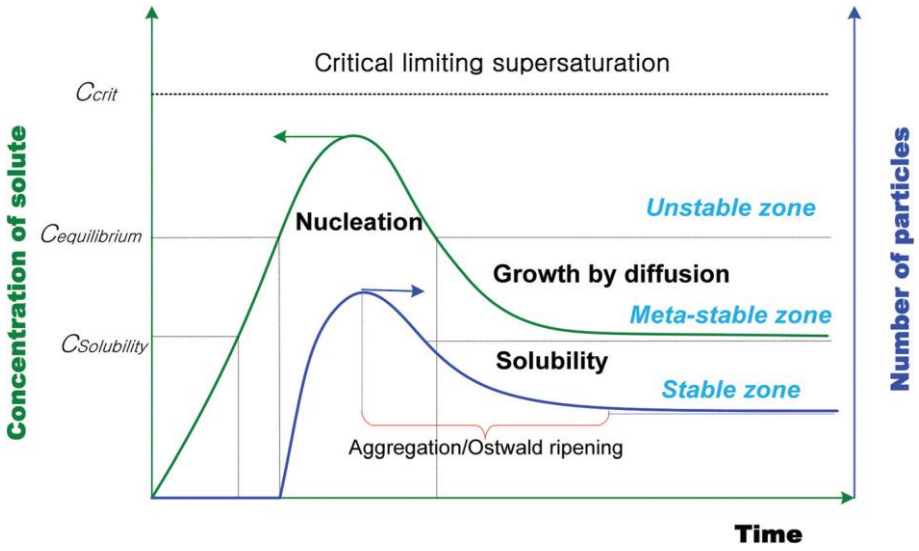

Figure 2.4: Schematic representation of the LaMer model of nucleation and growth [9].

At the beginning of the reaction after precursors are mixed (or dissolved), the concentration of free monomers in the solution builds up rapidly to supersaturation level. As the degree of supersaturation surpasses the critical nucleation threshold, nucleation takes place. At this stage free monomers concentration in the reaction solution decreases sufficiently, and the number of solid particles increase quickly. This reduces the degree of supersaturation. If the nucleation rate surpasses that of monomer formation, the monomer concentration will fall back below the nucleation threshold as shown in figure 2.4 [14,9].

After this stage the preformed nuclei may grow via several pathways. Firstly, via monomer addition, a process through which additional precursor units are deposited onto the preformed nuclei from reaction solution. The second way in which these nanoparticles may grow is through the Ostwald ripening, in which nuclei which are energetically disfavoured tend to re-dissolve and get deposited onto the more thermodynamically stable larger nuclei. Lastly, these nanoparticles may grow through aggregation, in which numerous particles come together and bond.

All these processes and other mechanisms may take place among preformed nuclei to reduce the number of solid particles until the equilibrium state of the solution is reached [15]. Isotropic shapes such as 0D spherical, pseudo-spherical etc. are usually attainable if during growth process, the formed nuclei develop into low energy nanoparticles by supplying enough energy to the solution or by having low concentration of precursor monomer under thermodynamic control [9]. There are a number of parameters that can be varied, as discussed in the next sections, in order to directly adjust supersaturation, and hence control the dimensional shapes of nanoparticles.

(b). Precursor Concentration and additives

In a seed-mediated synthesis, it is crucial to directly alter supersaturation of the reaction solution with the purpose of separating nucleation from the growth process, thereby controlling the size distribution and shapes of the prepared nano-particles [16]. The Lamer mechanism predicts that there is a critical size for a given concentration at which the precipitation and dissolution rates of particles are the same. Particles which are smaller than the critical size dissolve via the Ostwald ripening mechanism and widens the distribution of size. At higher concentration just below the nucleation concentration, the growth rate of nanoparticles is dominated or controlled by the diffusion-controlled growth, in which the precursors are conveyed from the bulk solution and precipitated onto the surface of the preformed particles [16]. Generally, in a seed-mediated synthesis method, the growth mechanism and size distribution, hence particle shape can be controlled by using different addition rate of reaction precursors. For instance, Ho and co-workers have reported the change of Fe_3O_4 nanoparticles from cubic to rhombicuboctahedral shapes by tuning the monomer concentration [17].

Also, the reductant concentration is one of the most important parameter to be tuned in order to control the shapes on nanoparticles. In particular, the amount of precursor relative to the reductant is known to be a very crucial parameter to control the depletion rate of precursor monomer for formation of inorganic

nanoparticles [9]. Tan and co-workers managed to synthesise Monodisperse Spherical, Ellipsoidal, and Elongated Hematite α-Fe_2O_3 Nanoparticles by tuning the Ascorbic Acid to Fe(III) ratio [18].

(c). pH of the reaction solution

Adjusting pH is also another route to modulate the shapes of nanoparticles. This is usually done by introducing an acid or base to the reaction solution, to either stimulate or delay supersaturation of the reaction solution, thereby allowing for the modulation of initial nucleation rate for shape control [19]. This takes place because the addition of acid or base in a reaction solution tend to temper with the state of chemical species in the solution and coordination bonding ions in the precursor monomer solution to form a complex [9]. Sugimoto and co-workers have demonstrated the modulation of the anatase TiO_2 shapes from pseudocubes to ellipsoids using triethanolamine (TEOA), the effect of which was pH dependent when varying the pH [19].

Worth noting also, is that pH adjustment also affects the surface properties of the pre-formed nano-particles, together with the chemical and physical states of the surfactants or additives, giving rise to different adsorption modes or amounts on the surface of the preformed nanoparticles [20]. Consequently, selective growth or aggregation and self-assembly tend to favour the shape evolution of inorganic nano-particles.

(d). Solvents

Supersaturation can also be modified through the incorporation of solvents with different functional groups such as ionic liquids into the reaction mixture during synthesis, thereby providing an opportunity to modulate the dimensional shapes of nanoparticles. These types of solvents provide special coordination with the precursor monomer, which then provide an advantage to thermodynamically or kinetically manipulate the shapes of nano-particles [9]. This is one of the simplest method through which T. Wang and co-workers [21] managed to manipulate the shapes of ZnO particles from double-end clean-cut hexagonal prism to porous

loose rough sphere morphology, by adjusting the ratio of a water-ethylene glycol solution.

(e). Surfactants

Using surfactants during synthesis of inorganic nanoparticles is another way to control nucleation and growth and thereby provide the opportunity to modulate the morphology of nanoparticles. Essentially, during synthesis, inorganic nanoparticles tend to aggregate and form bigger particles with irregular and undesirable morphologies due to their high surface energy and that is an unwanted thing to happen. So, to circumvent this and safely modulate shapes of particles, surfactants can be employed. Surfactants help modulate shapes by adsorbing onto some facets of the growing nanoparticles to reduce their surface energy and provide a controllable growth rate of specific facets for desirable morphologies [9].

In general, surfactants are made up of functional groups or coordinating groups which act as capping agents to adsorb onto the surface of the growing nanoparticles. Of very importance when selecting these capping agents is the adsorption ability and stability of the functional groups. The most commonly used capping agents for shape modulation are small molecules and polymers such as hydroxyl groups, thiol groups, and long alkyl chains. Typical polymers that are used for shape modulation include poly(vinylpyrollidone), poly(acrylic acid), poly(ethylene glycol) etc. Small molecules include (CTAB) cetyltrimethylammonium bromide, cetylmethylammonium chloride (CTAC), trioctylphosphine (TOPO), trioctylphosphine (TOP) [9].

2.1.3.2. Thermodynamic factor

Reaction temperature — Supersaturation can also be modified thermodynamically through the variation of reaction temperature, thereby providing another route to tune the morphology of inorganic nano-particles. When temperatures of a reaction solution are elevated, molecules in the solution tend to move very fast destabilizing the solution due to an increased Gibbs free energy [9,22]. This

causes the supersaturation rate in the solution to increase rapidly, with a consequence of shortening both the nucleation and grow processes due to increased nucleation and growth rates. The most favourable dimensional shapes of inorganic nano-particles under these synthesis conditions are usually pseudo-spherical or spherical morphologies [22,9]. Puvvada et al. [23] reported the morphological change of Hydroxyapatite (HA) nanoparticles from needle-shaped to spherical morphology as the reaction temperature was raised.

2.2. Synthesis methods.

2.2.1. Precipitation Method

Chemical Precipitation method is basically a synthesis method by which a product as an insoluble salt is precipitated from mixing of two solutions containing soluble salts [24]. There are two ways in which a precipitate can be obtained as the final product. In the first one, the products from the reaction are insoluble in the solvent used and tend to precipitate when the reactions come to completion. In the second one, the products can dissolve in the solvent as starting materials. The precipitant is then being added to the mixture to precipitate the products from the reaction.

In the solvent–precipitant–product mixture, only the solvent and the precipitant are miscible, so that the products remain as precipitate. Because, the solubility is depending on a pH value, the precipitation process is also sensitive to pH value [24]. This is one of the convenient wet chemical methods of synthesizing ceramic nanomaterials in that, starting materials can be mixed at the atomic level [25]. Basically, the precipitation method involves a few steps as illustrated in **Figure 2.5**.

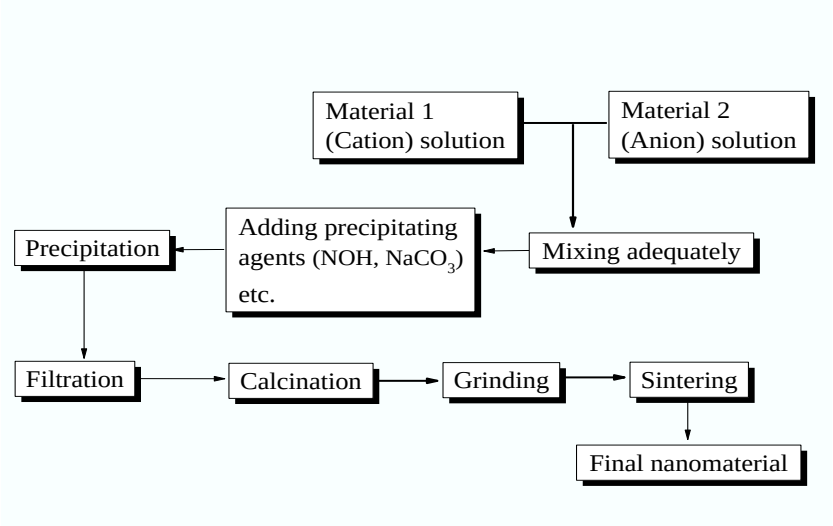

Figure 2.5: Schematic illustration of co-precipitation method procedure of synthesizing nanomaterials.

Firstly, the reagents to make the salt are put in place and mixed with solvents. This main solution is usually made by dissolving reagents such as metal oxide; metal hydrates; metal salts or organometallic compounds in solvents such as deionized water, ethanol, methanol etc. vigorous stirring is usually necessary for a complete reaction of the starting materials. The formed precipitate is then filtered, collected, washed using distilled water, and dried with filter paper.

2.2.2. Combustion synthesis method

Combustion synthesis method can be defined as a rapid exothermic, self-propagating reaction process of synthesising nanoscale materials [26]. Many ceramic powders of nanoscale size used in different applications can be synthesised using this method. For instance, ceramic oxide such as XAl_2O_4 (X = Sr, Ba, Mg, etc.) can be synthesized by mixing metal nitrates (oxidizer) in aqueous solution with urea ($NH_2CO(NH_2)$ or glycerine ($C_2H_5NO_2$) as a fuel, reducing and complexing agent of the metal ion in the solution [26]. The precursors are then mixed thoroughly in a crucible to obtain a homogeneous solution and put into the muffle furnace that is usually set to high temperatures lower than that of phase transition of the target materials, typically around 500 ^oC [27]. After some time,

typically three to five minutes, the mixture boils, decomposes, dehydrates, and raptures into a flame as shown in **figure 2.6**. The mixture continues to burn in a flame for plus or minus 15 seconds [28] and forms a foamy crystalline final powder product which occupies the whole volume of reaction container (crucible) as demonstrated in **figure 2.6** [29]. The whole process from start to finish is demonstrated in **figure 2.6.**

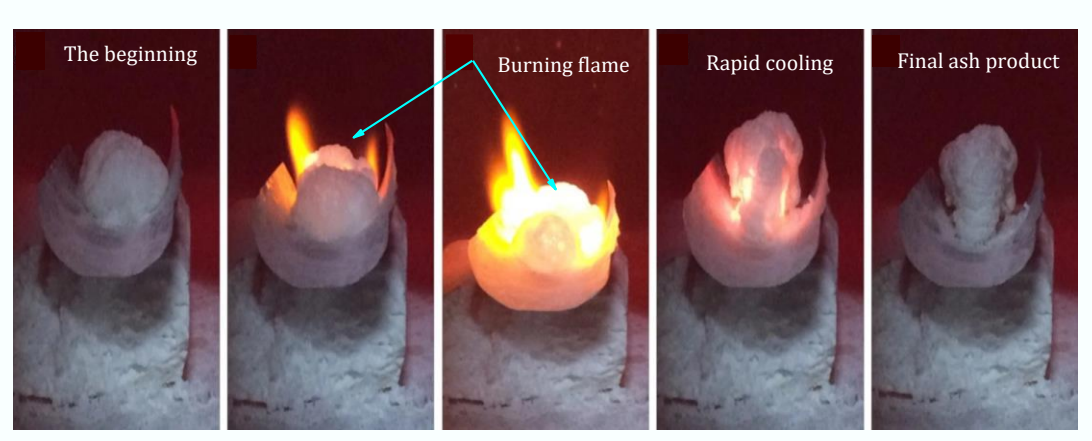

Figure 2.6: A typical combustion synthesis process of ceramic oxide powders [30].

In combustion synthesis method, gases such as N_2, CO_2, and H_2O escape from the reaction mixture during the synthesis process [27]. When these gases escape from the reaction mixture, heat is also being extracted from the reaction and this caters for an ideal environment for the formation of fine crystallite final powder products. This is among other reasons, why combustion synthesis method is even more preferable in the production of ceramic oxide powders [26]. Typically, the escape of gases, results in large clusters being broken, which creates pores between particles which enhance more heat extraction from the reaction mixture and this results in an obstruction of growth of the particles [26], which finally results in small particles with increased surface area of the ceramic oxide powders [27]. Both crystallinity and surface area of the resultant powder are heavily reliant upon the ignition temperature (furnace temperature). For instance, the heating rate of the reactants does depend on the temperate of the

furnace [26]. When the temperature is high, the reaction mixture in the crucible tends to boil swiftly, and this increases the chances of residual water at the time of ignition which in turn affects the flame temperature by lowering it. This reaction condition results in a poorly crystallised final powder [27]. In contrast though, failure of combustion method may result when the furnace temperature is very low, and this is a result of gases escaping from the reaction mixture at very low rate [27].

During the reaction process, high reaction temperature is generated from within the reaction itself, which can volatilize impurities that have low boiling point and result in the formation of more pure products, which adds to other advantages of the combustion method [29]. Another advantage of combustion method is brought by its simplicity, and low processing costs. Also, it is possible to achieve fine, homogeneous, and highly crystalline as-prepared powders via this synthesis technique [26,31].

2.2.3. **Hydrothermal Synthesis Method**

Over and above the conventional methods discussed in the preceding sections, this work also employed the hydrothermal synthesis method to synthesize the silicate-based nanomaterials. This is a non-conventional synthesis method, which can be described as any heterogeneous reaction taking place in the presence of aqueous solvents under both high pressure (> 1 bar) and high temperature (> 100 ^{o}C) conditions. In other words, the reactants dissolve and react with each other in water as a solvent above critical temperature and pressure. These conditions are key to this method in that, even materials that are almost insoluble under normal conditions tend to dissolve and later recrystallize under high pressure and temperature [32].

Hydrothermal synthesis method first emerged in the 19th century, when a British geologist sir Roderick Murchison carried out simulations of the natural conditions existing underneath the earth's crust in order to describe the action of

water at high pressure and temperature, causing changes in the earth's crust, which led to the formation of different rocks and minerals [32]. It is now applied in the synthesis of many inorganic materials such as complex oxides, silicates, germanites, phosphates, chalcogenides, carbonates, including LEDs phosphors. This is one of the synthesis methods in which particle size and morphology can be easily controlled via nucleation, growth, and Oswald aging processes to fulfil requirements of phosphors production [33]. In hydrothermal synthesis method, crystal growth takes place in a specially sealed reaction vessel called the autoclave as depicted in **Figure 2.7**, under subcritical of supercritical conditions of the solvent [34].

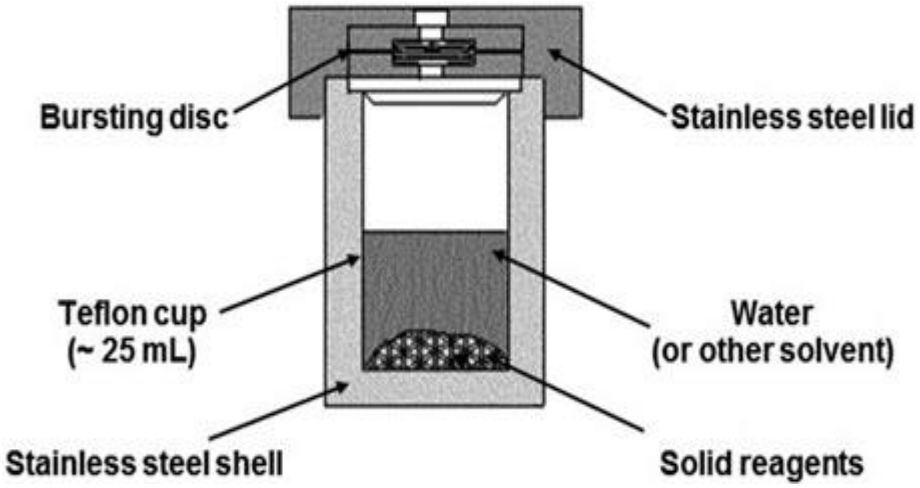

Figure 2.7: A Schematic representation of a typical Teflon-lined stainless steel autoclave used for hydrothermal synthesis in the lab [35].

In this reaction vessel, various parameters can be varied to modulate the dimensions of nanoparticles. Temperature as one of them plays a very vital role in thermodynamic stability of the phase of the product and in the kinetics of product formation, so reaction temperature can be varied to modulate particle dimensions of the material. Pressure is also one of the vital parameters and is very crucial for solubility of reactants, the supersaturation range directing the crystallization process. For example, at very high pressure, crystallization of denser phases does result [36].

Additionally, other parameters such reaction time, type of solvent, pH of the reaction solution, types of capping agents and surfactants can also be varied in this method. Notwithstanding the very interesting advantages that this method has such as the possibility to create highly crystalline phases at much lower temperature, the possibility to synthesize agglomeration free materials, also, fine grained with high purity and controlled morphology is possible through this synthesis method. There are two drawbacks attached to this method. It requires expensive autoclaves, and the impossibility of monitoring the crystals as they grow [37].

2.3. Characterization techniques

2.3.1. Scanning Electron Microscope

The Scanning Electron Microscope is a flexible characterization technique that uses high energy electrons to study and analyse the microstructure morphology of different materials [38]. The technique is composed of four fundamental components, namely the electron gun, the specimen stage, electron beam scanning coils and signal detector. A schematic diagram of SEM presented in **figure 2.8** clearly shows all the key components of the SEM technique.

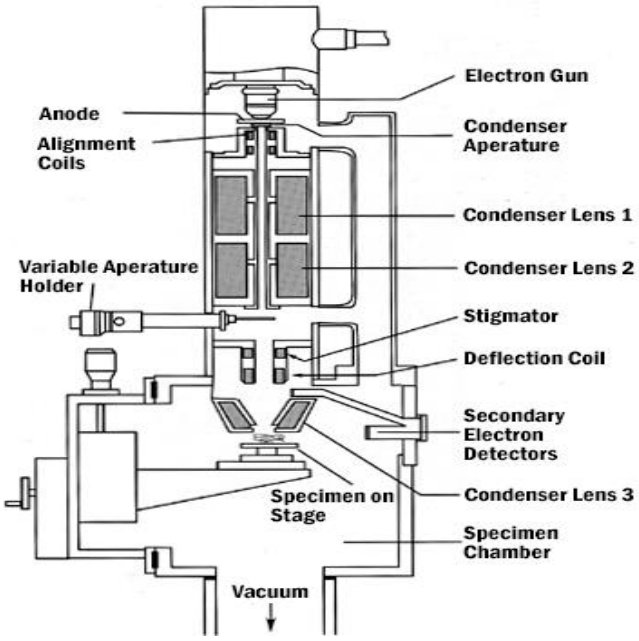

Figure 2.8: A schematic diagram of Scanning Electron Microscope illustrating the electron beam path starting from the electron gun to the specimen and all the basic components [39].

In a typical data acquisition experiment, a high energy beam of electrons generated by electron sources, usually tungsten filament cathode or lanthanum hexaboride (LaB_6) inside the gun, is focussed onto the sample to be scanned across the sample as illustrated in **figure 2.9** [38].

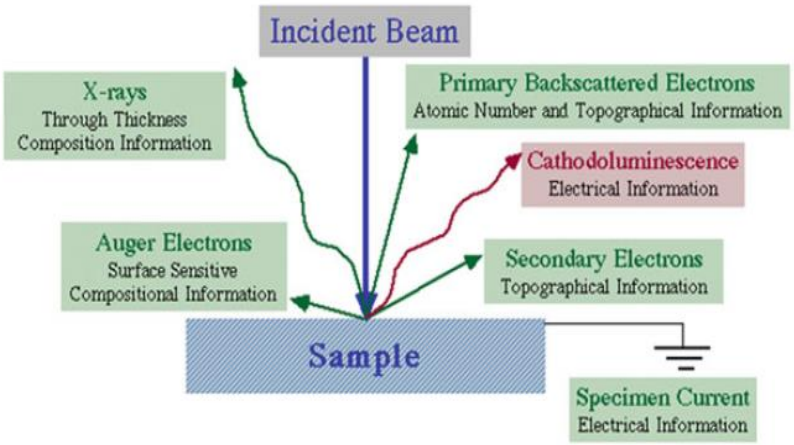

Figure 2.9: A schematic illustration of the interaction between the surface and the sample to produce different signals for surface analysis [40].

A focussed high energy beam then interacts with the surface of the sample. This sample-surface interaction then generates several signals which escape the surface of the sample. Those signals are low energy secondary electrons, back-scattered electrons, cathodoluminescence, transmitted electrons, and characteristic X-ray emission [40]. The surface topography and characteristic features of the sample are studied from these signals after being collected using the appropriate detectors. For example, the secondary electrons are usually collected by a scintillation-photomultiplier system [41].

In principle, the surface of the sample can be probed in three ways during SEM measurements, namely by detection of secondary electrons, backscattered electrons, and characteristic X-rays [40]. Texture and roughness of the sample surface are usually visualised from secondary electrons, whereas backscattered electrons are usually detected for the purpose of examining both compositional and topographic information about the sample being studied. The characteristic X-rays and Auger electrons are both useful for providing chemical information about the sample. Transmitted electrons are very crucial for studying the elemental information and distribution when coupled with X-ray microanalysis [42].

2.3.2. X- Ray Diffraction

X-ray diffraction spectrometer (XRD) can be described as a technique which is widely used for phase identification, determination of phase compositions and estimation of particle size of crystalline materials. The crystalline materials which can be studied using this technique can be powders, ceramics, polymers and metals [43]. This type of a spectrometer only evolved after the discovery of the diffraction of X-rays from crystals by Max Laue [44]. Basically, the generated X-rays from the X-ray tube are monochromatized by a foil or a crystal monochromator and directed onto a sample which is crystalline in nature [45].

In the case where these X-rays are diffracted constructively by the crystalline sample and obey the Bragg's Law, $n\lambda = 2d\sin\theta$, they will be detected, processed, and counted. Usually, scanning a crystalline sample through a range of 2θ angles shows all possible diffraction peaks associated to planes of the sample's crystal lattice. The resulting spectrum can be compared with standards to identify the material under study. There are three fundamental components of which the X-ray diffractometer is comprised as depicted in **figure 2.10,** namely, X-ray source (generator), goniometer and X-ray detector. The goniometer positions the sample relative to the detector [46].

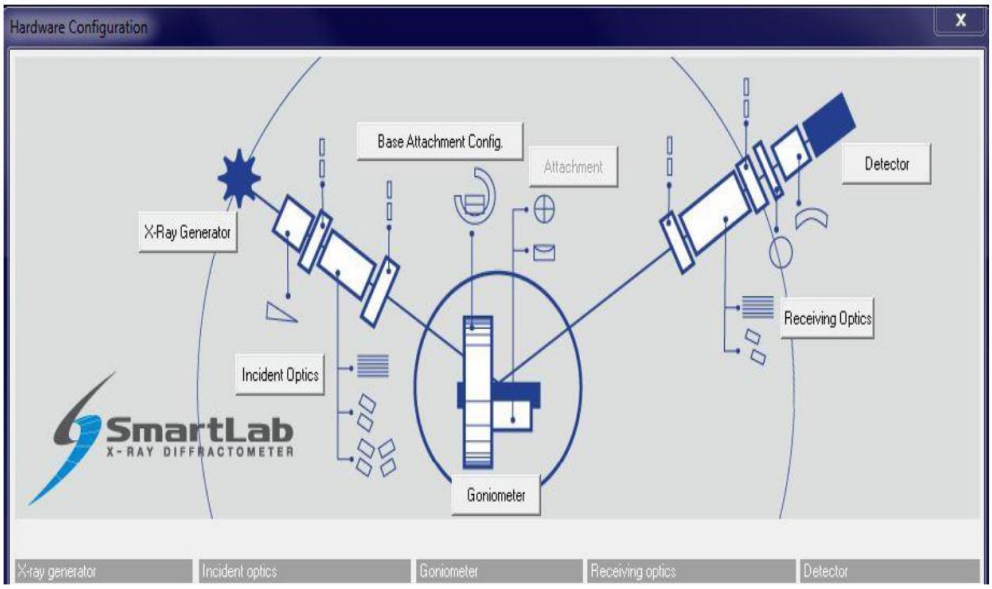

Figure 2.10: A schematic illustration of a typical X-ray diffractometer [47].

In this study, SmartLab X-ray diffraction spectrometer was used in confirming the prepared materials after the synthesis processes. By comparing the spectra results from the prepared samples with the standards, the envisaged materials are confirmed. This sophisticated technique allows the possibility of confirming whether the synthesized materials are single-phased, or more than one phase coexist in the prepared samples.

2.3.3. X-ray photoelectron spectroscopy

This is an x-ray spectroscopic, surface characterization technique which is used to acquire information about elemental composition and chemical bonding states of samples [48]. It was first demonstrated by Dr. Siegbahn in 1954, because of which he was awarded a Nobel Prize in 1981. His demonstration followed the tremendous work of the first formulation of the basic XPS theory in 1914 by Ernest Rutherford. Rutherford's formulation was made a success by Hendrick Rudolf Hertz's first discovery of photoelectric effect in 1887, a phenomenon on which XPS is based [49].

Basically, XPS analyses the sample's surface by mapping photoelectrons ejected from the core shells of elements in the sample. The signals of these photoelectrons then provide information about all elements in the sample except hydrogen and helium [50]. Typically, in an XPS experiment, X-ray photons from the x-ray gun are projected onto the sample as shown in **figure 2.11** and penetrate it to excite core shell electrons of elements in the sample.

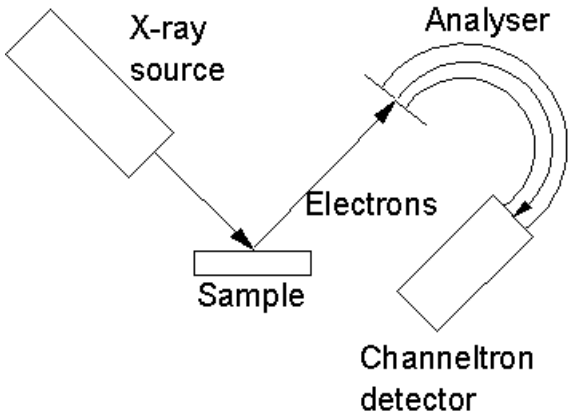

Figure 2.11: A schematic illustration of X-ray photoelectron spectroscopy [51].

The x-ray photons give these electrons enough kinetic energy to break away from nuclear attraction force and escape from different bound states in the elements to the surface of the sample. Some undergo inelastic scattering and lose energy on their way to the surface of the sample, while some escape the surface of the sample without losing energy [50].

However, all these electrons escape the surface with different kinetic energies to the surrounding vacuum, where they get collected by the electron analyser as shown in **figure 2.11** to measure their kinetic energies. A spectrum of the number of photoelectrons reaching the analyser versus the energy required to knock these electrons off the core shells of the elements in the sample is then acquired. In other words, a spectrum of intensity of photoelectrons on the y axis versus the binding energy of these electrons on the x axis is acquired.

Each peak on the binding energy axis is then a representative of a particular element, except the X-ray independent, asymmetric peaks on the spectrum that are due to signals from Auger electrons [52].

The Information regarding characteristic peaks on the spectrum is carried by photoelectrons that did not undergo scattering, while the ones that underwent scattering only contribute to the background of the spectrum [52]

2.3.4. Fourier transform infrared spectroscopy

The Fourier transform infrared spectroscopy (FTIR) is a type of spectroscopy which is focussed on the vibrations of molecules. It is based on the idea that each functional group has its own distinct vibrational energy through which molecules together with their concentration can be identified by a way of a combining all the functional groups. In other words, the infrared (IR) light interacts with the molecules and change the dipole moment of the molecules and this change corresponds to a specific vibrational energy. Samples can be solids, liquids, gases, semi-solids, and mixtures [53,54,55]. The idea of FTIR spectroscopy has been well-known for more than a century. It started with Michelson's invention of the interferometer in the 1880s, which was followed by Lord Rayleigh's idea that the interference pattern generated by the interferometer could be converted into a spectrum through the use of Fourier transformation [56].

The main components of an FTIR are the IR source, an interferometer, and a detector as depicted in **figure 2.12** [57,58,56].

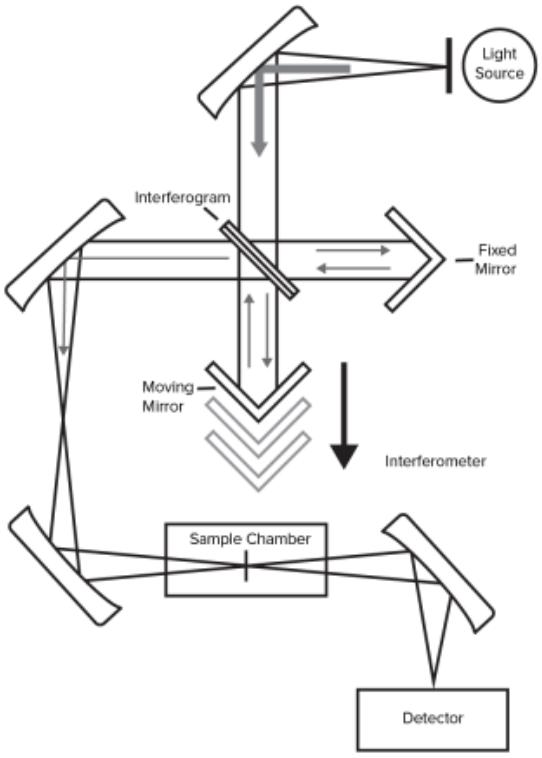

Figure 2.12: A schematic Diagram of an FTIR spectrometer with the IR source, interferometer, and the detector [57]

The FTIR typically uses a broadband emitter as an an IR source. The fundamental part of an FTIR is the interferometer, which is composed of a beamsplitter, a moving mirror, a stationary mirror, and a timing laser. The purpose of the beamsplitter, which is typically positioned at 45 degrees to the incident beam of light from the IR source is to split the beam from the IR source into two paths. Half of the split beam goes to the moving mirror while the other half goes to the stationary one.

A commonly used beam splitter in FTIR systems is KBr. So, as shown in **figure 2.12**, the two split beams are then reflected from the two mirrors to recombine at the beamsplitter with a path difference causing an interference pattern (destructive and constructive), also known as an interferogram. This interferogram is then

sent to the sample to interact with it. The transmitted part of an interferogram is then sent to the detector, from which a Fourier transform is carried out to obtain a full spectrum of transmittance as a function of wavenumber [57,58,56].

The FTIR spectrometer is most preferred over the others due to advantages such as high precision, accuracy, speed, enhanced sensitivity, ease of operation, and sample nondestructiveness. The most basic feature of the FTIR technology lies on atomic vibrations of molecules which only absorbs particular frequencies and energies of infrared radiation [59].

2.3.5. Photoluminescence Spectroscopy

This spectrometer uses photons to examine the electronic structure of materials. It is comprised of four essential components namely, the monochromators (excitation and emission), sample compartment, detectors, and accessories. In photoluminescence experiment, photons of light from the light source, typically xenon lamp, are projected onto a sample as shown in **Figure 2.13** in the sample compartment to interact with it. When energy of these photons selected from the excitation monochromators is absorbed, the ions in the sample move from ground to excited states. One way for these ions to return to their normal ground states is by losing a small fraction of this excitation energy to its lattice as heat and phonons without emitting photons [60].

The other way is by emitting the remaining fraction of energy as photons, though which a phenomenon of luminescence either as fluorescence or phosphorescence (depending entirely on the duration of this emission) can be observed [61].

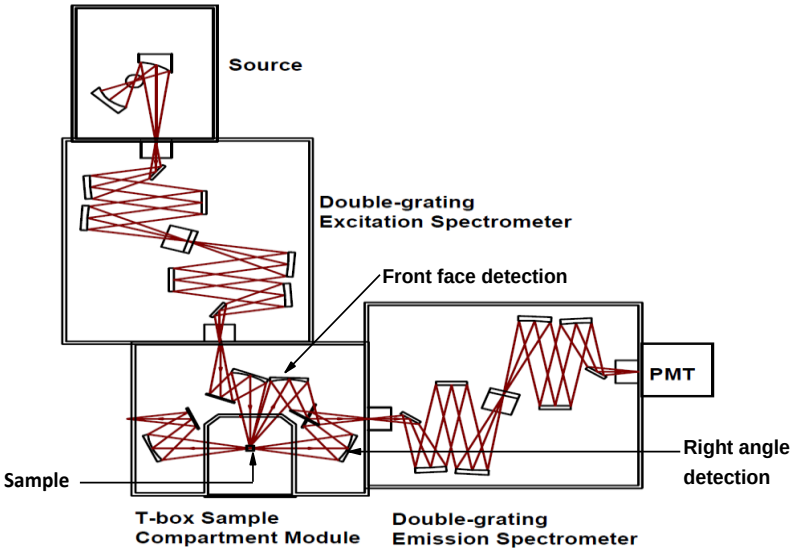

Figure 2.13: A schematic Diagram of a Fluorolog®-3 spectrometer, showing the path of a photon beam from the photon source (xenon lamb) until to the PMT detector [62].

The emitted photons are then detected by a photomultiplier detector. A spectrum of the intensity of these emitted photons arriving at the detector as a function of their energy, typically in wavelength units is then acquired. In this work, the Fluorolog®-3 spectrometer was used to study the physical properties caused by defects that are induced during the synthesis in the spinel silicate and aluminate hosts, in particular, the luminescence properties of the prepared nanophosphors.

This is a very sophisticated system in that, it comes with benefits such as high sensitivity and stray-light rejection, and this owes to its double-grating [62]. Whether or not the emitted light covers the required range on the spectrum for white light applications is confirmed from luminescence spectra acquired from this spectrometer. It is also the major technique of this study. The quality of the envisaged white light, hence quantum yield of the prepared nanophosphors is evaluated using this technique. Below is a brief discussion of steady state and time correlated capabilities of this spectrometer.

2.3.5.1. Excitation and emission spectra

Before checking for the emission colours from the samples being studied, it is imperative that we first examine the spectral dispersion of light absorbed by the prepared samples. In other words, the excitation spectra of the samples need to be acquired. Acquiring an excitation spectrum on this spectrometer involves scanning a selected excitation spectral region while fixing the emission wavelength of the sample at one wavelength position [62]. Typically, the emission wavelength is the one that is fixed at a wavelength which matches with the emission peak of the material.

In principle, the excitation spectra of the material should be the same as the absorption spectra. The problem is, however, the wavelength dependence of the lamp output. For instance, modern spectrofluorometers ordinarily use a xenon lamp as a light source, the output of which is a continuum in the range of approximately 200-1200 nm, with a radiation curve that shows blackbody radiation with a maximum at approximately 550 nm and a sharp decline at short wavelength [63]. A correction of excitation spectra of materials is therefore necessary for the lamp background in order for the excitation spectra to correlate with the absorption spectra.

In other words, this correction is done to get rid of sharp spikes of the xenon lamp between 450 and 500 nm of the excitation spectra. This is usually archived through the use of a quantum counter like rhodamine B, strong luminophore which has a capability to absorb more or less all the incident light over a wide range of wavelength. The procedure of correcting excitation spectra of samples is then done by dividing the uncorrected spectra by the excitation spectrum of the quantum counter [63]. This eventually leaves excitation spectra of many materials very similar to their absorption spectra.

The emission spectra on the other hand are spectra which result from steady state measurements and they provide information about spectral dispersion of light emitted by the samples. Acquisition of these types of spectra on this

spectrometer involves scanning a selected emission spectral region, while keeping the excitation wavelength at a fixed position. The excitation wavelength is usually fixed at a wavelength at which the material has an optimum absorbance [62].

2.3.5.2. Lifetime measurements

This study took advantage of Fluorolog®-3's lifetime fluorescence spectroscopy capabilities, curtesy of Horiba Jobin Yvon, to investigate the change of luminescence from the prepared samples over time when excited with UV light. A brief description of all three different capabilities (modes) is outlined here. These different modes of fluorescence spectrometer make it clear how long luminescence from the samples lasts, hence which samples are suitable for general lighting, and which are suitable for persistent luminescence applications.

2.3.5.2.1. TCSPC mode

This study takes advantage of UNISA's Fluorolog®-3 technique which has a time-correlated single photon counting (TCSPC) capability to evaluate the duration of short luminescence (Fluorescence), usually in nanosecond range, from samples applicable in general lighting. In a TCSPC experiment, the sample is excited with photons from a pulsed source, such as Nano-LED and delta diodes [64]. The sample fluorescence is then collected as single photons arriving at the detector. The arrival of these photons then builds up a histogram, which represents a decay curve from which the duration of samples' fluorescence can be calculated [64].

2.3.5.2.2. *Phos-mode*

In cases where the sample's luminescence (phosphorescence) lasts from microsecond to seconds, the Fluorolog®-3 can be operated in a Phos-mode to accurately evaluate the lifetimes of triplet excited states in the prepared samples. Just like TCSPC mode, the sample is excited with photons from a pulsed source, and the sample phosphorescence is then collected as single photons arriving at the detector. The arrival of these photons then builds up a histogram, which

represents a decay curve from which the duration of samples' phosphorescence can be evaluated. In contrast to the TCSPC however, this mode uses a pulsed xenon lamp source [62].

2.3.5.2.3. Kinetic mode

Fluorolog®-3's kinetic mode is ideal for luminescence that persists from seconds to hours; hence it is for the evaluation of luminescence duration from samples applicable in persistence luminescence. This mode is in contrast with the above modes, using a continuous xenon lamp to excite the samples. In a kinetic mode experiment, two files (batches) are created, namely excitation and emission batches. These batches will then later be executed sequentially. Basically, the excitation wavelength and time of excitation are set while blocking the emitted photons from reaching the detector. In other words, the emission slit is set to zero. This excitation file batch is then saved.

The emission file batch is then created by setting the excitation slit to zero, and opening the emission slit to the width of choice. The emission time range is then set. The emission batch file is then saved. The two files are then browsed and executed sequentially. Starting with excitation file, the system will excite the sample for the time set in the excitation file, stop when the excitation time lapses and close the excitation path. Lastly the emission path is open for decay collection [62].

2.3.6. Quantum yield measurements

When phosphors are excited with photons, excited states are created and populated with electrons. These phosphors usually relax back to the ground states through two ways, namely radiative and non-radiative decays [65]. It is therefore important to determine the ratio of the radiative relaxation (luminescence) processes relative to the non-radiative ones. This ratio is referred to as the quantum yield of a material [66,67]. This is however even more complex on samples from which the emitted luminescence is angular dependent, such as

inorganic phosphor powders, and films [68,69]. To circumvent this challenge, Fluorolog®-3 spectrofluorometer is used in conjunction with a very sophisticated integrating sphere, shown in **Figure 2.14**, referred to as the "*quanta-φ"*, to measure the photoluminescence quantum yields of the samples.

Figure 2.14: The Quanta-φ integrating sphere used for the quantum yield measurements [70].

This integrating sphere integrates all the radiation that enters and produced within it [71]. The interior of the quanta-φ is made by Horiba Scientific's spectralon® which has over 95% reflectance over a very wide range (250 nm to 2.5 μm). This makes the integrating sphere useful from UV through the near-IR scanning range of the Fluorolog®-3 spectrofluorometer.

This approach of using the spectrofluorometer in conjunction with the integrating sphere to measure quantum yield comes with the merit of exciting the samples from the excitation monochromater, where the excitation wavelength can be easily selected, as opposed to the old way of using integrating sphere to measure quantum yield. The old way required a laser as the excitation source, and this limits one to choose the excitation wavelength without constraints. Now,

by employing this new approach the constraints of choosing the excitation wavelength from ultraviolet to the visible parts of the electromagnetic spectrum are relaxed.

In the Fluorolog®-3-quanta-φ system, the quanta-φ is operated external to the Fluorolog®-3 spectrofluorometer with fibre optic cables guiding the excitation beam from the excitation monochromator and emitted photons to the emission monochromator. This means that the need for an independent detection system is also relaxed, since the luminescence from the samples is collected through the emission monochromator to different detectors with great sensitivities in UV, visible and IR regions of the electromagnetic spectrum respectively. Also, the excitation wavelength can be selected within the range 250 nm to 600 nm [62].

There are basically two methods that the Fluorolog®-3-quanta-φ system is using for the calculation of the quantum yield of the phosphor materials. The first method is the use of two curves method. In this method, the two curves are being used to calculate the quantum yield. The two curves used are the scan resulting from only a blank, and the one resulting from the sample plus the blank. Basically, the blank is scanned trough a region covering the excitation wavelength and emission wavelength of the sample (though no sample). The second scan also covers both the excitation wavelength and the emission of the sample. The two spectra are then used together with the solid or solution reference file, depending on the state of the sample to calculate quantum yield.

This first method is however not the best due to the fact that, when calculating the quantum yield, there has to be a consistency when scanning the blank and the sample. The consistency is usually achieved by fixing the slits to a particular bandpass so that the measurements are carried out within the linearity of the spectrofluorometer, i.e. two million counts/seconds for Fluorolog®-3 [62]. Now, fixing slits for the benefit of linearity comes with a price of compromising the signal to noise ratio. In other words, the scan having both the blank and the

sample is usually very noisy on the sample emission region of the electromagnetic spectrum.

This then triggered a need for the four-curves method. What happens in this method is basically that, the two curves in the first method are split in to two to form four curves. The blank is scanned separately through two regions, namely the excitation region and the sample emission of the electromagnetic spectrum to have two spectra. The other two spectra are acquired by scanning the blank with the sample separately through excitation and sample emission region respectively. These four spectra are then used together with the solid or solution reference file, depending on the state of the sample to calculate quantum yield.

2.3.7. Thermoluminescence spectrometer

This is a spectrometer that is used to study the concentration and depths of defects in insulating and semiconducting materials. It has three main components as shown in **Figure 2.15**, namely the irradiation source, luminescence stimulation system, and luminescence detection system. The irradiation is usually done in situ using either X-ray source, alpha source, or beta source [72]. The luminescence stimulation system is composed of a heating element and an optical stimulation component. Themorluminescence (TL) detection system uses a photomultiplier tube which is coupled with detection filters.

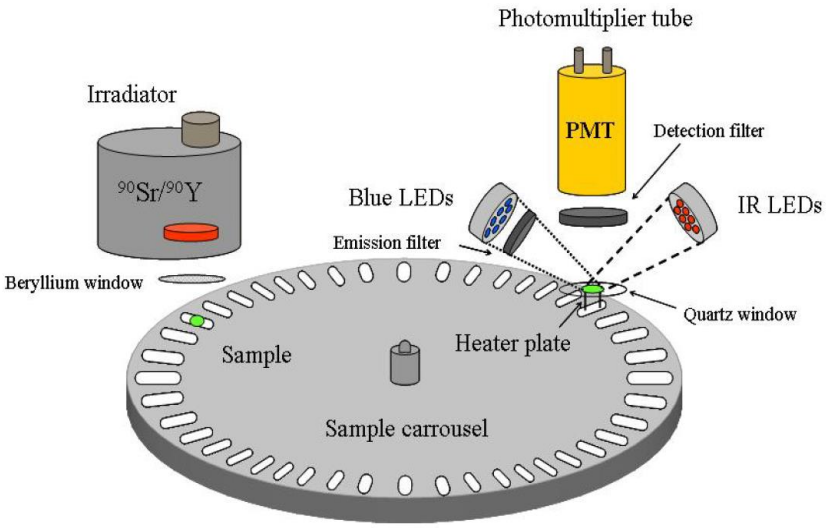

Figure 2.15: A schematic representation of TL reader sowing basic components [72].

In thermoluminescence experiment, the samples are irradiated with either of the above-mentioned excitation sources. This is a means of exciting the sample and fill the available traps in the sample with charge carriers. Heating the sample usually from room temperature to 500 ^{o}C after irradiation then triggers the emission of photons when the electrons relax back to lower energy states. These emitted photons are then detected by the PMT. The intensity of these emitted photons versus temperature is recorded as a thermoluminescence spectrum, referred to as a thermoluminescence glow curve [73]. Each peak on the spectrum is a representative of a charge carrier trap with a distinct trap depth. The higher the intensity of the peaks shows that a particular type of a trap is at a high concentration in the sample [73].

REFERENCES

1. Claudia Altavilla, Enrico Ciliberto, Inorganic Nanoparticles: Synthesis, Applications, and Perspectives, CRC Press, 2017.
2. Guozhong Cao, Ying Wang, Nanostructures and Nanomaterials: Synthesis, Properties, and Applications, World Scientific, 2011.
3. Rajendra Kumar Goyal, Nanomaterials and Nanocomposites: Synthesis, Properties, Characterization Techniques, and Applications, CRC Press, 2017.
4. J. W. Mullin, Crystallization: 4th edn, Butterworth-Heinemann, Oxford, Boston, 2001.
5. https://www.slideshare.net/SachinHariprasad/solidification-of-metals-by-hari-prasad/2019/05/28.
6. Keshra Sangwal, Additives and Crystallization Processes: From Fundamentals to Applications, ohn Wiley & Sons, 2007, England.
7. https://www.benbest.com/cryonics/lessons.html.
8. Ignác Capek, Noble Metal Nanoparticles: Preparation, Composite Nanostructures, Biodecoration and Collective Properties, Springer, Japan, 2017.
9. Zhaohui Wu, Shuanglei Yang and Wei Wu, Shape control of inorganic nanoparticles from solution, Nanoscale, 8 (2016) 1237.
10. https://www.google.co.za/search?q=Free+energy+as+a+function+of+nucleus+size+during+homogeneous+nucleation/schematic&tbm=isch&source=univ&sa=X&ved=2ahUKEwif09K5lYniAhVPyhoKHW3cB4MQsAR6BAgJEAE&biw=1536&bih=754#imgrc=Sebv5_0xR20dXM:
11. Jiujun Zhang, Hansan Liu, Electrocatalysis of Direct Methanol Fuel Cells: From Fundamentals to Applications, Wiley-VCH Verlag GmbH & Co. KGaA, Weinheim, 2009.
12. Efstratios N. Pistikopoulos, Michael C. Georgiodis, and Julio R. Banga, Process System Engineering: Dynamic Process Modelling, Volume 7, WILEY-VCH Verlag GmbH & Co., 2011.

13. Shahrzad Arshadi, Javad Moghaddam, and Mohammadreza Eskandarian, LaMer diagram approach to study the nucleation and growth of Cu2O nanoparticles using supersaturation theory, Korean J. Chem. Eng., 31(11) (2014) 2020-2026.
14. J. Chang, and E. R. Waclawik, Colloidal semiconductor nanocrystals: controlled synthesis and surface chemistry in organic media, The Royal Society of Chemistry, 4 (2014) 23505-23527.
15. Dunne P.W, Munn A.S, Starkey C.L, Huddle T.A, Lester E.H. 2015 Continuous-flow hydrothermal synthesis for the production of inorganic nanomaterials. Phil. Trans. R. Soc. A 373: 20150015.
16. R. Zong, X. Wang, S. Shi and Y. Zhu, kinetically controlled seed-mediated growth of narrow dispersed silver nanoparticles up to 120 nm: secondary nucleation, size focusing, and Ostwald ripening, Phys. Chem. Chem. Phys. 16 (2014) 4236-4241.
17. Chien-Hsin Ho, Chih-Pin Tsai, Chia-Chi Chung, Chun-Ying Tsai, Fu-Rong Chen, Hong-Ji Lin, and Chih-Huang Lai, Shape-Controlled Growth and Shape-Dependent Cation Site Occupancy of Monodisperse Fe_3O_4 Nanoparticles, Chem. Mater. 23 (2011) 1753–1760.
18. W. Tan, Y. Yu, M. Wang, F. Liu, and L. K. Koopal, Shape Evolution Synthesis of Monodisperse Spherical, Ellipsoidal, and Elongated Hematite (α-Fe2O3) Nanoparticles Using Ascorbic Acid, Cryst. Growth Des. 14 (2014) 157−164.
19. T. Sugimoto, X. P. Zhou and A. Muramatsu, Synthesis of uniform anatase TiO2 nanoparticles by gel-sol method 3. Formation process and size control, J. Colloid Interface Sci. 259 (2003) 43–52.
20. M. K. Alqadi, O. A. A. Noqtah, F. Y. Alzoubi, J. Alzouby and K. Aljarrah, pH effect on the aggregation of silver nanoparticles synthesized by chemical reduction, Mater. Sci. 32(1) (2014) 107–111.
21. T. Wang, S. Xu, N. Hu, J. Hua, Da Huang, W. Jiang, S. Wang, S. Wu, Y. Zhang, Z. Yang, Microwave preparation and remarkable ethanol sensing properties of ZnO particles with controlled morphologies in water-

ethylene glycol binary solvent system, Sens. Actuator B-Chem. 255 (2018) 1006–1014.

22. Neus G. Bastus, Joan Comenge, and Víctor Puntes, Kinetically Controlled Seeded Growth Synthesis of Citrate-Stabilized Gold Nanoparticles of up to 200 nm: Size Focusing versus Ostwald Ripening, | Langmuir 2011, 27, 11098–11105.
23. Nagaprasad Puvvada, Pravas Kumar Panigrahi, Himani Kalita, Keka R. Chakraborty, Amita Pathak, Effect of temperature on morphology of triethanolamine-assisted synthesized hydroxyapatite nanoparticles, Appl Nanosci. (2013) 3:203–209.
24. Wei-Hong Zhong: Nanoscience and Nanomaterials: Synthesis, Manufacturing and Industry Impacts, DEStech Publications, 2012.
25. http://shodhganga.inflibnet.ac.in/bitstream/10603/707/11/11_chapter%202.pdf./06/05/2019.
26. Annelise Kopp Alves, Carlos P. Bergmann, Felipe Amorim Berutti, Novel Synthesis and Characterization of Nanostructured Materials, Springer Science & Business Media, 2013.
27. Proceedings of The Sixth International Conference on Luminescent Materials, Electrochemical Society,1998.
28. W. M. Yen, M. J. Weber, Inorganic Phosphors: Compositions, Preparation and Optical Properties, CRC Press, 2004.
29. K. N. Shinde, S. J. Dhoble, H. C. Swart, K. Park, Phosphate Phosphors For Solid-State Lighting, Springer, Berlin Heidelberg, 2012.
30. Willams T. Barbosa,Imarally V. S. R. Nascimento,Raúl Garcia-Carrodeguas,Marcus V. L. Fook,Miguel A. Rodríguez, Combustion synthesis and characterization of Sr3Al2O6, Int J Appl Ceram Technol. (2019) 595–601.
31. A. Lakshmanan, Luminescence and Display Phosphors: Phenomena and Applications, Nova Publishers, 2008.
32. K. Byrappa, Masahiro Yoshimura, Handbook of Hydrothermal Technology, second edition, William Andrew, Oxford, UK, 2013.

33. Advanced Magnetic and Optical Materials, Ashutosh Tiwari, Parameswar K. Iyer, Vijay Kumar, Hendrik Swart, Scrivener Publishing, 2017.
34. Ruren Xu, Yan Xu, Elsevier B.V, Modern Inorganic Synthetic Chemistry: Second Edition captures, Netherlands, 2017.
35. https://www.researchgate.net/figure/Schematic-of-Teflon-lined-stainless-steel-autoclave-typically-used-in-laboratories-for_fig5_315869720/06/05/2019.
36. Philippe Knauth, Joop Schoonman, Nanostructured Materials: Selected Synthesis Methods, Properties and Applications, Kluwer Academic Publishers, New York, 2004.
37. Tiwari, Ratnesh, Dubey, Vikas, Dhoble, Sanjay J, Emerging Synthesis Techniques for Luminescent Materials, IGI Global, 2018.
38. Z, Li, Industrial Applications of Electron Microscopy, CRC Press, New York, 2002.
39. https://cmrf.research.uiowa.edu/scanning-electron-microscopy/06/03/2018.
40. K. N. Shinde, S. J. Dhoble, H. C. Swart, K. Park, Phosphate Phosphors For Solid-State Lighting, Springer, Berlin Heidelberg, 2012.
41. H. Schatten, Scanning Electron Microscopy for the Life Sciences, Cambridge University Press, 2013.
42. W. Zhou, Z. L. Wang, Scanning Microscopy for Nanotechnology: Techniques and Applications, Springer, 2007.
43. E. Lifshin, X-ray Characterization of materials, John Wiley & Sons, New York, 2008.
44. https://onlinelibrary.wiley.com/doi/epdf/10.1002/andp.201200724/06/03/2018
45. J. Drenth, Principles of Protein X-ray Crystallography, Springer+Business Media, New York, 1999.
46. R. A. Fava, Crystal Structure and Morphology, New York, Academic Press, 1980.

47. http://epswww.unm.edu/media/pdf/SmartLab-Operating-Procedures.pdf/06/03/2018.
48. Siegfried Hofmann, Auger- and X-Ray Photoelectron Spectroscopy in Materials Science: A User-Oriented Guide, Springer Science & Business Media, 2012
49. http://wikivisually.com/wiki/Laser-based_angle-resolved_photoemission_spectroscopy/12/05/2017
50. Paulo Davim, Surface Integrity in Machining, Springer Science & Business Media, (2010).
51. http://www.chm.bris.ac.uk/pt/diamond/jamespthesis/chapter2.htm/04/10/22.
52. [Klaus Wandelt, Surface and Interface Science, Volumes 1 and 2, John Wiley & Sons, (2012).
53. Brian C. Smith, Fundamentals of Fourier Transform Infrared Spectroscopy, CRC Press, 2011.
54. Nishikida, Selected Applications of Modern FT-IR Techniques, Routledge, 2019.
55. Vamsi KrishnaUndavalli, ChenxingLing, Bhupendra Khandelwal, Chapter 6 - Impact of alternative fuels and properties on elastomer compatibility, 2021, 113-132.
56. Da-Wen Sun, Infrared Spectroscopy for Food Quality Analysis and Control, Academic Press, 2009.
57. https://jascoinc.com/learning-center/theory/spectroscopy/fundamentals-ftir-spectroscopy/04/10/22
58. https://www.findlight.net/blog/2019/03/27/ftir-principles-applications/04/10/22
59. Vamsi KrishnaUndavalli, ChenxingLing, BhupendraKhandelwal, Chapter 6 - Impact of alternative fuels and properties on elastomer compatibility, 2021, 113-132.
60. Gang Chen, Nanoscale Energy Transport and Conversion: A Parallel Treatment of Electrons, Oxford University Press, 2005.

61. RPL Dosimetry, Radiophotoluminescence in Health Physics, J. A. Perry, CRC Press, 1987.
62. https://www.rose-hulman.edu/~brandt/FL3.PDF/2016/07/20.
63. John C. Lindon, Geoge E. Tranter, David W. Koppenaal, Encyclopedia of Spectroscopy and Spectrometry, Academic Press, UK, 2016.
64. http://www.mrfn.org/sites/www.mrfn.org/files/instrument/FLMax4_Instrument_Manual_0.pdf/2016/07/20.
65. Rong-Jun Xie, Yuan Qiang Li, Naoto Hirosaki, Hajime Yamamoto, Nitride Phosphors and Solid-State Lighting, CRC Press, 2016.
66. Aaron R. Johnson, Shu-Jen Lee, Julien Klein, and Jerzy Kanicki, Review of Scientific Instruments 78, 096101 (2007).
67. http://www.horiba.com/fileadmin/uploads/Scientific/Documents/Fluorescence/quantumyieldstrad.pdf/15/05/2017.
68. Ute Resch-Genger, Standardization and Quality Assurance in Fluorescence Measurements I: Techniques, Springer Science & Business Media, 2008.
69. Lars-Olof Palsson, Andrew P. Monkman, Measurements of Solid-State Photoluminescence Quantum Yields of Films Using a Fluorimeter, Adv. Mater. 14 (2002) 757-758.
70. http://mrfn.org/sites/mrfn.org/files/instrument/Quanta-phi_Integrating_Sphere_Manual_0.pdf/15/05/2017.
71. Aaron R. Johnson, Shu-Jen Lee, Julien Klein, and Jerzy Kanicki, Review of Scientific Instruments 78, 096101 (2007); doi: 10.1063/1.2778614.
72. http://www.usu.edu/geo/luminlab/Reader.pdf/15/05/2017.
73. M. V. dos S Rezende,R. M. Araujo, M. E. G. Valerio, R. A. Jackson, Intrinsic Defects in Strontium Aluminates studied via Computer Simulation Technique, J. phys. 249 (2010) 012042.

CHAPTER 3

Structure, Morphology, and defects of $SrSiO_3/SiO_2$ phosphor

3.1. INTRODUCTION

Alkaline earth silicates have been studied and reported as promising hosts for phosphor materials, and this is mainly due to their chemical, physical and thermal stability [1,2]. A considerable amount of research has also been conducted on their structure, morphology and size (micro and nano-particles). Such research was mainly to understand how the modulation of these structures, morphologies, and sizes affect their physical properties, luminescence properties in particular [3,4,5]. Modulation and optimization of structure, size and morphology of these phosphor materials usually results in excellent luminescence properties which are applicable in solid state lighting, i.e. phosphor-converted light emitting diodes (pc LEDs) [6,7]. One common way of modulating and optimizing structure, size and morphology of phosphor materials and hence luminescence efficiency of phosphors is through synthesis process. For instance, synthesis methods which use high temperatures (800-1600 ^oC) such as solid-state reaction method usually result in irregular morphology and large grain sizes, and this is usually undesirable from application point of view [7,8,9]. In this chapter $SrSiO_3/SiO_2$ phosphors of different Sr/Si molar ratio (1:1, 1:2, 2:1, 2.5:1, and 3.5:1) were synthesized using co-precipitation method and an extra sample of 2:1 molar ratio was also synthesized by hydrothermal method for comparison with the sample of the same molar ratio which was prepared by co-precipitation method. The comparison is done only on the 2:1 molar ratio as it will be noted in the subsequent chapters that this sample shows excellent white phosphorescence, which is the core of this study, compared to the rest of the samples. Structure, morphology, and sizes of these different phosphors are studied in this chapter.

3.2. EXPERIMENTAL

3.2.1. Sample preparation using co-precipitation method

The nano-crystalline, $SrSiO_3/SiO_2$ phosphors were synthesized using co-precipitation and hydrothermal methods. In a typical co-precipitation method, 0.331, 0.661, 1.5, 1.653 and 2.315 g of strontium carbonate ($SrCO_3$) in analytical grade were separately dissolved into 100 mL of deionised water, with a few drops of nitric acid (HNO_3) added to convert $SrCO_3$ into $(SrNO_3)_2$ and stirred at room temperature for 1 hour. After an hour, a second solution of 1 mL of tetraethyl orthosilicate (TEOS) in 10 mL of ethanol, with a few drops of nitric acid which was also separately stirred for 30 minutes, was poured into the first solution, and allowed to stir for 30 minutes.

This mixture was then heated at 90 ^oC, while stirring for an hour, after which it was allowed to cool to room temperature to be precipitated while pH was being adjusted to 9 using NaOH solution at a 1:1 molar ratio with $SrCO_3$. The resulting white precipitates were then washed 3 times with ethanol and deionised water separately, after which they were filtered and dried at 100 ^oC overnight. The dried products were then ground in an agate mortar to fine final powder products and annealed in air at 1050 ^oC, after which XRD measurements were performed for structure confirmation.

3.2.2. Sample preparation using hydrothermal method

Similarly, in hydrothermal method, 1.5 g of strontium carbonate ($SrCO_3$) in analytical grade was separately dissolved into a 100 mL of deionised water, with a few drops of nitric acid added to convert $SrCO_3$ into $(SrNO_3)_2$ and stirred at room temperature for 1 hour. After an hour, a second solution of 1 mL of tetraethyl orthosilicate (TEOS) in 10 mL of ethanol, with a few drops of nitric acid (HNO_3) which was also separately stirred for 30 minutes, was poured into the

first solution, and allowed to stir for 30 minutes. Instead of heating, this solution was pH-adjusted to 9 using NaOH solution at 1:1 molar ratio with $SrCO_3$.

The resulting solution was then transferred into Teflon-lined stainless-steel autoclave, sealed, and kept at 180 ^oC for 24 h, after which it was allowed to cool to room temperature naturally. The resulted white product was filtered and washed with distilled water and absolute ethanol three times separately before drying at 100 ^oC overnight. The dried product was then ground in an agate mortar to a fine final powder product and annealed in air at 1050 ^oC, after which XRD measurements were performed for structure confirmation.

3.3. RESULTS AND DISCUSSION

3.3.1. Sample structure

X-ray diffraction (XRD) measurements were carried out to investigate the crystal structure and the crystallinity of the prepared phosphors with various Sr to Si molar ratios, and X-ray diffraction pattens are shown in Figure 3.1. **Figure 3.1** (c), (d), (e), (f), and (g) are the phosphors prepared at Sr/Si molar ratio of 2:1, 1:2, 1:1, 2.5:1, and 3.5:1 by co-precipitation method, while **figure 3.1** (h) represents a X-ray difraction pattern of a 2:1 Sr/Si molar ratio phosphor prepared by hydrothermal method. All main diffraction peaks match well with typical XRD patterns of the Hexagonal phase of $SrSiO_3$ according to the ICSD data file number (59308) as shown in Figure 3.1 (b), except for the two diffraction peaks at 21.98 and 33.77 degrees, marked with an asterik (∗) which did not match with the $SrSiO_3$ phase, but matched well with the SiO_2 hexagonal phase acording to the ICSD data file number (170554) as shown in **Figure 3.1** (a) in the form of $SrSiO_3$/ SiO_2 phosphor material. This suggests that the prepared phosphors both with co-precipitation and hydrothermal methods are of a mixed phase in the form of $SrSiO_3$/ SiO_2 phosphor material.

Scherrer's formular in equation 3.1 was used to estimate the average crystallite sizes of the prepared phosphors [10], from the full width at half maximum (FWHM) of the diffraction peaks located at 2θ = 21.84°, 30.61°, and 48.86° and the average values as shown from table 3.1 were taken from the three values for each sample.

Table 3. 1: *The average crystallite sizes of the prepared phosphors using both co-precipitation and hydrothermal methods.*

Sample	Crystallite size (nm)
2:1 Sr/Si ratio Co-prec	26.591
1:2 Sr/Si ratio	33.177
1:1 Sr/Si ratio	24.510
2.5:1 Sr/Si ratio	29.155
3.5:1 Sr/Si ratio	27.848
2:1 Sr/Si ratio hydro	23.584

$$D = \frac{k\lambda}{\beta \cos\theta} \qquad (3.1)$$

D represents the crystallite size, β the full width at half maximum height of the diffraction peak, λ denotes the X-ray wavelength, θ is the Bragg's angle, k is a constant (0.94). The crystallite sizes were averaged and proven that the prepared phosphors are indeed nanomaterials. There was a random change in the crystallite size as a result of a change in Sr/Si molar ratio in the phosphors prepared by the same method (co-precipitation), therefore the observed change

cannot be associated with the change in Sr/Si molar ratio. Also, a 2:1 molar ratio phosphor prepared by co-precipitation method showed bigger crystallite sizes than the one prepared by hydrothermal method. The observed difference in crystallite sizes between these two samples is associated with the difference in preparation conditions in both methods.

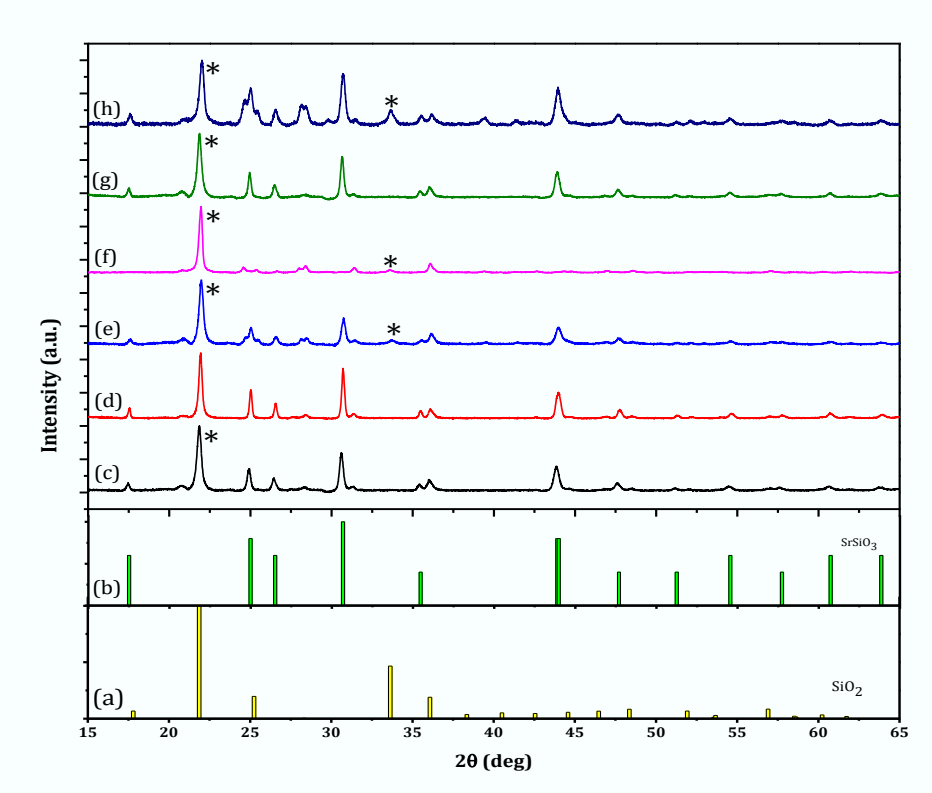

Figure 3.1: XRD standard files of SiO_2 (a) and $SrSiO_3$ (b), together with XRD parttens of $SrSiO_3$/ SiO_2 phosphors prepared by co-precipitation method at Sr/Si molar ratio of 2:1 (c), 1:2 (d), 1:1 (e), 2.5:1 (f), and 3.5: 1 (g). (h) represents an XRD partten of $SrSiO_3$/ SiO_2 phosphors prepared by hydrothermal method at 2:1 molar ratio.

3.3.2. Fourier transform infrared spectroscopy

As a complementary technique to XRD for structural confirmation, the Fourier transform infrared spectroscopy was used to determine the presence of different functional groups in the prepared $SrSiO_3/SiO_2$ phosphors by co-precipitation and hydrothermal methods. The spectra of $SrSiO_3/SiO_2$ phosphors with 1:2 and 1:1

molar ratio prepared by co-precipitation method are presented in **figure 3.2** (a) and (b) respectively. In both **figure 3.2** (a) and (b), the broad bands in the 3600-2520 cm^{-1} region, are associated with stretching vibrations of hydroxyl (OH) groups of water which may have been absorbed on the surface of the samples [11,12,13,14]. There is also evidence of this H-O-H bending vibration due to water hydration within the 1600-1650 cm^{-1} range peaking at 1619 cm^{-1} in both samples [15,16]. A very intense peak evident at 1074 cm^{-1} in **figure 3.2** (a) and (b) is characteristic of the asymmetric stretching vibration of Si-O-Si bonds in the two samples [17,18]. The Si-O stretching vibrational bands in the range 800-970 cm^{-1} can also be observed in both **figure 3.2** (a) and (b). The Sr-O-Sr stretching and Sr-O bending vibrations are also evident at 852 and 621 cm^{-1} respectively in both samples [19,20]. Evident also at 531 cm^{-1} in both samples is the Si-O-Si bending vibration. The Si-H band is also evident at 2282 cm^{-1} in both samples [21].

The peaks at 790, 924, and 986 cm^{-1} are the evidence of the Si–O–Si and O–Si–O stretching vibrations [22]. A peak at 706 cm^{-1} is assigned to the Si-O in the octahedra of silicate species [23]. In the range 1900-1700 cm^{-1}, the bands peaking at 1878 and 1751 cm^{-1} which are ascribed to the asymmetric streching of the carbonate (CO_3^{2-}) groups can also be observed in both samples [24]. A weak band at 1428 cm^{-1} in both samples is also ascribed to the assymmetric stretching of (CO_3^{2-}) groups of $SrCO_3$ [24,25]. A characteristic peak of C=C stretching bond at 1982 cm^{-1} can also be ovserved in both samples [26,27].

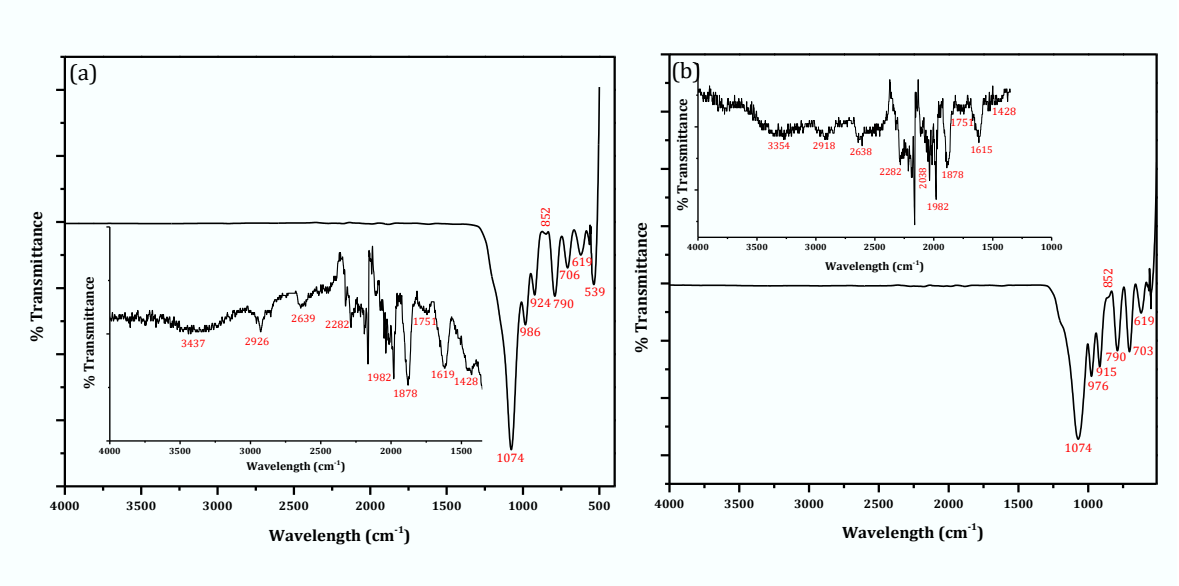

Figure 3.2: FTIR Spectra of phosphors prepared at 1:2 (a) and 1:1 (b) Sr/Si molar ratio by co-precipitation. The inserts in both (a) and (b) are plots to show peaks in the regions where weaker peaks were suppressed by the intense one at 1074 cm^{-1}.

Figure 3.3. (a) and (b) presents FTIR spectra of 2:1 Sr/Si molar ratio samples prepared by co-precipitation and hydrothermal methods respectively. A Similar comparison as in **figure 3.2** was done here. In both **figure 3.3** (a) and (b), the broad bands in the 3600-2520 cm^{-1} region, are associated with stretching vibrations of hydroxyl (OH) groups of water which may have been absorbed on the surface of the samples [11,12,13 ,14]. There is also evidence of this H-O-H bending vibration due to water hydration in the 1600-1650 cm^{-1} range peaking at 1619 and 1630 cm^{-1} in **figure 3.3** (a) and (b) respectively [13,16].

An intense peak evident at 1075 cm^{-1} in figure 3.3 (a) is attributed to the asymmetric stretching vibration of Si-O-Si bond [17,18]. This peak appears to be shifted to lower values (1065 cm^{-1}) in the sample prepared by hydrothermal method, which could be associated with a difference in the Si-O-Si bond length between the two samples [28]. The Sr-OH stretching and Sr-O bending vibrations are also evident at 850 and 621 cm^{-1} respectively in the sample prepared by co-precipitation method in **figure 3.3** (a) [19,20,23]. The Sr-OH stretching band which

interesttingly is associated with the octahedral sites in the silicate matrix, is observed to have shifted to lower wavenumbers (800 cm^{-1}) whereas the 621 cm^{-1} bending vibration seemed to have disappeared in the sample prepared by hydrothermal method in **figure 3.3** (b). A closer look at the Sr-OH stretching band shows that this band is intense in the sample prepared by hydrothermal method, which is clear indication that the number of non-bridging oxygens (NBO's) is higher in this sample as the water is also ocuppying the network modifying site [28,29]. It was suggested in the litterature that the neighbouring Si-O-Si in a silicate matrix are sensitive to and weakened by the presence of the NBO's, hence a lower intensity of the 107 cm^{-1} band in **Figure 3.3** (b) than in (a). Symmetric and asymmetric CH_3 bands can also be observed in the sample prepared by hydrothermal method at around 1370 and 1439 cm^{-1} in **figure 3.4** (a) and (b).

In other words, the formation of hydrogen bonds was only favourable in the hydrothermal sample than all the co-precipitation ones. The results of the formation of these bonds is an increase in the Si-O bond length which has a consequence of a decreased vibration, hence a shift to lower wavenumbers in the 2:1 molar ratio sample prepared by hydrothermal method compared to the 2:1 molar ration prepared by co-precipitation [28,29]. Also, very interesting in **figure 3.4** (a) and (b) is the disappearence of the octahedral 706 cm^{-1} peak in the 2:1 molar ratio sample prepared by hydrothermal method. This peak is sufficiently intense in the 2:1 molar ratio sample prepared by co-precipitation method, and very weak in all other samples prepared by co-precipitation.

From a structural point of view, this is an indication that, the lattice sites were being tempered with in two ways, namely through sample preperation, and though modulation of strontium content in these samples. Evident also at 531 cm^{-1} in **figure 3.3** (a) is the Si-O-Si bending vibration. This peak was red-shifted to 546 cm^{-1} in the sample prepared by hydrothermal method. The Si-H band is also evident at 2282 cm^{-1} in **figure 3.3** (a) [21,28].

There is no evidence of this peak in the sample prepared by hydrothermal method. In the range 1900-1700 cm^{-1}, absorption bands peaking at 1882 and 1756 cm^{-1} which are ascribed to the asymmetric streching of carbonate (CO_3^{2-}) groups can also be observed in **figure 3.3** (a) [24]. In **figure 3.3** (b), these asymmetric streching of carbonate (CO_3^{2-}) groups are evident at 1870 and 1794 cm^{-1}. Weak bands at 1617 cm^{-1} in **figure 3.3** (a) and 1444, and 1372 cm^{-1} in **figure 3.3** (b) are also ascribed to the assymmetric stritching of (CO_3^{2-}) groups of $SrCO_3$ [24,25]. Characteristic peaks of C=C stretching bond at 1991 cm^{-1} in **figure 3.3** (a) and 1977 cm^{-1} in **figure 3.3** (b) can also be observed [26]. It is interesting to note in **figure 3.3** (a) and (b) that several peaks associated with silicon-oxygen defects that are present in the sample prepared by co-precipitation method are absent in the one prepared by hydrothermal method.

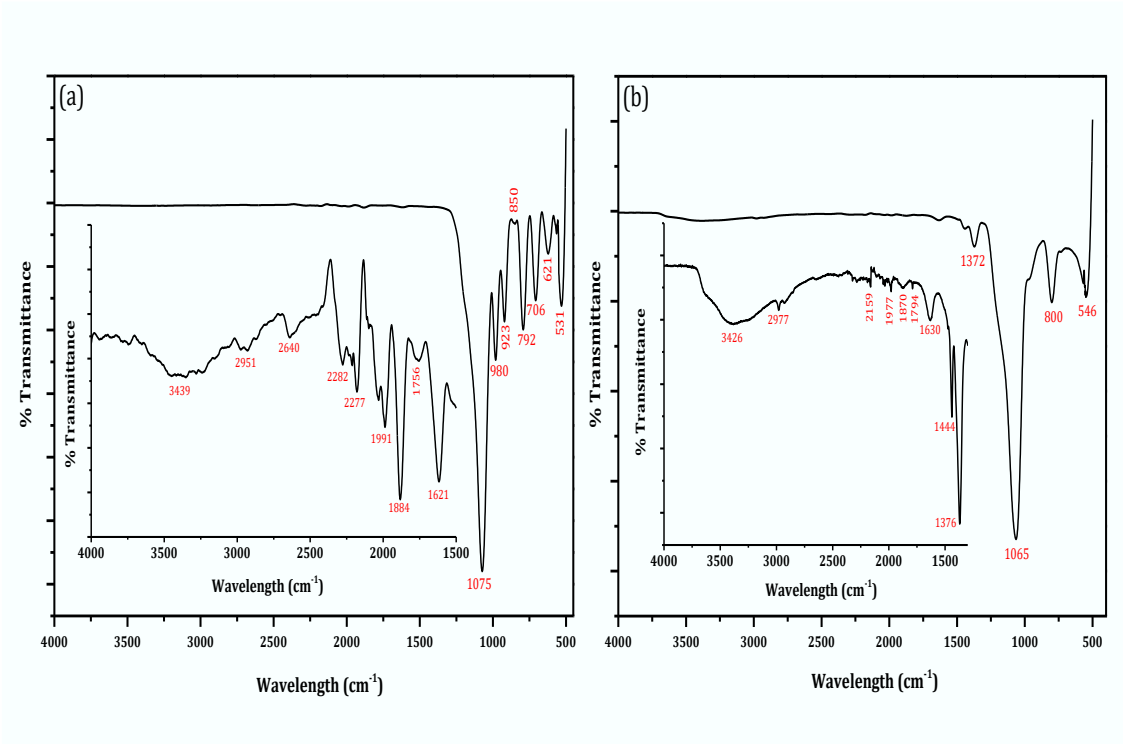

Figure 3.3: FTIR Spectra of phosphor prepared at 2:1 Sr/Si molar ratio by co-precipitation (a) and hydrothermal method(b). The inserts in both (a) and (b) are plots to show peaks in the regions where weaker peaks were suppressed by the intense on.

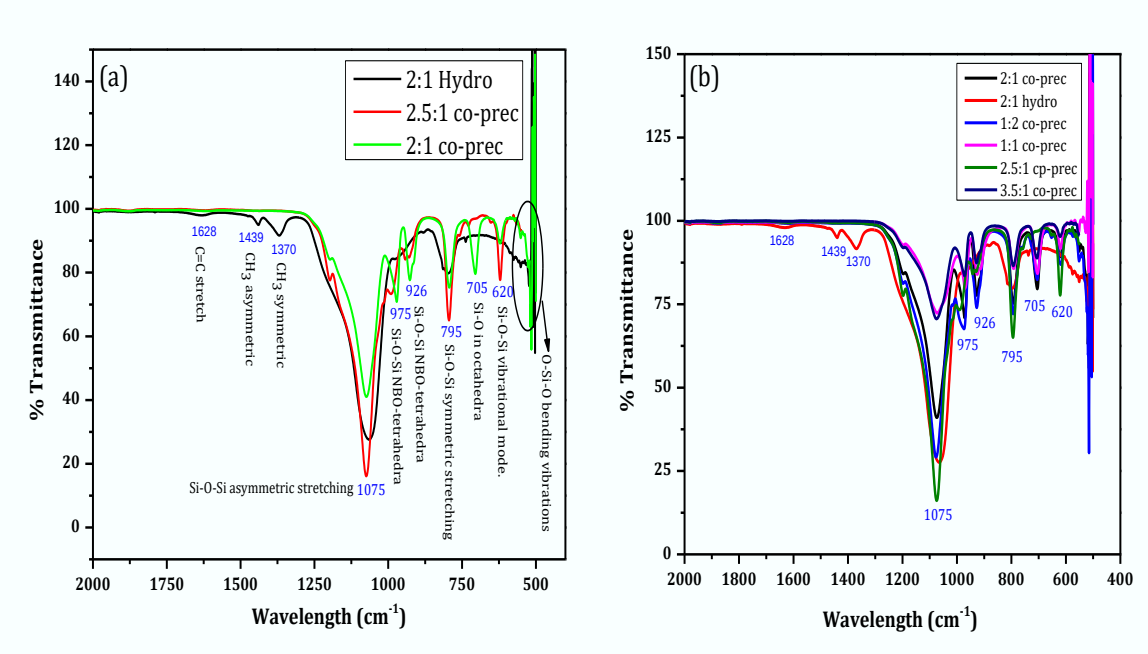

Figure 3.4: Plot of FTIR Spectra in the range 500 – 2000 cm^{-1} of phosphors prepared by co-precipitation method at 2:1 and 2.5:1 Sr/Si molar ratio and phosphor prepared at 2:1 molar ratio by hydrothermal method (a). (b) is a plot of FTIR Spectra of all samples in the range 500 – 2000 cm^{-1}. The two plots are solely to make explicit the absense of the 705 cm^{-1} peak in the hydrothermal sample.

Figure 3.5 (a) and (b) presents FTIR spectra of the phosphors prepared by co-precipitation method at 2.5:1 and 3.5:1 Sr/Si molar ratio respectively. In both **figure 3.5** (a) and (b), broad bands in the 3600-2520 cm^{-1} region, are associated with stretching vibrations of hydroxyl (OH) groups of water [11,12 ,13 ,14]. There is also evidence of this H-O-H bending vibrations due to water hydration in the 1600-1650 cm^{-1} range peaking at 1623 cm^{-1} in both **figure 3.5** (a) and (b) [13,16] An intense peak evident at 1074 cm^{-1} in both **figure 3.5** (a) and (b) is assigned to the asymmetric stretching vibration of Si-O-Si bond [17,18]. The Sr-OH stretching and Sr-O bending vibrations are also evident at 852 and 621 cm^{-1} respectively in both samples prepared in **figure 3.4** (a) and (b) [19,20,23]. It is interesting to observe in **figure 3.5**, that the octahedral 706 cm^{-1} band is weak in the 2.5:1 molar ratio sample in **figure 3.5** (a) and pronounced in the 3.5:1 molar ratio sample in **figure 3.5** (b). This can be attributed to a high strontium content in the later sample. The Si-H band is also evident at 2282 cm^{-1} in both **figure 3.5** (a) and (b)

[21]. In the 1900-1700 cm^{-1} range, bands peaking at 1882 cm^{-1} which are ascribed to the asymmetric streching of carbonate (CO_3^{2-}) groups can also be observed in **figure 3.5** (a) and (b) [24]. Weak bands at 1623 and 1443 cm^{-1} in **figure 3.5** (a) and (b), are also evidence of the assymmetric stretching of (CO_3^{2-}) groups of $SrCO_3$ [24,25]. Characteritic peaks of C=C stretching bond at 1994 and 1982 cm^{-1} can also be ovserved in **figure 3.5** (a) and (b) respectively [26].

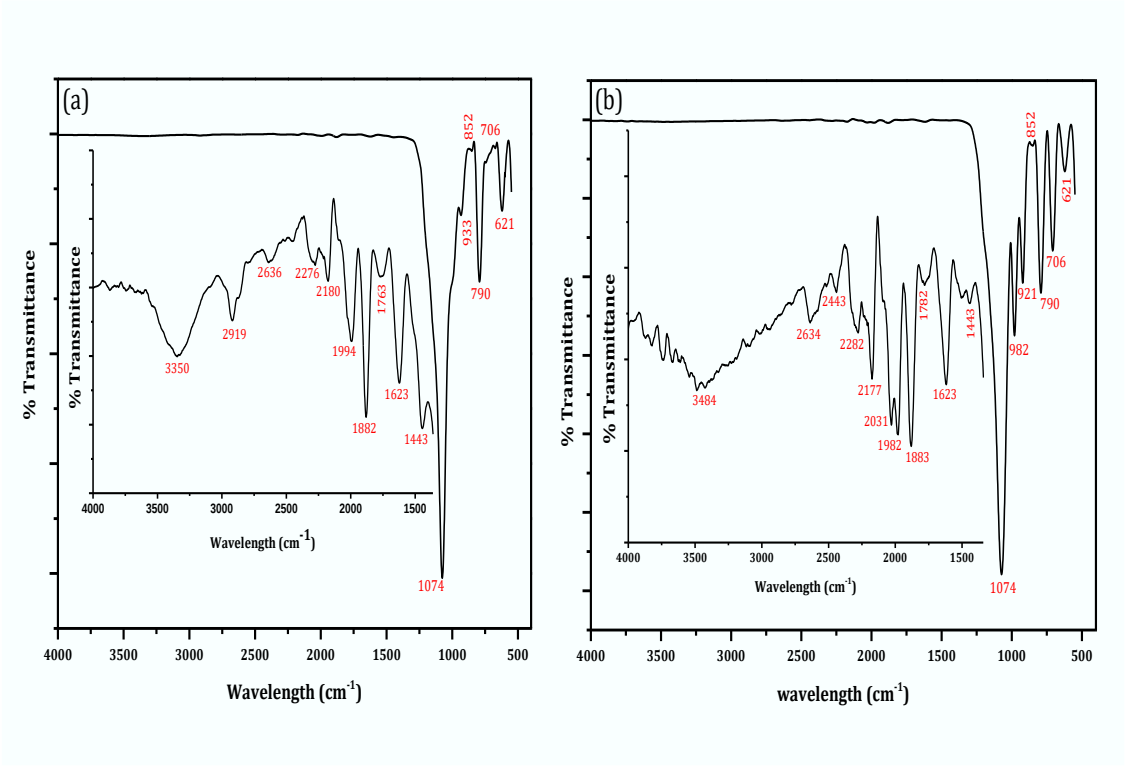

Figure 3.5: FTIR Spectra of phosphors prepared at 2.5:1 (a) and 3.5:1 (b) Sr/Si molar ratio by co-precipitation method. The inserts in both (a) and (b) are plots to show peaks in the regions where weaker peaks were suppressed by the intense one at 1074 cm^{-1}.

3.3.3. Sample morphology

3.3.3.1. Scanning electron microscope

To investigate the surface morphology of the prepared $SrSiO_3/SiO_2$ phosphors, scanning electron microscope (SEM) measurements were carried out on the

$SrSiO_3$/ SiO_2 phosphors prepared by co-precipitation method at Sr/Si molar ratio of 2:1 (a), 1:2 (b), 1:1 (c) 2.5:1 (d) 3.5:1 (e) and hydrothermal method at 2:1 Sr/Si molar ratio (f). The micrographs were acquired at X 80 magnification as presented in **Figure 3.6**. All samples exhibited irregular shaped particles, suggesting inhomogenity in particle size distribution.

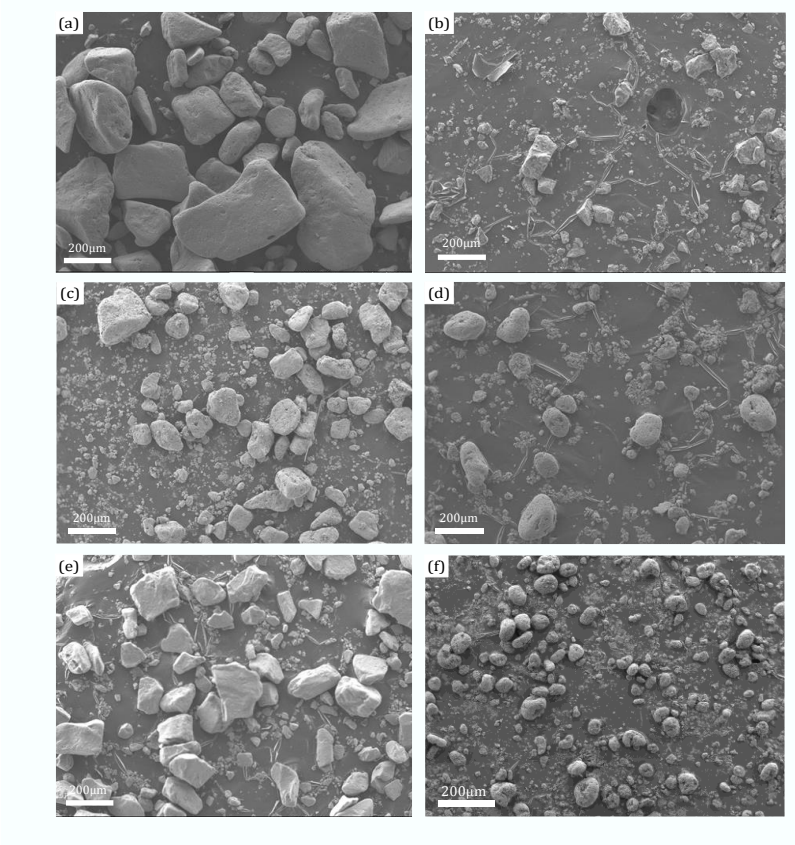

Figure 3.6: SEM low magnification (X 80) images of the $SrSiO_3$/ SiO_2 phosphors prepared by co-precipitation method at Sr/Si molar ratio of 2:1 (a), 1:2 (b), 1:1 (c) 2.5:1 (d) 3.5:1 (e) and hydrothermal method at 2:1 molar ratio (f).

Figure 3.7 presents a higher magnification for all samples in **Figure 3.6**. All samples in **figure 3.7** showed irregular spherical nanoparticles with agglomeration, with the 1:2 (more silicon) Sr/Si molar ratio sample showing more agglomeration than all other samples, while the 2:1 molar ratio sample prepared by hydrothermal

showing less agglomeration. This means that the distribution of the particle sizes in these phosphors is not homogeneous. The agglomeration in these samples can be attributed to annealing of the prepared samples at 1050 ^{o}C [27].

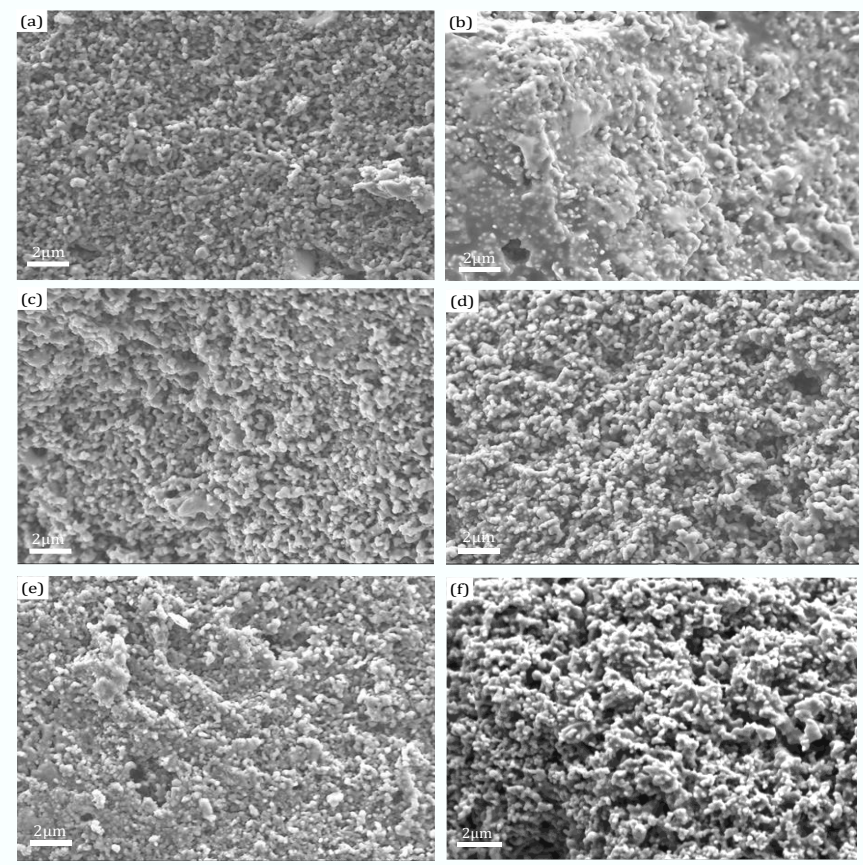

Figure 3.7: SEM high magnification (X 5000) images of the $SrSiO_3/SiO_2$ phosphors prepared by co-precipitation method at Sr/Si molar ratio of 2:1 (a), 1:2 (b), 1:1 (c) 2.5:1 (d) 3.5:1 (e) and by hydrothermal method 2:1 (f).

3.3.3.2. Energy-dispersive X-ray spectroscopy.

The elemental analysis of surfaces of the $SrSiO_3$/ SiO_2 phosphors were performed and the acquired spectrum is shown in **Figure 3.8** (a). The insert is an electron image of an area that was used during spectral acquisition and the mapping to investigate their spatial distribution of all elements in the prepared samples as can be seen from the maps in **figure 3.8** (b), (c) and (d). The Energy-dispersive X-

ray spectroscopy (EDS) spectrum in **figure 3.8** (a) confirms the presence of Sr, Si, and O in the prepared phosphor, represented by the L line of strontium at 1.806 keV, K line of Si at 1.7 keV, and K line of oxygen at 0.523 keV. All samples prepared by both methods showed the same spectrum. The carbon K line at 0.282 keV is evidence of carbon from the sample preparation with carbon tape and carbon rod from coating.

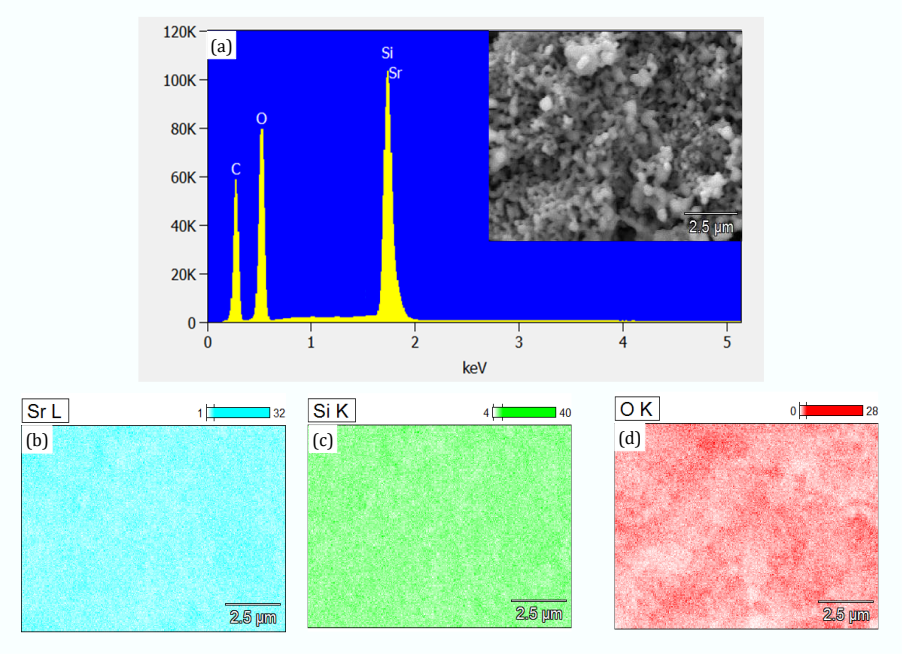

Figure 3.8: EDS spectrum of the $SrSiO_3/SiO_2$ phosphors (a), elemental distribution frames of strontium (b), silicon(c), and oxygen (d).

3.4. CONCLUSION

The prepared phosphors were proven by FTIR and XRD measurements to be of a mixed-phase nature with grain size averaged by Scherrer equation to be below 34 nm. The SEM measurements revealed spherical nono-particles with agglomeration and non-uniform distribution of particle size, with hydrothermal method sample showing less agglomeration than all the co-precipitation sample. The change in crystallite size was random relative to the change in molar ratio,

and therefore could not be associated with the change in molar ratio. The 2:1 molar ratio sample prepared by hydrothermal method was proven to have smaller crystallite sizes compared to the one prepared by co-precipitation method with same Sr/Si molar ratio. There was no obvious effect of the change in Sr/Si molar ratio on the overall crystal structures (XRD) of the prepared phosphors. There was also no effect of the Sr/Si molar ratio change on the particle shapes of the prepared phosphors by both co-precipitation and hydrothermal methods. EDS measurements demonstrated an even distribution of all the elements Sr, Si, and O in the prepared phosphors.

REFERENCES

1. Li G.H, Li M.M, Li L.L, Yong H. Zou H.F, Zou L.C, Gan S.C,and Xu, X.C.: Luminescent properties of $Sr_2Al_2SiO_7:Ce^{3+},Eu^{2+}$ phosphors for near UV-exrefd white light-emitting diodes. Mater. Lett. 65, 3418 (2011).
2. Y. Wang, Y. Chen, Q. Sun, & B. Yan, (2017). Synthesis, structure, and photoluminescence properties of Ce^{3+} and Tb^{3+} doped alkaline-earth silicate
3. Sr2MgSi2O7 phosphors for WLEDs. *Journal of Materials Research, 32*(3), 547-556.
4. Zhengwu Lua, Luqian Weng, Shenhua Song, Peixin Zhang, Xiongbiao Luo, Hydrothermal synthesis, morphology and photoluminescence of hexagonal SrSiO3:Eu2+ micro-octahedrons and prism-like hollow microstructures, Materials Chemistry and Physics 132 (2012) 800– 807.
5. Zhang, X.G., Tang, X.P., Zhang, J.L., Wang, H.H., Shi, J.X.,and Gong, M.L.: Luminescent properties of $Sr_2MgSi_2O_7:Eu^{2+}$ as blue phosphor for NUV light-emitting diodes. Powder Technol. 204, 263 (2010).
6. Baohong Li, Jie Yang, , Mingmei Wu, Two-color emitting of $Eu^{2+}$and Tb^{3+}co-doped $Sr_2MgSi_2O_7$ for UV LEDs, Optical Materials 36 (2014) 1649–1654.
7. Liping Yu, Mao Xia, Xun Chen, Chunying ong, Jinlin Zhang, Wenli Zhou, Ming Ma and Shixun Lian, Improvement of luminescence properties of $Ca_{0.8}Zn_{0.2}TiO_3:Pr^{3+}$ prepared by hydrothermal method, *Journal of Materials Research, 28*(18), 2590-2597.
8. P.T Diallo, K. Jeanlouis, P. Boutinaud, R. Mahiou, J.C. Cousseins, Improvement of the optical performances of Pr^{3+} in $CaTiO_3$, Journal of Alloys and Compounds 323–324 (2001) 218–222.
9. Eric Pinel, Philippe Boutinaud, Geneviève Bertrand, Christophe Caperaa, Joël Cellier, Rachid Mahiou, Preparation and characterization of luminescent films of Pr^{3+}-doped CaTiO3 processed by sol–gel technique, Journal of Alloys and Compounds 374 (2004) 202–206.

10. R. Sivakami, S. Dhanuskodi, R. Karvembu, Estimation of lattice strain in nanocrystalline RuO_2 by Williamson–Hall and size–strain plot methods, Spectrochim Acta A Mol Biomol Spectrosc, 152 (2016) 43–50.
11. Serdar Gültekin, Serdar Yıldırım, Ozan Yılmaz, İlker Çetin Keskin, Mehmet İsmail Katı, Erdal Çelik, Structural and optical properties of $SrAl_2O_4$: Eu^{2+}/Dy^{3+} phosphors synthesized by flame spray pyrolysis technique, Journal of Luminescence 206 (2019) 59–69.
12. A. J. Maira, J. M. Coronado, V. Augugliaro, K. L. Yeung, J. C. Conesa, and J. Soria, Fourier Transform Infrared Study of the Performance of Nanostructured TiO2 Particles for the Photocatalytic Oxidation of Gaseous Toluene, Journal of Catalysis 202, 413– 420 (2001).
13. Jung Hoon ParkK, Young Kim, Sang Do Park, Oxygen permeation and stability of $La_{0.6}Sr_{0.4}Ti_xFe_{1-x}O_{3-\delta}$(x= 0.2 and 0.3) membrane, Desalination 245 (2009) 559–569.
14. https://www2.chemistry.msu.edu/faculty/reusch/virttxtjml/spectrpy/infrared/irspec1.htm/08/01/2022.
15. Jung Hoon ParkK, Young Kim, Sang Do Park, Oxygen permeation and stability of $La_{0.6}Sr_{0.4}Ti_xFe_{1-x}O_{3-\delta}$(x= 0.2 and 0.3) membrane, Desalination 245 (2009) 559–569.
16. Irshad Ahmad, Shazia Shukrullah, Muhammad Yasin Naz, Muhammad Athar Rasheed, Mukhtar Ahmad, Ejaz Ahmed, Muhammad Shoaib Akhtar, N.R. Khalid, Abid Hussain, Sadia Khalid, Boosted hydrogen evolution activity from Sr doped ZnO/CNTs nanocomposite as visible light drivenphotocatalyst, I n t e r n a t i o n a l journal o f hydrogen energy 4 6 (2 0 2 1) 2 6 7 1 1-2 6 7 2 4.
17. Ewa Kapeluszna, Łukasz Kotwica, Agnieszka Ró_zycka, Łukasz Gołek, Incorporation of Al in C-A-S-H gels with various Ca/Si and Al/Si ratio: Microstructural and structural characteristics with DTA/TG, XRD, FTIR and TEM analysis, Construction and Building Materials 155 (2017) 643–653.
18. Mata Nayarit A, Ros-Tárraga Patricia, Velasquez Pablo, Murciano Angel, De Aza Pied N, Synthesis and characterization of 3D multilayer porous Si–Ca–P

scaffolds doped with Sr ions to modulate in vitro bioactivity, ceramic intenational 46 (2020) 968-977.

19. Mohammed M. Rahman, Mohammad Musarraf Hussain and Abdullah M. Asiri, A novel approach towards hydrazine sensor development using SrO.CNT nanocomposites, RSC Adv., 2016, 6, 65338.
20. Ishwar Prasad Sahu, Studies on the luminescence properties of dysprosium doped strontium metasilicate phosphor by solid state reaction method, J Mater Sci: Mater Electron (2016) 27:9094–9106.
21. Philip J. Launer, Updated by Barry Arkles, Infrared analysis of organosilicon compounds: spectra-structure correlations, Silicon Compounds: Silanes & Silicones, 2013 Gelest, Inc Morrisville, PA.
22. Abdolali Alemi, Shahin Khademinia, Part I: lithium metasilicate (Li_2SiO_3)—mild condition hydrothermal synthesis, characterization, and optical properties, Int Nano Lett (2015) 5:15–20.
23. V. N. Chukanov, A. D. Chervonnyi, Infrared Spectroscopy of Minerals and Related Compounds, Springer, 2016.
24. H. Patra, S.K. Rout, S.K. Pratihar, S. Bhattacharya, Effect of process parameters on combined EDTA–citrate synthesis of $Ba_{0.5}Sr_{0.5}Co_{0.8}Fe_{0.2}O_{3-\delta}$ perovskite, Powder Technology 209 (2011) 98–104.
25. S. Gunasekaran, G. Anbalagan and S. Pandi, Raman and infrared spectra of carbonates of calcite structure, J. Raman Spectrosc. 2006; 37: 892–899.
26. Wei Li, Yaohui Xu, Yang Zhou, Wenhui Ma, Shixing Wang and Yongnian Dai, Silica nanoparticles functionalized via click chemistry and ATRP for enrichment of Pb(II) ion, Nanoscale Research Letters 2012, 7:485.
27. Bhargavi ram thimmiah, Gobi nallathambi, Synthesis of α-Fe2O3 nanoparticles and analyzing the effect of annealing temperature on its properties, Materials Science-Poland, 38(1), 2020, pp. 116-121.
28. Chi-Fa Lin, Wei-Tsu Tseng, Ming Shiann Feng, Formation and characteristics of silicon nanocrystals in plasma-enhanced chemical-vapor-deposited silicon-rich oxide, Journal of Applied Physics · March 2000.

29. Joseph Davidovits, Geopolymer, Green Chemistry and Sustainable Development Solutions: Proceedings of the World Congress Geopolymer 2005.

CHAPTER 4

Effect of non-stoichiometry on white phosphorescence and Thermoluminescence properties of $SrSiO_3/SiO_2$ phosphor

4.1. INTRODUCTION

Recently, there is a multitude of research devoted to room temperature phosphorescence (RTP) due to it's applications in numerous fields, such as white light emitting diodes (WLEDs), emergency signs, bioimaging, medical diagnostics, sensors etc. [1,2]. Among the above-mentioned applications, WLEDs are particularly getting a considerable attention, due to their promising usage as lighting sources in illumination and displays and this is due to their eco-friendliness, longevity, energy saving character etc. [3]. One conventional and popular way of making WLEDs is by a combination of a yellow light emitting YAG:Ce^{3+} phosphor with a blue InGaN-based diode.

This method, however, has drawbacks of low color rendering index (CRIs < 80) and high correlated color temperature (CCTs = > 4500 k) due to insufficient red part of the spectrum [4,5]. The other explored method is through a mixture of near-UV chip together with blue, green, and red emitting phosphors [6]. This method still comes at a price of color reabsorptions among individual phosphors used, and there is a lack of homogeneity of luminescence properties in this method, which tends to suppress the luminous efficiency [6].

Besides the above-mentioned drawbacks in the previous methods, the white light is obtained from the phosphor materials which are doped with expensive rare-earths, and this makes the cost of production high, which in turn puts the price of the WLEds higher, and this is an undesirable factor which automatically triggers a search for new promising strategies to obtain WLEDs with high efficiency [7,8,9]. One interesting way of tuning physical properties of a phosphor material is to temper with it's structure and bring about non-stoichiometry by introducing

defects into the structure without doping the structure, in other words introducing lattice imperfections into the material such as substitutional defects, vacant sites, atoms on interstitial sites etc. [10,11]. N. Suriyamurthy et al reported an enhancement of the afterglow intensity of the $Sr_4Al_{14}O_{25}:Eu^{2+}$, Dy^{3+} phosphor through non-stoichiometry introduction [12]. This chapter, therefore, explores and reports white phosphorescence and thermoluminescence properties of the undoped (rare-earth free) $SrSiO_3/SiO_2$ phosphor which come from the intrinsic defects formed during the synthesis of these materials.

Undoped phosphors prepared by co-precipitation method at different Sr/Si molar ratio are prepared and their luminescence properties are compared in this chapter. So, because the 2:1 molar ratio prepared by coprecipitation method shows excellent luminescence properties, an extra 2:1 molar ratio sample was prepared by hydrothermal method to compare it's luminescence properties from the two methods. The interest in these Inorganic silicate-based phosphors is mainly due to their more chemical and thermal stability characteristics. These phosphors are also cheaper to produce compared to sulphide and aluminate-based phosphors [13], and this is because strontium and silica are in abundance and less costly [14].

4.2. EXPERIMENTAL

4.2.1. Sample preparation with co-precipitation

The phosphor materials studied in this section were prepared using the experimental procedure presented in chapter 3, section 3.2.1 and 3.2.2.

4.2.2. Characterization

The X-ray diffraction spectrometer equipped with Cu Kα (30 kV, 15 mA, λ = 1.54051Å) radiation was used at room temperature to investigate the phase and crystallinity of the $SrSiO_3/SiO_2$ phosphor. The scans during spectra acquisition were performed in the range 10° to 70°. Spectral acquisitions were carried out

using 0.05° steps and a 0.002°/s scan rate. Phosphorescence excitation and emission spectra were aquired at room temperature using a Jobin Yvon/SPEX Fluorolog®-3 spectrofluorometer, which uses a 450 W Xenon flashing lamp as photons source and collecting phosphorescence signals by a R928 PMT detector operated at 950 V in a continuous mode. These spectra were collected using a 0.2 s integration time and 4.5 nm band pass both in excitation and emission paths.

The decay curves of the phosphor were also acquired at room temperature from a Jobin Yvon/SPEX Fluorolog®-3 spectrofluorometer after exciting the phosphor samples with a Xenon flashing lamp and collecting signals by a R928 PMT detector at 950 V in a photon counting mode. During decay curve aquisitions, the samples were excited at 246 nm, where it optimally absorbs, while monitoring the emission at 495 nm. For the steady state and lifetime measurements, a double excitation monochromator (330 nm blazed, 1200 grooves/mm) with a built-in chopper and a double emission monochromator (500 nm blazed, 1200 grooves/mm) were used. TL spectra were recorded after beta irradiation using a Riso TL/OSL reader (Model DA-20), equipped with the BG39 filter as an upper filter and the blue filter as the lower filter.

4.3. **RESULTS AND DISCUSSION**

4.3.1. **Sample structure**

The XRD analysis of the prepared phosphor materials were done in chapter 3, section 3.3.1.

4.3.2. **Fourier transform infrared spectroscopy (FTIR)**

The Fourier transform infrared spectroscopy (FTIR) analysis of the prepare phosphor materials were also done in chapter 3, section 3.3.2.

4.3.3. **Photoluminescence properties of the SrSiO3/SiO2 phosphor material**

Phosphorescence studies were carried out to study the defects in the $SrSiO_3/SiO_2$ phosphors prepared at different Sr/Si molar ratios and the spectra are presented in figure 4.1. The quality of white light emitted from these phosphors is also discussed later in this section. Figure 4.1 (a), (b), (c), (d), and (e) present room temperature phosphorescence spectra of $SrSiO_3/SiO_2$ phosphors prepared by co-precipitation method at Sr/Si molar ratios of 2:1, 1:2, 1:1, 2.5:1, 3.5:1 respectively. Figure 4.1 (f) represents phosphorescence spectrum of the same phosphor prepared by hydrothermal method at 2:1 Sr/Si molar ratio and the insert in it is an excitation spectrum showing a prominent peak at 246 nm with which all the samples were excited during spectral aquisitions.

The emission spectrum in figure 4.1 (a) showed two broad peaks; a prominent one at 495 nm and another one at 687 nm making up white phosphorescence from the $SrSiO_3/SiO_2$ phosphor. Since the studied phosphors in this chapter are undoped, both of these broad peaks can only originate from intrinsic defects in the $SrSiO_3/SiO_2$ phosphors. Several undoped oxide phosphors have been reported in the literature, also attributing emissions from them to the intrinsic defects, oxygen-related defects in particular. For instance, Huang et al. reported a red emission from the undoped Y_2O_3 and they ascribed it to the oxygen related vacancy in the Y_2O_3 matrix [15].

Dhlamini et al. also attributed a 450 nm emission band of SiO_2 matrix to the oxygen vacancies [16]. It is therefore infered from here that the observed peaks originate from the Si-O defects. In particular, this phosphor could be emitting through Si-O defects from both tetrahedral and octahedral sites of the silicate matrices, since it is well known that silicate species are composed of both these

sites [17,18]. Also, the first broad emission band could be a combination of two peaks at 450 and 495nm which emit from the SiO_2 and $SrSiO_3$ matrices respectively in the $SrSiO_3/SiO_2$ composites. The peak at 495 nm is consistent with the reported oxygen related defect peak in the undoped $SrSO_4$ nanoplates by Zhai et al. [19]. Also, noticable from figure 4.1 (a) to (e) was that, the overall structure of the emission spectrum was affected by the change in Sr/Si molar ratio, in particlular, the 687 nm emission is weak in a 1:2 and 1:1 molar ratio samples prepared by co-precipitation method. This peak seems vey week and almost vanished completely at higher Sr/Si molar ratio samples (2.5:1 and 3.5:1), while the 495 nm remained.

From the FTIR analysis in figure 3.4 (a) and (b) in the previous chapter, it was noted that all samples which do not show the 687 nm peak here in figure 4.1, did also not or at a very least, showed a vey weak 706 cm^{-1} band which is associated with octahedral sites in the silicate matrices, therefore the 687 nm emission peak could be originating from the Si-O defects residing in the octahedral sites of these phosphors. Upon observation of the PL emission in figure 4.1, it is obvious that modulating the strontium content in the $SrSiO_3/SiO_2$ samples does have an effect on the overall structure of the emission spectra of these phosphors. Strontium in these phosphors acts as a network modifier [20].

In other words, introducing strontium into silicate matrices results in the breaking of bridging oxygen (BO's) bonds in the lattice. So, a higher strontium content means a higher number of bridging oxygen bonds that are broken, hence a higher number of non-bridging oxygens (NBO's) formed in the lattice [21]. Now, because luminesce in these phosphors is supported by literature to be originating from these types of defects, there should be expected a high luminescence intensity in the studied phosphors at higher NBO's up to a certain level of strontium content (2.5:1 ratio), beyond which luminescence is quenched and decreased in intensity as demonstrated in figure 4.2 (a). It was also suggested from literature that the build up of NBO's tends to interfere with and weaken the

neighbouring Si-O-Si bonds [21]. So, upon increasing the strontium content in these silicate phosphor, the NBO's build up could be interfering with the Si-O defects responsible for the 687 nm peak and eventually diminishing luminescence due to those defects [21,22].

Noted also was that, the 2:1 molar ratio sample prepared by hydrothermal method did not show the 687 nm peak, compared to the same 2:1 molar ratio sample that was prepared by co-precipitation method. The only difference between the two samples is the preparation method. So, it is suggested here that the formation of Si-O defects which are responsible for the 687 nm peak are only favourable in the co-precipitation method and not in the hydrothermal one. There are two key parameters which distinguish the two preparation methods and could be influencing the formation of defects during synthesis in this case, namely, temperature and presure.

Co-precipitation method was carried out under normal pressure at 90 ^{o}C, whereas hydrothermal method was carried out under critical temperature (> 100 ^{o}C) and pressure (> 1 bar). So obviously, the dissolution of precursors under these two different conditions in the two methods are different, therefore the stabilization of the same type of defects in the two methods shuld not be the same,

hence two different PL emission structures in the 2:1 molar ratio sample prepared by two different methods.

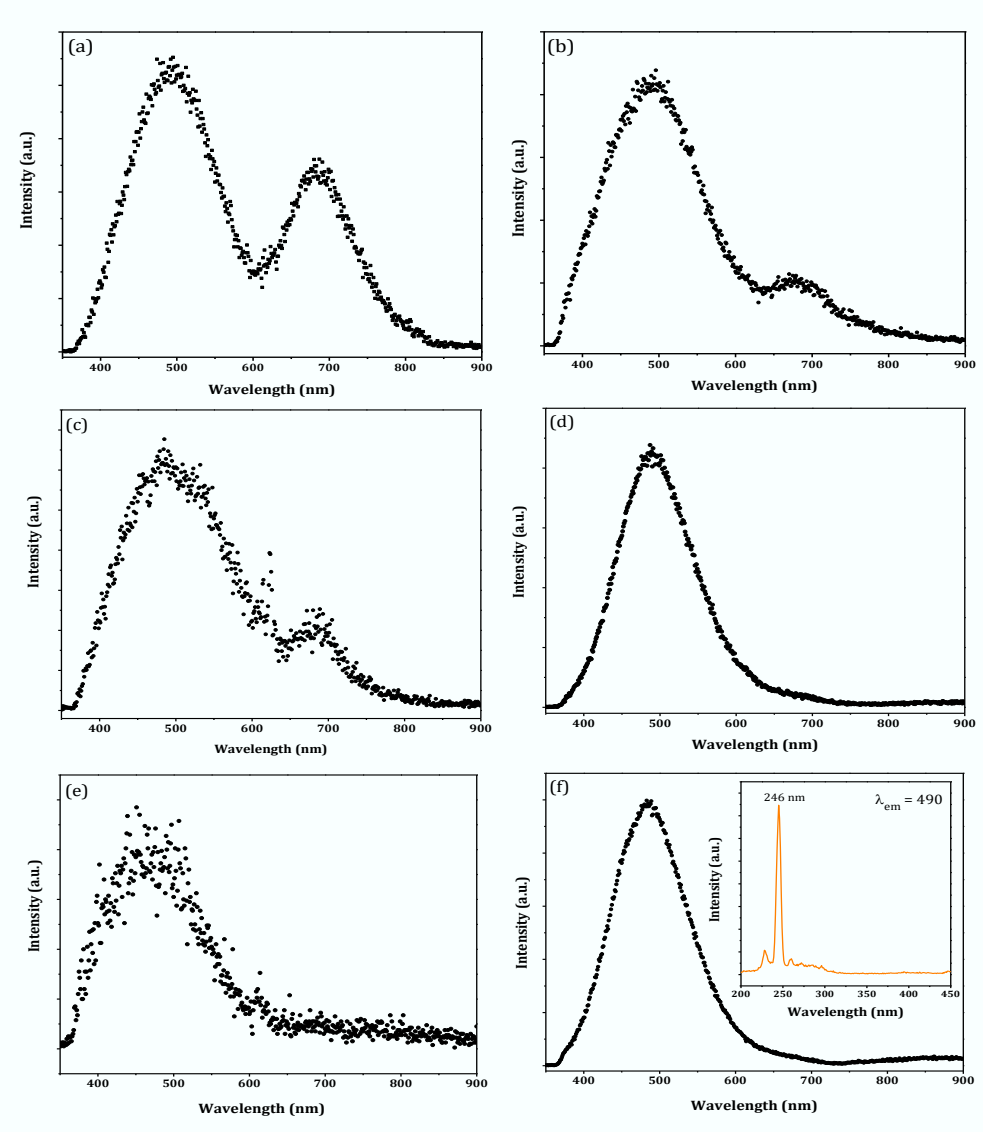

Figure 4.1: Phosphorescence spectra of the $SrSiO_3/SiO_2$ phosphors prepared by co-precipitation method at Sr/Si molar ratio of 2:1 (a), 1:2 (b), 1:1 (c) 2.5:1 (d) 3.5:1 (e) and hydrothermal method at 2:1 (f).

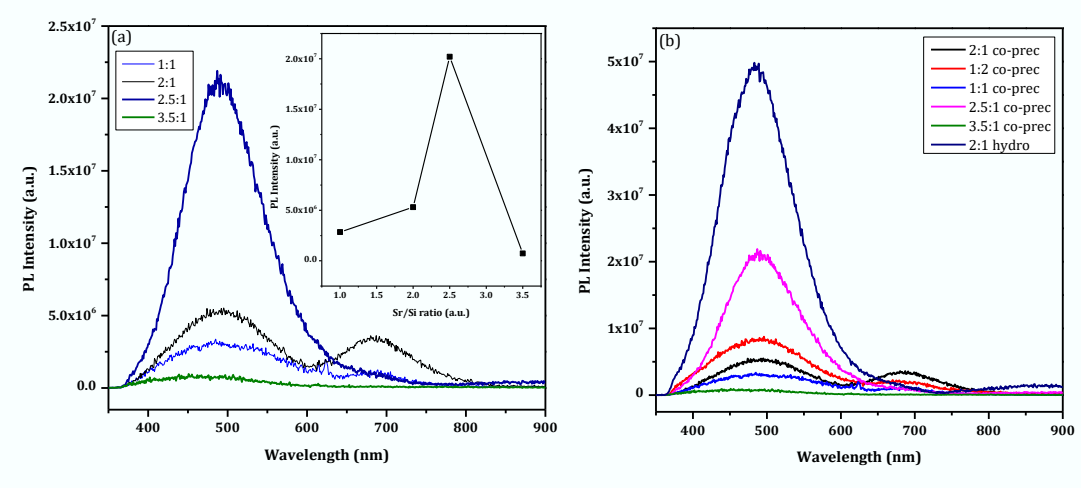

Figure 4.2: Plots of phosphorescence spectra of the $SrSiO_3/SiO_2$ phosphors demonstrating strontiium concentration quenching. (a) is a demostration of concentration quenching using only plots of samples where Sr content was increased, while (b) represents PL plots of all samples ploted on the same set of axis.

To evaluate the quality of white light emitted by the phospors discussed in this chapter, the Commission International del' Eclairage (CIE) 1931 chromaticity coordinates (x, y) of the prepared phosphors were obtained from the emission spectra after a 246 nm excitation as presented in figure 4.3. The CIE coordinates presented in figure 4.3 (a) (0.260, 0.330), (c) (0.270, 0.330), (d) (0.240, 0.320), (e) (0.210, 0.320), and (f) (0.220, 0.270), are of the $SrSiO_3/SiO_2$ phosphors prepared by co-precipitation method at Sr/Si molar ratios of 2:1, 1:1, 1:2, 2.5:1, 3.5:1 respectively, while the one in figure 4.3 (b) 0.200, 0.290 represent the CIE coordinates of the phosphor prepared by hydrothermal method at 2:1 Sr/Si molar ratio. It is evident in figure 4.3 that, for the samples prepared by co-precipitation method, the color coordinates shifted away from the neutral white light towards a green color as the strontium content was increased. The color coordinates of the 1:1 and 2:1 molar ratio samples were found to fall in the neutral white light region in the CIE diagram in figure 4.3.

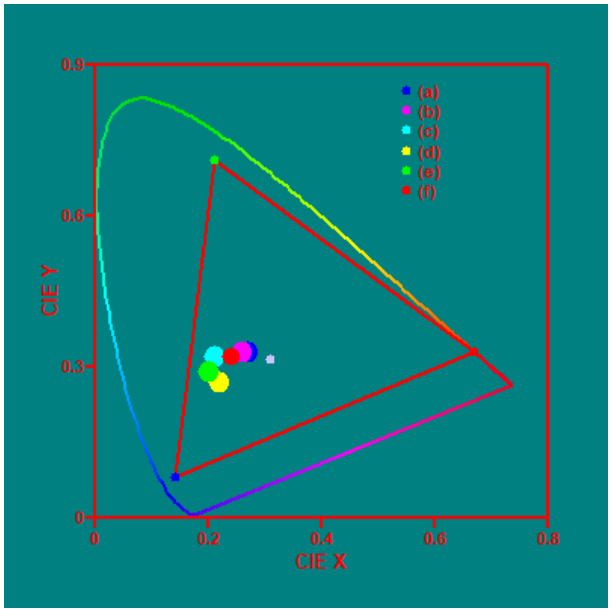

Figure 4.3: CIE 1931 chromaticity coordinates of the $SrSiO_3/SiO_2$ phosphors prepared by co-precipitation method at Sr/Si molar ratio of 1:1 (a), 2:1 (b), 2.5:1 (c), 3.5:1 (d), 1:2 (f) and hydrothermal method at a ratio of 2:1 (e). The white circle inside the red plot triangle represents white light. CIE coordinates were calculated using the software GoCIE obtained from http://www.geocities.com/krjustin/gocie.html.

The correlated color temperatures (CCT) of the two samples (1:1 and 2:1 molar ratio) closest to the neutral white light were also calculated from the CIE chromaticity coordinates obtained in figure 4.3 and found to be 9895 and 9167 K respectively. The two temperatures were calculated using McCamy analytical relation in equation 4.1 [23].

$$CCT = an^3 + bn^2 + cn + d \qquad (4.1)$$

where $n = (x - x_e)/(y - y_e)$ which denotes the inverse slope line and x_e and y_e are equal to 0.3320 and 0.1858 respectively. a = -437, b = 3601, c = -6861, and d = 5514.31.

4.3.4. Decay curves of the $SrSiO_3/SiO_2$ phosphor material

Time resolved measurements were performed with the purpose of studying the nature and lifetimes of different excited states in the $SrSiO_3/SiO_2$ phosphors and their phosphorescence decay curves are presented in figure 4.4 (a) to (f). All the decay curves acquisitions were monitored at 495 nm emission. To acquire more

understanding with regards to the decay components comprising the decay of phosphorescence in the studied phosphors presented in figure 4.4, the decays were analysed by means of fitting the data with HORIBA Scientific DAS6 analysis software. Upon comparison, the best model of fitting the data for the 495 nm emission in all samples was found to be a third exponential model in equation 4.2.

$$I(t) = A + B_1 \exp(-t/T_1) + B_2 \exp(-t/T_2) + B_3 \exp(-t/T_3) \quad (4.2)$$

where I represent the phosphorescence intensity, A is a background offset, B_1, B_2 and B_3 are the pre-exponential functions relating to how much of an emitting species there is in a phosphor material, t denotes time, and T represents the phosphorescence lifetime. The average lifetimes were utilized in order to make a comparison of the average amount of time it takes for electrons in the excited states in the $SrSiO_3/SiO_2$ nanophosphors and the amplitude-average lifetime [24] in equation 4.3 was utilized for the calculation of the average lifetime τ_{ave} of these electrons in their excited states, and the τ_{ave} values are also presented in figure 4.4.

$$\tau_{ave} = \sum_{i=1}^{n} B_i T_i \quad (4.3)$$

B and T still have the same meanings as in equation 4.2. It is worth mentioning here that, there was no clear evidence of concentration quenching from the decay curves as observed in section 4.3.3.

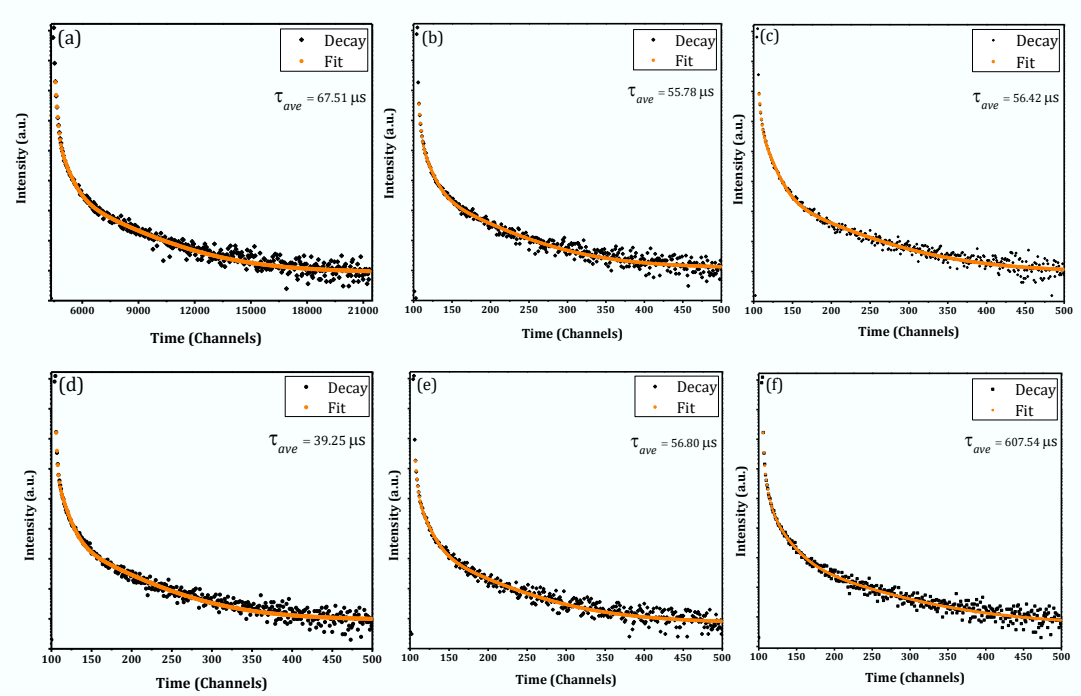

Figure 4.4: Phosphorescence decay curves of the $SrSiO_3/SiO_2$ phosphors prepared by co-precipitation method at Sr/Si molar ratio of 2.5:1 (a), 1:1 (b), 1:2 (c) 2:1 (d), 3.5:1 (e) and hydrothermal method at 2:1 (f). The solid black dots represent the experimental data, and the solid orange line is the fit of the data by third exponential model.

4.3.5. Thermoluminescence properties of the $SrSiO_3/SiO_2$ phosphor material

4.3.5.1. *General properties of a glow curve of the $SrSiO_3/SiO_2$ phosphor*

Thermoluminescence measurements were also performed to further study the defects in the $SrSiO_3/SiO_2$ phosphors prepared at different Sr/Si molar ratios and their spectra are presented in figure 4.5. Figure 4.5 (a), (b), (c), (d), and (e), show thermoluminescence glow curves of $SrSiO_3/SiO_2$ phosphors prepared by co-precipitation method at Sr/Si molar ratios of 2:1, 1:2, 1:1, 2.5:1, 3.5:1 respectively, whereas figure 4.5 (f) represent a glow curve of the same phosphor prepared by hydrothermal method at 2:1 Sr/Si molar ratio.

All glow curves in Figure 4.5 were acquired at a constant heating rate of 1 $^{o}C.s^{-1}$ after a beta irradiation of 2.5 kGy, except the glow curve in Figure 4.4 (b) which was irradiated for 600 Gy to avoid the PMT saturation at higher doses. Figure 4.5

(a) shows four peaks which are evident for this dose; two prominent ones at about 86 and 126 ^{o}C, together with weak ones at about 200, and 388 ^{o}C, which confirms four types of luminescence centers in this phosphor. This is also an indication of the presence of both shallow and deep traps in this phosphor, which are associated with intrinsic defects in this phosphor i.e. oxygen vacancies, Sr vacancies, substitutional Sr vacancies, interstitial Sr or Si vacancies since this is an undoped phosphor [25].

Evident in figure 4.5 (b) is a very intense peak at 84 ^{o}C and a very weak one at 136 ^{o}C. The intense nature of the low temperature peak suggests a competition between shallow and deep traps during trap filling, in which shallow traps get a preferential filling compared to deep ones, for the dose used [26]. Figure 4.5 (c) shows a glow curve with four peaks at 90, 126, 200, and 384 ^{o}C, which again suggests the presence of four different types of traps in this phosphor. Figure 4.5 (d) presents a glow curve consisting of three evident peaks at 96, 200, 408 ^{o}C, with no evidence of the 126 ^{o}C peak. This peak could have weakened in intensity due to competition of trap filling between a trap responsible for it and the one for the main peak at 96 ^{o}C. In figure 4.5 (e), four thermoluminescence peaks are evident at 86, 126, 200, 398 ^{o}C. Again, the 126 ^{o}C is now intense than the main peak at 86 ^{o}C, which is a suggestion of a competition of trap filling between the two traps. Figure 4.5 (f) shows a TL glow curve comprising of only a single TL peak situated at 100 ^{o}C. This is an indication that there is only one type of a trap in this phosphor.

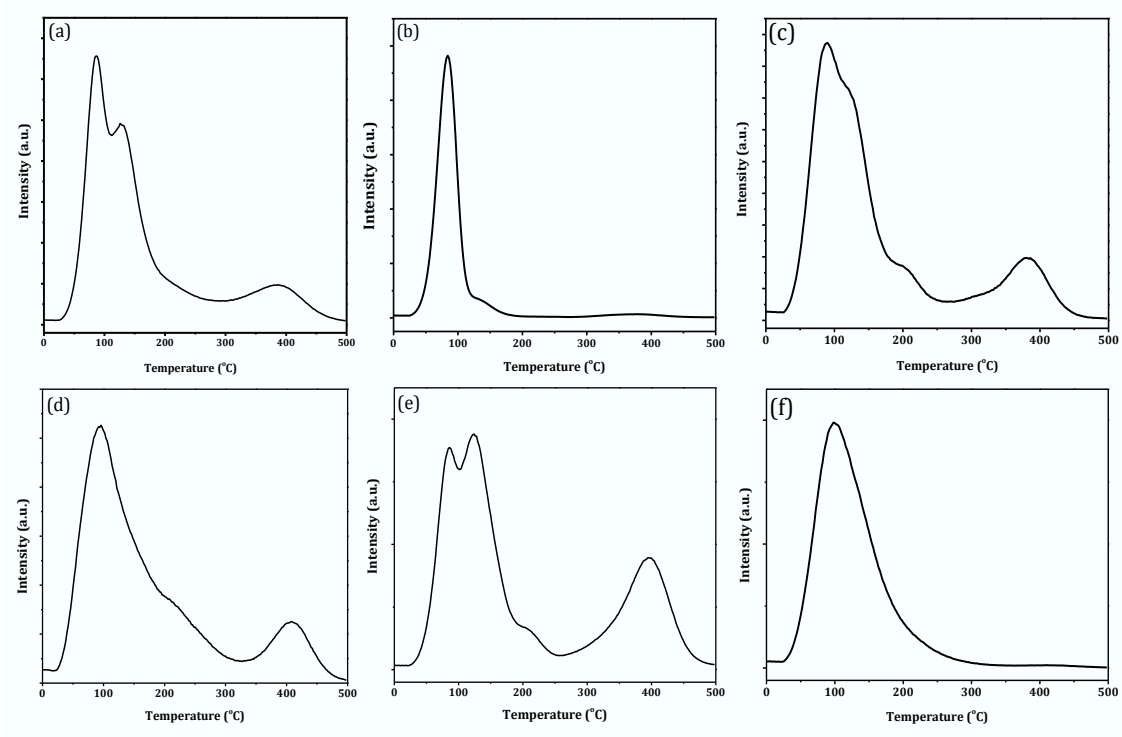

Figure 4.5: Thermoluminescence spectra of the $SrSiO_3/SiO_2$ phosphors prepared by co-precipitation method at Sr/Si molar ratio of 2:1 (a), 1:2 (b), 1:1 (c) 2.5:1 (d) 3.5:1 (e) and hydrothermal method at a ratio of 2:1 (f).

4.3.5.2. *Dose response.*

Dose response measurements were carried out and the spectra acquired for the $SrSiO_3/SiO_2$ phosphors prepared at diffent Sr/Si molar ratio are presented from figure 4.6 to figure 4.10. For ease of comparison and because the peaks at higher temperature side are of lower intensity and indeterminate, the dose response comparisons were done using a more prominent peak at lower temperature side. Figure 4.6 (a) shows a plot of TL glow curve of $SrSiO_3/SiO_2$ phosphor prepared by co-precipitation method at a 2:1 Sr/Si molar ratio, as a function of irradiation dose ranging from 0.3 kGy to 2.4 kGy. The TL spectra were acquired at a constant heating rate of 1 $^{o}C.s^{-1}$. It was observed in figure 4.6 (a) and (b) that the TL intensity increased as irradiation dose was increased and saturated at 2.1 kGy dose.

It was also noted from figure 4.6 (b) that the temperature at maximum TL intensity T_m did not shift to elevated or lower temperatures with an increase in dose. According to thermoluminescence theory, the peak T_m values are expected to change only as a function of heating rate (b=1). So, for a fixed heating rate, T_m position should not be influenced by other experimental parameters and should therefore remain constant [27,28,29]. In this case T_m of the first peak remains constant, which suggests that the first peak in this phosphor should be of first order kinetics [28].

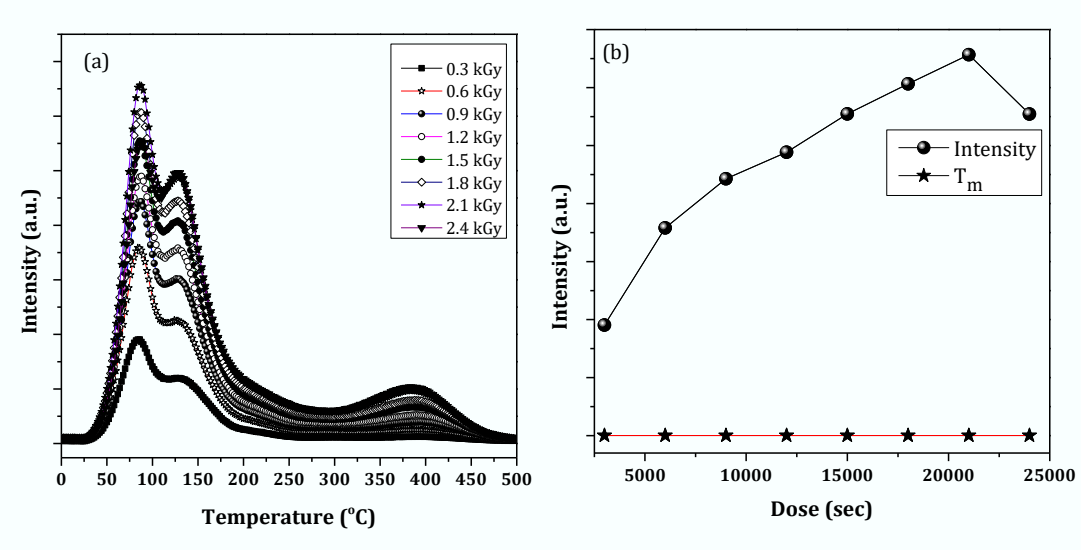

Figure 4.6: Dose response curves of the $SrSiO_3/SiO_2$ phosphors prepared at Sr/Si molar ratio of 2:1 by co-precipitation method (a). (b) is a plot showing changes in both maximum intensity I_m and temperature at maximum intensity T_m with irradiation dose.

Figure 4.7 (a) shows a plot of TL glow curve of $SrSiO_3/SiO_2$ phosphor prepared by co-precipitation method at a 1:2 Sr/Si molar ratio, as a function of irradiation dose from 60 Gy to 600 Gy. The spectral acquisitions were performed at a constant heating rate of 1 $^oC.s^{-1}$. Also observed in this phosphor was that, the thermoluminescence intensity increased with increasing dose without saturation in this dose range as presented in figure 4.7 (b). Worth noting in figure 4.7 (c) is that this phosphor showed a very high intensity at low doses. In fact, figure 4.7 (c) is clear evidence of the PMT saturation by the signal from this phosphor at

doses beyond 0.6 kGy [30]. The temperature at maximum TL intensity T_m also did not shift with an increase in dose in this phosphor. So as discussed above, the first peak in this phosphor should be of first order kinetics.

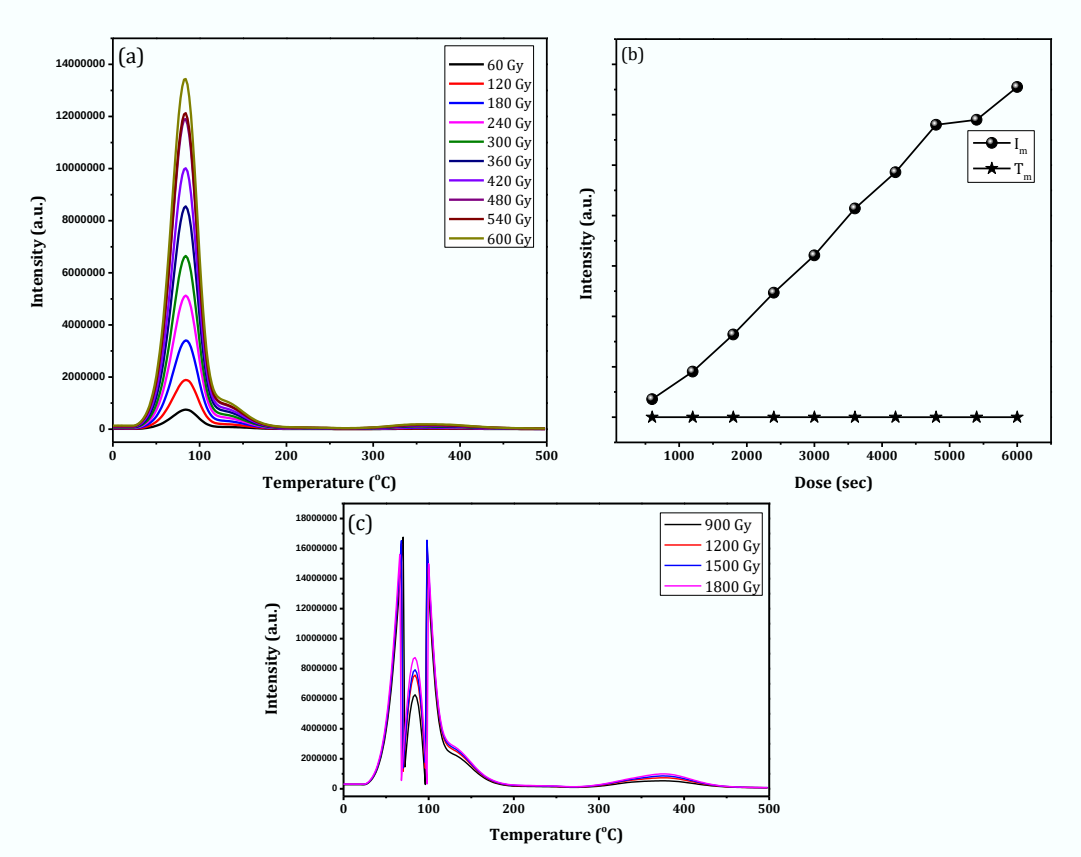

Figure 4.7: Dose response curves of the $SrSiO_3/SiO_2$ phosphors prepared at Sr/Si molar ratio of 1:2 by co-precipitation method (a). (b) is a plot showing changes in both maximum intensity I_m and T_m with irradiation dose. (c) is a plot of TL response to dose illustating a dose range beyond wich a high TL output from this phosphor saturates a detector.

Figure 4.8 (a) shows a plot of TL glow curve of $SrSiO_3/SiO_2$ phosphor prepared by co-precipitation method at a 1:1 Sr/Si molar ratio, as a function of dose from 0.3 kGy to 2.4 kGy range. The TL spectra were acquired at a constant 1 $^oC.s^{-1}$ heating rate. Also in this phosphor, the TL intensity was observed to increase as the

irradiation dose was increased until it saturated at 2.1 kGy dose and started to decrease with increasing dose as depicted in figure 4.8 (b). Also observed in figure 4.8 (b) was the temperature at maximum TL intensity T_m also did not show any shift towards higher or lower temperatures with an increasing dose in this phosphor. So as discussed above, the first peak in this phosphor should be of first order kinetics.

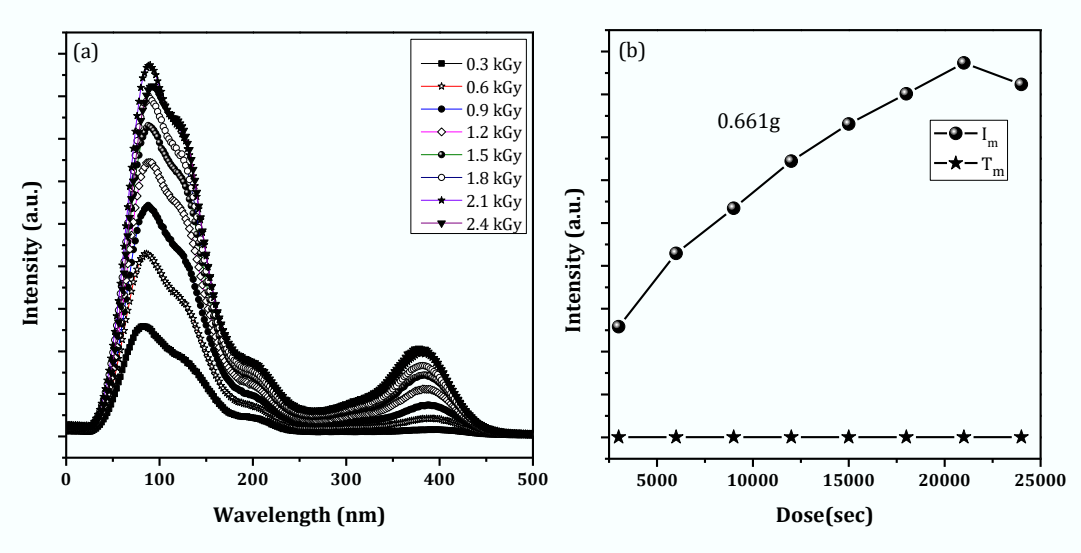

Figure 4.8: Dose response curves of the $SrSiO_3/SiO_2$ phosphors prepared at Sr/Si molar ratio of 1:1 by co-precipitation method (a). (b) is a plot showing changes in both maximum intensity I_m and temperature at maximum intensity T_m with irradiation dose.

Figure 4.9 (a) shows a plot of TL response glow curve of $SrSiO_3/SiO_2$ phosphor prepared by co-precipitation method at a 2.5:1 Sr/Si molar ratio, as a function of irradiation dose from 0.3 kGy to 2.4 kGy range. The acquisition of TL spectra were done at a constant heating rate of 1 $^oC.s^{-1}$. Also noted in this phosphor, the TL intensity increased as a function of beta irradiation dose until at 2.1 kGy dose where saturation occurred as evident in figure 4.8 (b). The temperature at

maximum TL intensity T_m also did not shift towards higher or lower temperatures with an increasing beta dose in this phosphor. Also, as discussed above, the first peak in this phosphor should be of first order kinetics.

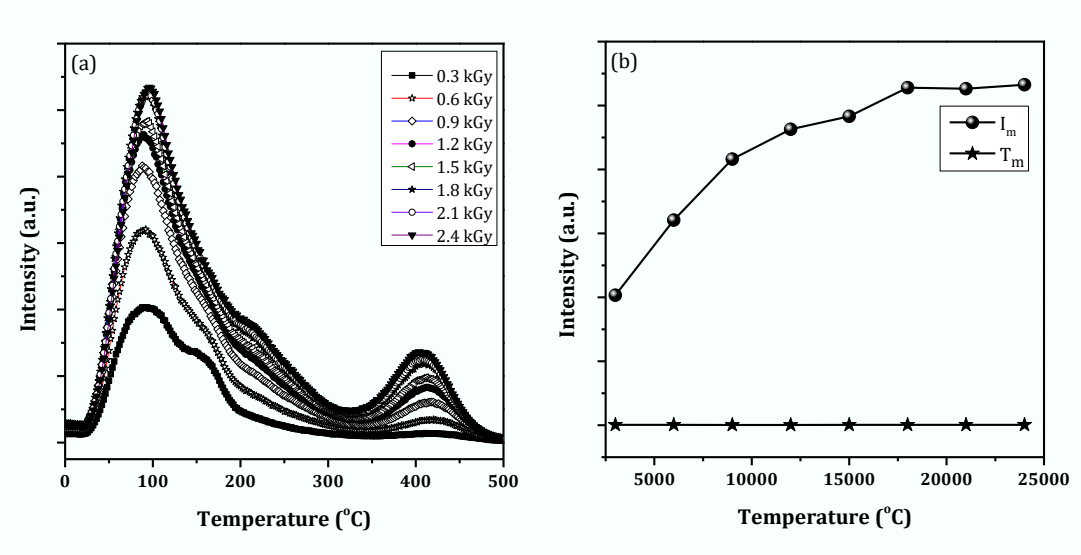

Figure 4.9: Dose response curves of the $SrSiO_3/SiO_2$ phosphors prepared at Sr/Si molar ratio of 2.5:1 by co-precipitation method (a). (b) is a plot showing changes in both maximum intensity I_m and temperature at maximum intensity T_m with irradiation dose.

Figure 4.10 (a) shows a plot of TL response glow curve of $SrSiO_3/SiO_2$ phosphor prepared by co-precipitation method at a 3.5:1 Sr/Si molar ratio, as a function of dose from 0.3 kGy to 2.4 kGy range. A constant heating rate of 1 $^oC.s^{-1}$ was used during TL spectral acquisitions. TL intensity of this phosphor was also observed to increase as the irradiation dose was increased until saturation at 2.1 kGy dose and started to decrease with an increase in dose as evident in figure 4.10 (b). The temperature at maximum TL intensity T_m also did not show a shift to lower or elevated temperatures when the irradiation dose was increased on this phosphor. Also, as discussed above, the first peak in this phosphor should be of first order kinetics.

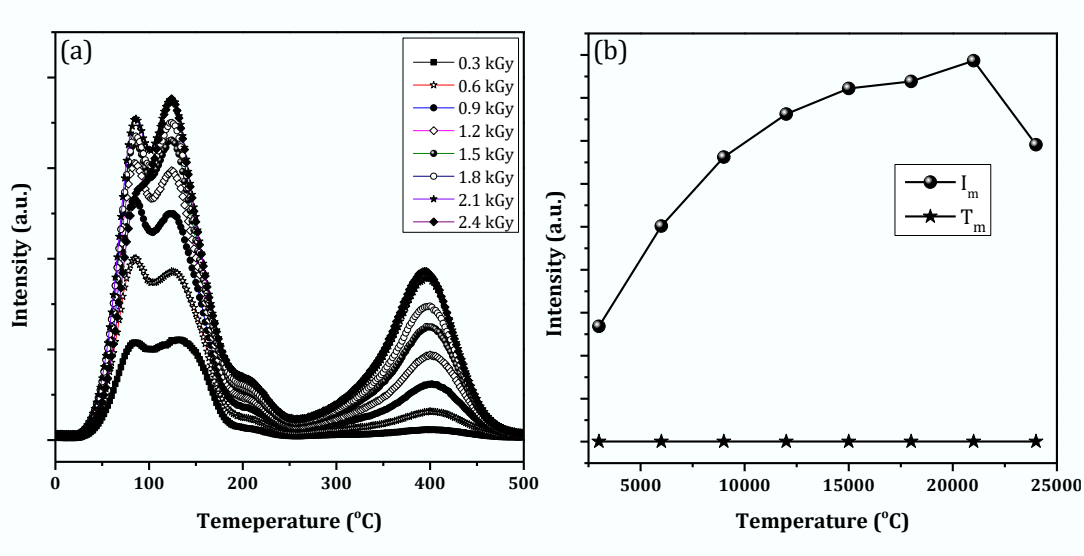

Figure 4.10: Dose response curves of the $SrSiO_3/SiO_2$ phosphors prepared at Sr/Si molar ratio of 3.5:1 by co-precipitation method (a). (b) is a plot showing changes in both maximum intensity I_m and temperature at maximum intensity T_m with irradiation dose.

4.3.5.3. *Heating rate response from the $SrSiO_3/SiO_2$ phosphors*

Just like dose, the heating rate is deemed a basic experimental variable in thermoluminescence measurements. TL spectra of the $SrSiO_3/SiO_2$ phosphors prepared at diffent Sr/Si molar ratio were acquired at varying linear heating rates from 0.5 to 9 $^oC.s^{-1}$ after irradiation dose of 2.5 kGy for the purpose of understanding the effect of heating rate on the glow curves of the prepared phosphors as presented in figure 4.11 to figure 4.15. Again, for ease of comparison and because the peaks at higher temperature side are of lower intensity and indeterminate, the heating rate response comparisons were done using only a more prominent peak at lower temperature side.

Figure 4.11 (a) and (b) show the TL response curves versus heating rate from both measured and the normalized data respectively of the $SrSiO_3/SiO_2$ phosphor prepared by co-precipitation method at a 2:1 Sr/Si molar ratio. Figure 4.11 (c) and (d) are the plots of T_m as a function of heating rate and I_m as a function of heating rate respectively. There is no change in the TL glow curve structure that

was observed at various heating rates in figure 4.11. Noted from figure 4.11 (a) to (c) was that, the temperature at maximum T_m was observed to be shifting to elevated temperatures with the increase in heating rate, β, and this is consistence with thermoluminescence theory. Similar changes in T_m with heating rates have been reported in many TL materials [31,32,33].

This phenomenon is well known as the temperature lag effect [34], in which the temperature lag between the heating element and the sample are different. In other words, the temperature recorded by TL reader, which is that of the heating element, is actually not the same as that of the sample, instead it is higher [35]. The sample heated with a relatively lower heating needs a longer time to release the same amount of electrons from traps as compared to the one heated with a higher heating rate [34].

Also, noted in figure 4.11 (d) was the decrease in TL intensity I_m and area under the main peak as the heating rate was increased. These are two evidence that the peak studied in this chapter is affected by thermal quenching [34], a process due to which the thermoluminescence efficiency η_{TL} in equation 4.4 [36] tends to be suppressed as the temperature is raised.

$$\eta_{TL} = \frac{P_r}{P_r + P_{nr}} \tag{4.4}$$

Here P_r represents the probability of luminescence transitions, which unlike the probability of non-radiative transitions P_{nr}, is dependent on temperature. Basically, at elevated temperatures, the competition between radiative and non-radiative transitions tend to favor the non-radiative transitions and this usually comes with a consequence of suppressing the luminescence efficiency, hence a decrease in TL intensity.

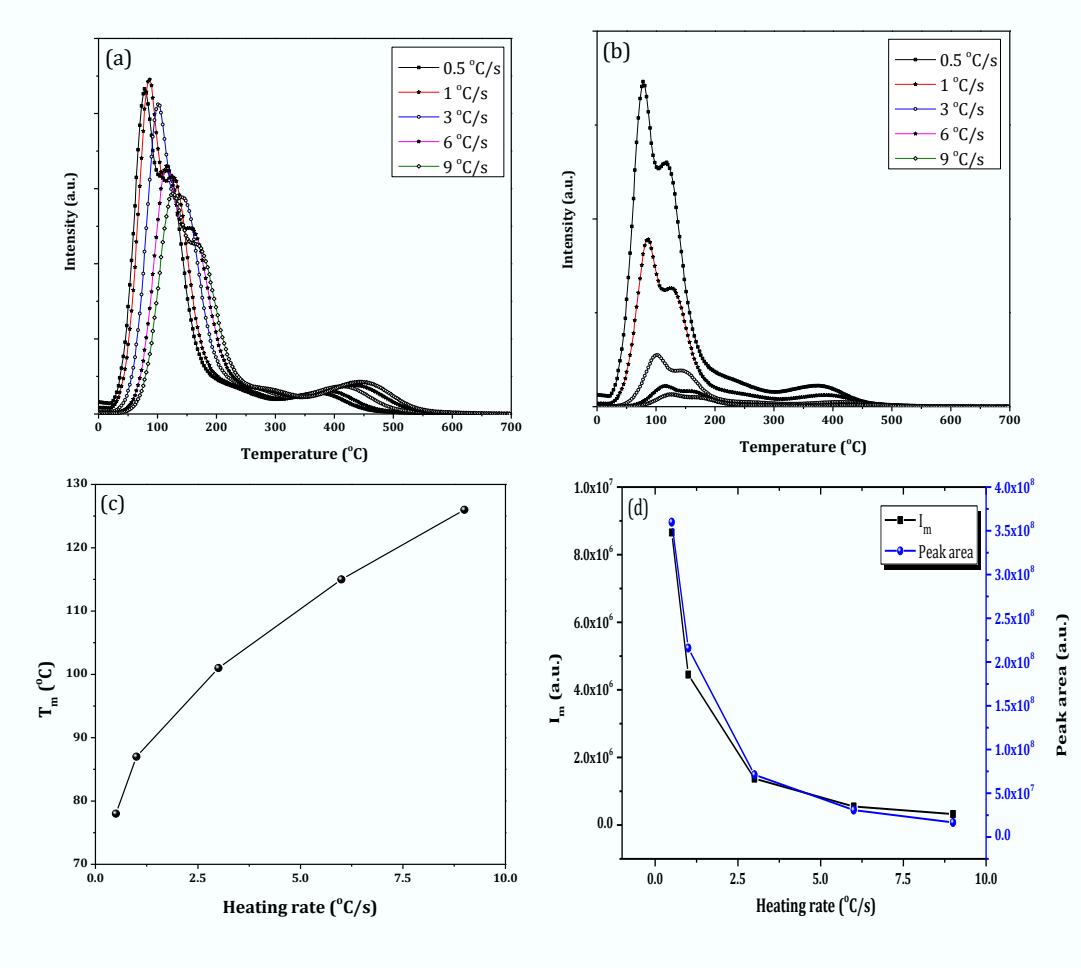

Figure 4.11: Heating rate response curves from raw data of the $SrSiO_3/SiO_2$ phosphors prepared at Sr/Si molar ratio of 2:1 by co-precipitation method (a). (b) is plot of the data used in (a) but normalized with respect to heating rate β. (c) is a plot of temperature at maximum T_m against heating rate, whereas (d) is a plot showing the behaviours of both maximum intensity I_m and peak area as heating rate is increased.

Figure 4.12 (a) and (b) show the TL response curves versus heating rate from both measured and the normalized data of the $SrSiO_3/SiO_2$ phosphor prepared by co-precipitation method at a 1:2 Sr/Si molar ratio. Figure 4.12 (c) shows the behavior of T_m, while Figure 4.12 (d) presents the behavior of I_m and peak area all as functions of heating rate. There was no change in the TL glow curve structure observed at various heating rates in figure 4.12. Noted from figure 4.12 (a) to (c) again was that the temperature at maximum T_m shifted to higher temperatures with increasing heating rate, β. Also, observed in figure 4.12 (d) was that both TL intensity I_m and area under the main peak decreased as the

heating rate was increased. Again, these two observations confirm this peak to be affected by thermal quenching.

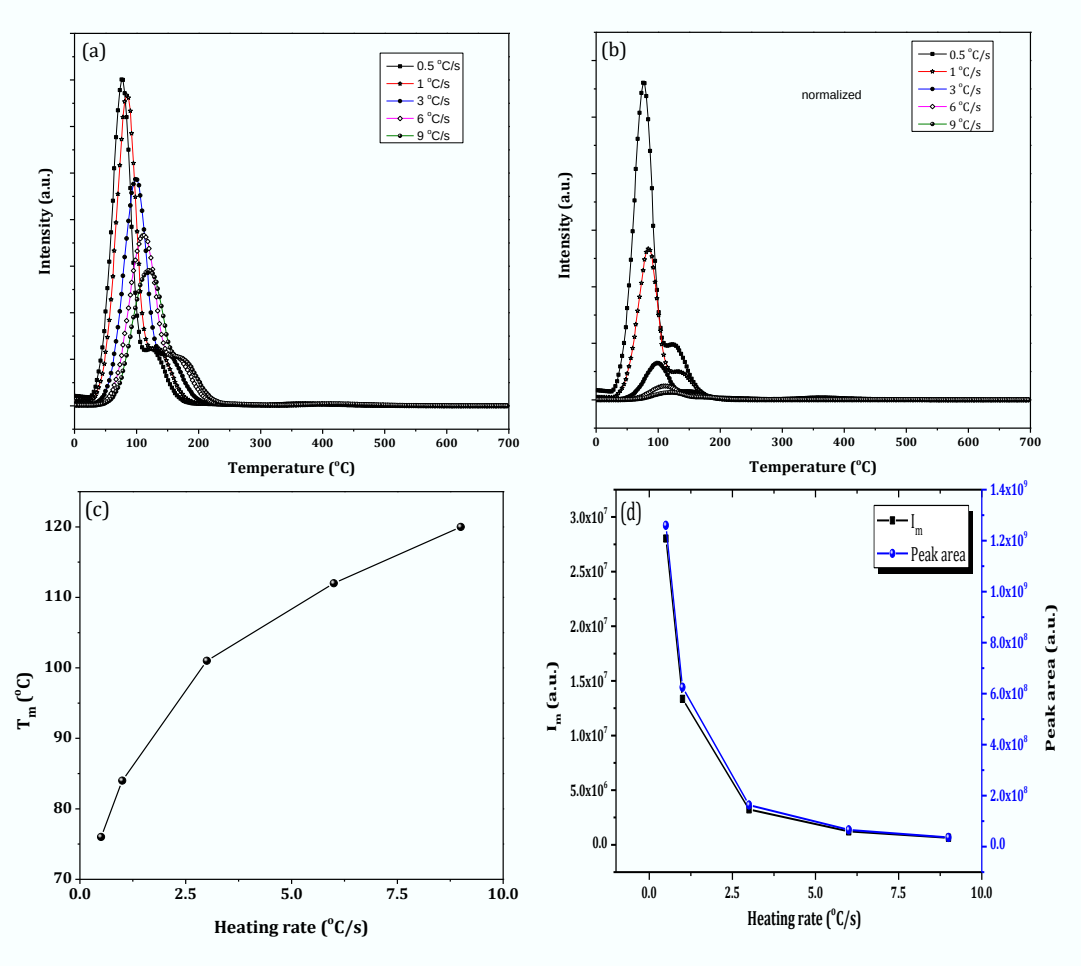

Figure 4.12: Heating rate response curves of the $SrSiO_3/SiO_2$ phosphors prepared at Sr/Si molar ratio of 1:2 by co-precipitation method (a). (b) is plot of the data used in (a) but normalized with respect to heating rate β. (c) is a plot of temperature at maximum T_m against heating rate, whereas (d) is a plot showing the behaviours of both maximum intensity I_m and peak area as heating rate is increased.

Figure 4.13 (a) and (b) show the TL response curves against heating rate from both measured and the normalized data of the $SrSiO_3/SiO_2$ phosphor prepared by co-precipitation method at a 1:1 Sr/Si molar ratio. Figure 4.13 (c) is a plot showing the behavior of peak temperature at maximum intensity T_m as the heating rate increases, whereas Figure 4.13 (d) is a plot showing the response of

TL intensity at maximum I_m and peak area also as the heating rate is varied. The TL glow curve structure was observed to remain unchanged at various heating rates in in this phosphor as well. T_m was observed to be shifting to higher temperatures as the heating rate was increased as evident in figure 4.13 (a) to (c). Again, the decrease in I_m and peak area with an increasing heating rate in figure 4.13 (d) are a confirmation of thermal quenching on the studied peak.

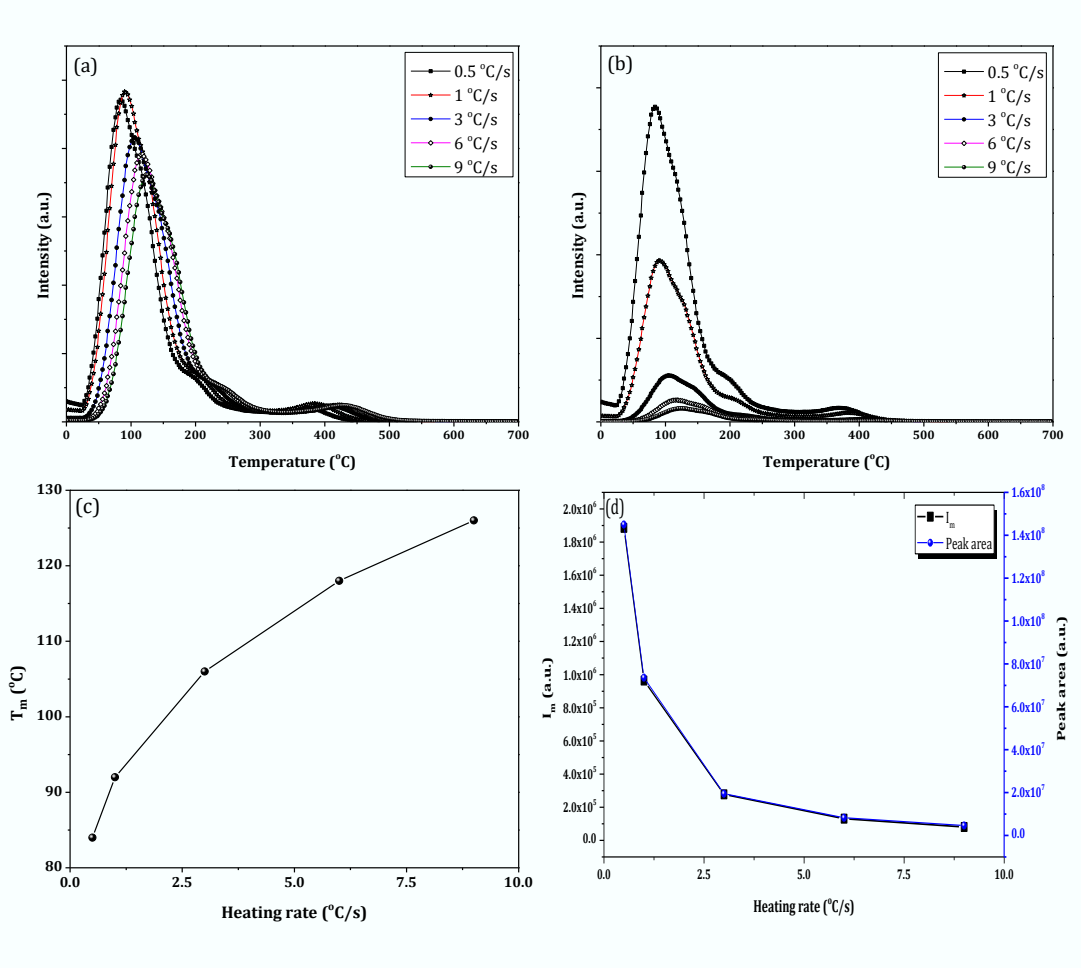

Figure 4.13:: Heating rate response curves of the $SrSiO_3/SiO_2$ phosphors prepared at Sr/Si molar ratio of 1:1 by co-precipitation method (a). (b) is plot of the data used in (a) but normalized with respect to heating rate β. (c) is a plot of temperature at maximum T_m versus heating rate, whereas (d) is a plot showing the behaviours of both maximum intensity I_m and peak area as heating rate is increased.

Figure 4.14 (a) and (b) show the TL response curves against heating rate from both measured and the normalized data of the $SrSiO_3/SiO_2$ phosphor prepared by co-precipitation method at a 2.5:1 Sr/Si molar ratio. Figure 4.14 (c) represents a

plot showing the behavior of peak temperature at maximum intensity T_m as the heating rate increases, whereas Figure 4.14 (d) depicts a plot which shows the response of TL intensity at maximum I_m and peak area as the heating rate is varied. The TL glow curve structure remained unaffected by the varying heating rates in the 0.5 to 9 $^oC.s^{-1}$ range in this phosphor as well. T_m was noted to be shifting to elevated temperatures with the increasing heating rate as shown in figure 4.14 (a) to (c). Again as evidence of thermal quenching on this peak in figure 4.14 (d), I_m and peak area decreased as the heating rate was increased.

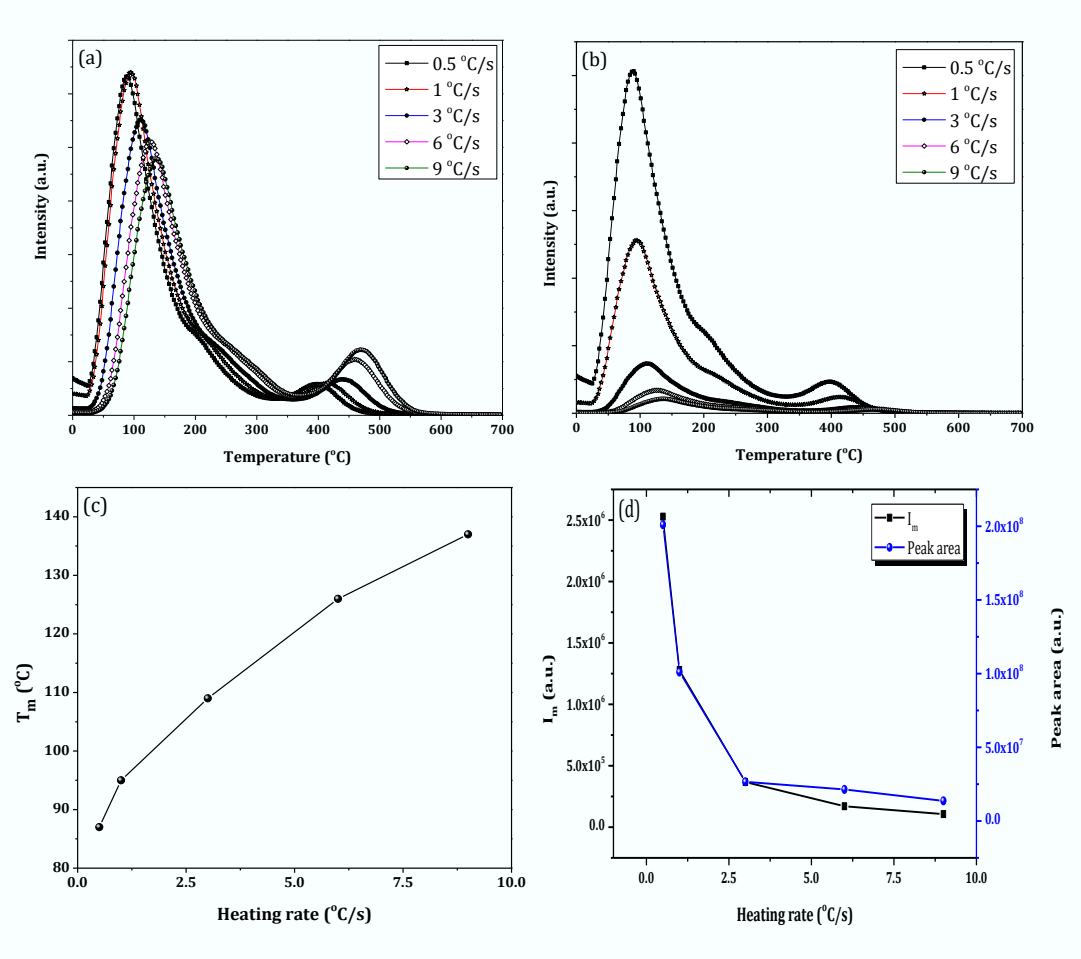

Figure 4.14: Heating rate response curves of the $SrSiO_3/SiO_2$ phosphors prepared at Sr/Si molar ratio of 2.5:1 by co-precipitation method (a). (b) is plot of the data used in (a) but normalized with respect to heating rate β. (c) is a plot of temperature at maximum T_m versus heating rate, whereas (d) is a plot showing the behaviours of both maximum intensity I_m and peak area as heating rate is increased.

Figure 4.15 (a) and (b) show the TL response curves against heating rate from both measured and the normalized data respectively of the $SrSiO_3/SiO_2$ phosphor prepared by co-precipitation method at a 3.5:1 Sr/Si molar ratio. Figure 4.15 (c) and (d) are the plots of T_m as a function of heating rate, together with both I_m and peak area as functions of heating rate respectively. The TL glow curve structure remained unaffected by the changing heating rates in this phosphor as well. T_m seemed to be shifting towards higher temperatures with the increasing heating rate as shown in figure 4.15 (a) to (c). Again, a decrease in TL intensity I_m and peak area with an increasing heating rate was observed in figure 4.15 (d), which is a confirmation of thermal quenching on this peak.

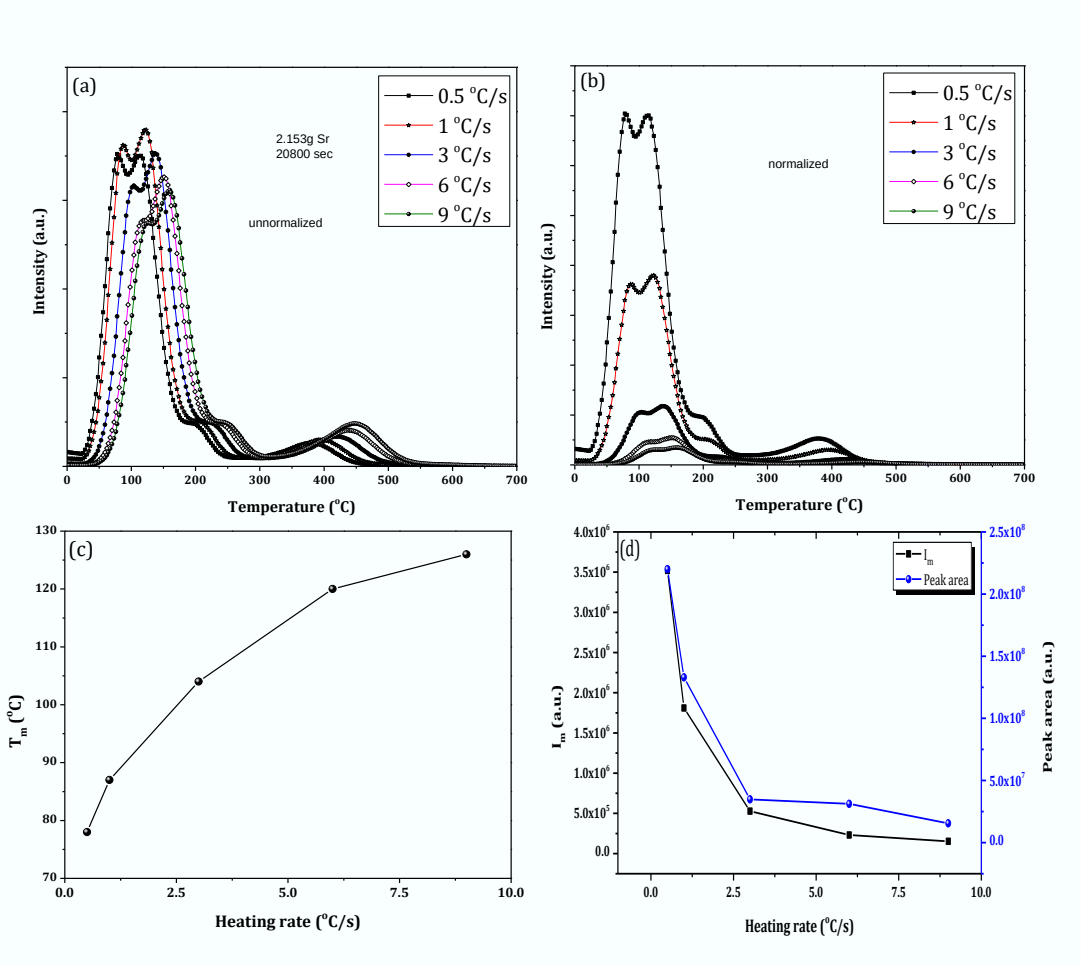

Figure 4.15: Heating rate response curves from raw data and normalized data (a) and (b) respectively, of the $SrSiO_3/SiO_2$ phosphors prepared at Sr/Si molar ratio of 3.5:1 by co-precipitation method. (c) is a plot of temeprature at maximum intensity T_m as a function of heating rate, wheas (d) is a plot showing the behaviours of both maximum intensity I_m and peak area.

4.4. Conclusion

Photo and thermoluminescence properties of the $SrSiO_3/SiO_2$ phosphors prepared at different Sr/Si molar ratios were investigated. An intense white room temperature phosphorescence was obtained from all the $SrSiO_3/SiO_2$ phosphors of different molar ratios. The origin of phosphorescence in the $SrSiO_3/SiO_2$ phosphors were attributed to the oxygen related defects in these phosphors. At higher Sr/Si molar ratio, there seemed to be a disappearence of the 687 nm

emission band, which from theory, reduces the quality of white light from this phosphor. Although a direct corelation between the Sr/Si molar ratio and the disappearence of this peak could not be observed, it was hypothesized that the emission responsible for this peak was quenched by a higher oxygen defects induced at higher Sr concentrations. Thermoluminescence studies illustrated a linear dose response up to absorbed dose of 2.1 kGy under beta irradiation for all samples except the 1:2 molar ratio sample which had a higher inensity to saturate the PMT detector at lower doses. Dose response studies on the main peak also showed a non changing T_m, suggesting this peak is a first order peak. Variable heating rate on this peak confirmed evidence of thermal quencing in the main peak, through a decrease in I_m and area of the peak for all the samples.

REFERENCES

1. L. Dua, G. Hea, Y. Gonga, W. Z. Yuanb, S. Wangc, C. Yua, Y. Liua, C. Wei, Efficient persistent room temperature phosphorescence achieved through Zn^{2+} doped sodium carboxymethyl cellulose composites, Composites Communications 8 (2018) 106–110.

2. Z. An, C. Zheng, Y. Tao, R. Chen, H. Shi, T. Chen, Z. Wang, H. Li, R. Deng, X. Liu, Stabilizing triplet excited states for ultralong organic phosphorescence, Nat. Mater. 14 (2015) 685–690.

3. L. Vijayalakshmi, K. Naveen Kumar, Pyung Hwanga, Tailoring ultraviolet-green to white light via energy transfer from Tb^{3+} - Eu^{3+} codoped glasses for white light-emitting diodes, scripta materialia, 187 (2020) 97-102.

4. L. Naixu, L. Shuqiang, W. Yueming, Z. Bingyao, S. Yueming, Z. Jiancheng, Luminescent properties and energy transfer of color-tunable $Sr_3Y_2(SiO_3)_6$:Ce^{3+},Tb^{3+} phosphors, Journal Of Rare earths, 32, 2014.

5. Yongbiao Hua ZunhuaLi, Synthesis and photoluminescence Sr_2LaTaO_6:Mn^{4+} phosphors with ultrahigh color purity for good CRI warm-WLED devices, Optik - International Journal for Light and Electron Optics 242 (2021) 167348.

6. Yaomiao Feng, Jinping Huang, Lili Liu, Jie Liu and Xibin Yu, Enhancement of white-light-emission from single-phase $Sr_5(PO_4)_3F$:Eu^{2+},Mn^{2+} phosphors for near-UV white LEDs, Dalton Trans., 2015, 44, 15006–15013.

7. Jinyong Kuang, Yingliang Liu, Jianxian Zhang , White-light-emitting long-lasting phosphorescence in Dy^{3+}-doped $SrSiO_3$, Journal of Solid State Chemistry 179 (2006) 266–269.

8. LI Naixu, LI Shuqiang, WANG Yueming, ZHOU Bingyao, SUN Yueming, ZHOU Jiancheng, Luminescent properties and energy transfer of color-tunable $Sr_3Y_2(SiO_3)_6:Ce^{3+},Tb^{3+}$ phosphors, JOURNAL OF RARE EARTHS, 2014, P. 933.

9. C.R. Garcia, J. Oliva, L.A. Diaz-Torres, E. Montes, G. Hirata, J. Bernal-Alvarado, C. Gomez-Solis, Controlling the white phosphorescence $ZnGa_2O_4$ phosphors by surface defects, ceramic international 45 (2019) 4972-4979.

10. J.-L. Zhang, G.-Y. Hong, in Modern Inorganic Synthetic Chemistry (Second Edition), 2017.

11. Arthur D. Pelton, in Phase Diagrams and Thermodynamic Modeling of Solutions, 2019.

12. N. Suriyamurthy, B.S. Panigrahi, Effects of non-stoichiometry and substitution on photoluminescence and afterglow luminescence of $Sr_4Al_{14}O_{25}:Eu^{2+}$, Dy^{3+} phosphor, Journal of Luminescence 128 (2008) 1809–1814.

13. Esra Öztürk, Photoluminescence Properties of Eu^{3+}-activated Silicate Phosphors, High Temp. Mater. Proc. 2017; 36(6): 635–640.

14. Ishwar Prasad Sahu, D.P. Bisen, Raunak Kumar Tamrakar, K.V.R. Murthy, M. Mohapatra, Luminescence studies on the europium doped strontium metasilicate phosphor prepared by solid state reaction method, Journal of Science: Advanced Materials and Devices (2017) 1-10.

15. H. Huang, X. Sun, S. Wang, Y. Liu, X. Li, J. Liu, Z. Kang, and S. Lee, Strong red emission of pure Y_2O_3 nanoparticles from oxygen related defects, Dalton Trans., 2011, 40, 11362.

16. M.S. Dhlamini, J. J. Terblans, R.E. Kroon, O.M. Ntwaeaborwa, J.M. Ngaruiya, J.R. Botha and H.C. Swart, Photoluminescence properties of SiO_2 surface-passivated PbS nanoparticles, South African Journal of Science 104, September/October 2008,

17. Laurent Cormier, Georges Calas, Brigitte Beuneu, Structural changes between soda-lime silicate glass and melt, journal of nano-crystalline solids 357 (2011) 926-931

18. Ishwar Prasad Sahu , D.P. Bisen, K.V.R. Murthy, M. Mohapatra, Luminescence Studies on the europium doped strontium metasilicate phosphor prepared by solid state reaction method, journal of science: Advanced Materials and Devices 2 (2017) 59-68.

19. Bao-gai Zhai, Hanfei Xu, Qing Zhang, and Yuan Ming Huang, Blue Photoluminescence and Cyan-Colored Afterglow of Undoped $SrSO_4$ Nanoplates, ACS Omega 2021, 6, 10129−10140.

20. Magali Benoit, Simona Ispas, Mark E. Tuckerman, Structural properties of molten silicates from ab initio molecular-dynamics simulations: comparison between CaO-Al_2O_3-SiO_2 and SiO_2, 2018.

21. Joseph Davidovits, Geopolymer, Green Chemistry and Sustainable Development Solutions: Proceedings of the World Congress Geopolymer 2005.

22. Kohta Nambu, Hitoshi Hayasaka, Takahisa Yamamoto, and Hidehiro Yoshida, Photoluminescence properties of undoped and Si^{4+}-doped polycrystalline Y_2O_3 phosphors prepared by flash-sintering, Applied Physics Express 12, 075504 (2019).

23. C. Li, G. Cui, M. Melgosa, X. Ruan, Y. Zhang, L. Ma, K. Xiao, and M. R. Luo, Accurate method for computing correlated color temperature, optics express 14066, 24, 2016

24. A. Sillen and Y. Engelborghs, J. Photochem. Photobiol 67(5) (1998) 475–486.

25. EFM Kombe-Atang and ML Chithambo, Phototransferred thermoluminescence and phosphorescence related to phototransfer in annealed synthetic quartz, SA Institute of Physics, ISBN: 978-0-620-70714-5.

26. David Van der Heggen, Dimitri Vandenberghe, Nasrin K. Moayed, Johan De Grave, Philippe F. Smet, Jonas J. Joos, The almost hidden role of deep traps when measuring afterglow and thermoluminescence of persistent phosphors, Journal of luminescence 226 (2020) 117496.

27. M. Yuksel, Z. G. Portakal, T. Dogan, M. Topaksu, E. Unsal, Thermoluminescence glow curve properties of TLD-500 dosimeter, Third international conference on radiation and applications in various fields of research, ISBN: 978-86-80300-01-6.

28. M.S. Rasheedy, A.M.A. Amry, On the frequency factor obtained in case of thermoluminescence second order kinetics, J. Lumin. 63 (1995) 149 –154.

29. A.N. Yazici, and M. Topaksu, 2003. "The analysis of thermoluminescence glow peaks of unannealed synthetic quartz", Journal of Physics D: Applied Physics, 36:620-627.

30. P. Bilski, W. Gieszczyk, B. Obryk and K. Hodyr, comparison of commercial thermoluminescent readers regarding high-dose high-temperature measurements, radiation measurements.

31. E. Cruz-Zaragoza, P.R.Gonza´ lez, J.Azorı´n, C.Furetta, Heating rateeffectonthermoluminescenceglowcurvesof LiF:Mg,Cu,P+PTFE phosphor, Applied radiation and isotopes 69 (2011) 1369-1373.

32. Sunil Thomas, M.L. Chithambo, General features and kinetic analysis of thermoluminescence from annealed natural quartz, Journal of luminescence 197 (2018) 406-411.

33. B. Subedi, D. Afouxenidis, G.S. Polymeris, K. Bakoglidis, S. Raptis, N.C. Tsirliganis, G.Kitis, Thermal quenching of thermoluminescence in quartz samples of various origins, Mediterranean Archaeology and Archaeometry, Vol. 2010, No. 4, pp. 69-75.

34. S. Balci-Yegena, M. Yüksela, N. Kucukb, Y. Karabulutc, M. Ayvacikli. Can, M. Topaksu, Thermoluminescence dose and heating rate dependence and kinetic analysis of ZnB_2O_4:0.05Dy^{3+} phosphor, Nuclear Inst, and Methods in physics Research B 416 (2018) 50-54.

35. T. Rivera Montalvo , C. Furetta , G. Kitis , J. Azorín & R. M. Vite, Radiat. Eff. Defects Solids 159 (2004) 217-222.

36. Claudio Furetta, Pao-Shan Weng, Operational Thermoluminescence Dosimetry, World Scientific, 1998 – 252.

CHAPTER 5

Thermoluminescence investigation of the $SrSiO_3/SiO_2$ phosphor with 2:1 Sr/Si molar ratio for dosimetry applications

5.1. Introduction

Thermoluminescence phenomenon displayed by phosphor materials through light emission following thermal stimulation is often useful in applications in interesting fields such as radiation dosimetry [1,2]. For a phosphor material to be deemed suitable for a particular application, a careful study on it's physical properties such as the nature of defects (traps and recombination centres within the band gap) which are either inevitably formed during the synthesis process or intentionally incorporated has to be carried out. So, depending on the nature and number of defects in a phosphor material, a TL glow curve acquired during the read out takes a particular shape.

This glow curve and its shape contain important detailed information with regards to the kinetics involved in thermoluminescence process, and the thermoluminescence parameters such as activation energy *E*, kinetics order *b*, and frequency factor *s* are evaluated from it [3,4]. There are several models reported in literature which were used for the estimation of the values of these parameters. One of them is the variable heating rate method which is reported to be a widely used model of calculating the activation energy of a trap, in other words, an estimation of how deep the trap is from conduction or the valence band of a particular material [5,6]. This is the method that was proposed by Hoogenstraaten [7] when he suggested a way to estimate the activation energy from a plot of T^2_m/B vs. $1/T_m$, from which the activation energy can be calculated from the slope E/k [5].

One other method of estimating the activation energy is the initial rise method from a glow curve through a plot of In(TL) vs. 1/T, which yields a straight line, the slope of which helps to evaluate the *E* value [6]. Another well-known and used

method of analysing a thermoluminescence glow curve for the purpose of acquiring significant information with regards to the kinetic parameters E, s, and b is the Chen's peak shape method, where the shape or geometrical properties of the peak are considered. Here the symmetric peaks are characterised as second order peaks, whereas first order ones are asymmetric [8,9]. Through the calculation of the so-called geometrical shape or symmetry factor, the order of kinetic followed by a certain trap can be established [9].

In this chapter, the behaviour of kinetic parameters with dose and heating rate were studied. In particular, the change in both thermoluminescence intensity I_m and temperature corresponding with maximum intensity T_m as functions of both beta dose (linearity) and heating rate are studied to evaluate the possibility of the application of the $SrSiO_3/SiO_2$ phosphor in dosimetry. It is well known from literature that for a phosphor material to be applicable in dosimetry, it needs to meet certain properties such as single peak on a glow curve, linearity between dose and light output over a wide range, emission spectrum in the visible range, preferably in the 400 – 500 nm range, etc [10]. So, amongst all the prepared $SrSiO_3/SiO_2$ phosphors with different molar ratios, only the 2:1 molar ratio prepared by hydrothermal method shows a single glow curve with no interfering glow peaks. It is for this reason that in this chapter only the 2:1 molar ratio prepared by hydrothermal method is studied for potential applications in dosimetry. The trapping parameters are also evaluated using different approaches from 2 methods in this chapter, namely the initial rise and variable heating rate methods.

5.2. Experimental

5.2.1. Sample preparation

The 2:1 Sr/Si molar ratio sample of $SrSiO_3/SiO_2$ phosphor was prepared by hydrothermal method. In the process, 1.5 g of strontium carbonate ($SrCO_3$) in analytical grade was separately dissolved into a 100 mL of deionised water, with

a few drops of nitric acid added to convert $SrCO_3$ into $(SrNO_3)_2$ and stirred at room temperature for 1 hour. After 1 hour, a second solution of 1 mL of tetraethyl orthosilicate (TEOS) in 10 mL of ethanol, with a few drops of nitric acid (HNO_3) which was also separately stirred for 30 minutes, was poured into the first solution, and allowed to stir for 30 minutes. This solution was then pH-adjusted to 9 using NaOH solution at 1:1 molar ratio with $SrCO_3$.

The resultant solution was then taken into a Teflon-lined stainless-steel autoclave, sealed, and kept at 180 ^oC for 24 h, after which it was allowed to cool to room temperature naturally. The resulting white product was filtered and washed with distilled water and absolute ethanol three times separately before drying at 100 ^oC overnight. The dried product was then ground in an agate mortar to a fine final product and annealed in air at 1050 ^oC, after which XRD measurements were performed for structure confirmation.

5.2.2. Characterization

5.2.2.1. Sample structure.

The XRD analysis of the prepare phosphor materials were covered in chapter 4, section 4.3.1.

5.2.2.2. Fourier transform infrared spectroscopy (FTIR).

The FTIR analysis of the prepare phosphor materials were also covered in chapter 4, section 4.3.2.

5.3. Results and discussion

5.3.1. General properties of a glow curve

Thermoluminescence measurements were performed to study the defects in a 2:1 Sr/Si molar ratios $SrSiO_3/SiO_2$ phosphor synthesized by hydrothermal method and the spectrum is presented in **figure 5.1**. A glow curve in **Figure 5.1** was acquired at a constant heating rate of 1 $^oC.s^{-1}$ after a beta irradiation of 1.8 kGy.

Figure 5.1 shows a glow curve which consisted of only a single thermoluminescence peak at 100 ^{o}C. This suggests that there is only one type of a trap in this phosphor. The insert of **figure 5.1** shows a PL emission spectrum in the visible range, peaking at 495 nm which is interestingly consistent with a dosimetry application requirement that a phosphor should emit preferably within a 400-500 nm emission range [10].

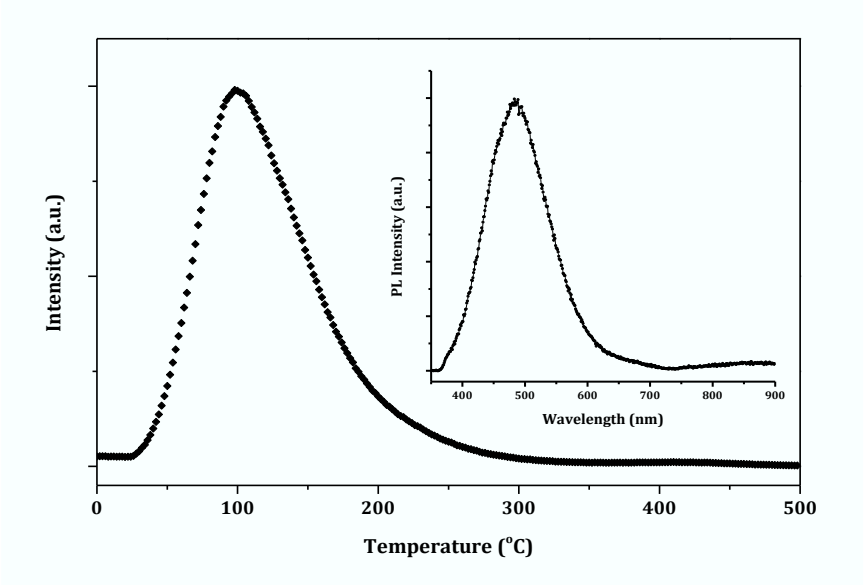

Figure 5.1: Thermoluminescence spectrum of the $SrSiO_3/SiO_2$ phosphors synthesized by hydrothermal method at 2:1 Sr/Si molar ratio. The insert is a PL spectrum of the same phosphor showing emission peak at 495 nm.

5.3.2. Dose response

Dose response measurements were carried out and the spectra acquired for the $SrSiO_3/SiO_2$ phosphor prepared at 2:1 Sr/Si molar ratio are depicted in **figure 5.2**. **Figure 5.2** (a) presents a plot of TL glow curve of $SrSiO_3/SiO_2$ phosphor prepared by hydrothermal method at a 2:1 Sr/Si molar ratio, as a function of beta dose in the range 0.3 kGy to 2.4 kGy. The acquisition of TL glow curves were done at a constant heating rate of 1 ^{o}C.s^{-1}. Observed from **figure 5.2** (a) and (b) was that the

thermoluminescence intensity increased linearly with the increasing dose and saturated at 1.8 kGy dose. This linearity of dose response over such a wide area is also consistent with the characteristics of a good dosimetric phosphor [10].

Noted also from **figure 5.2** (b), was a shift towards elevated temperatures of temperature corresponding with maximum TL intensity T_m with an increasing beta dose. In accordance with thermoluminescence theory, the T_m values are expected to change only with the change in heating rate. This shift in T_m position with increasing dose suggests that the studied peak in this phosphor could be of a non-first order kinetics [11].

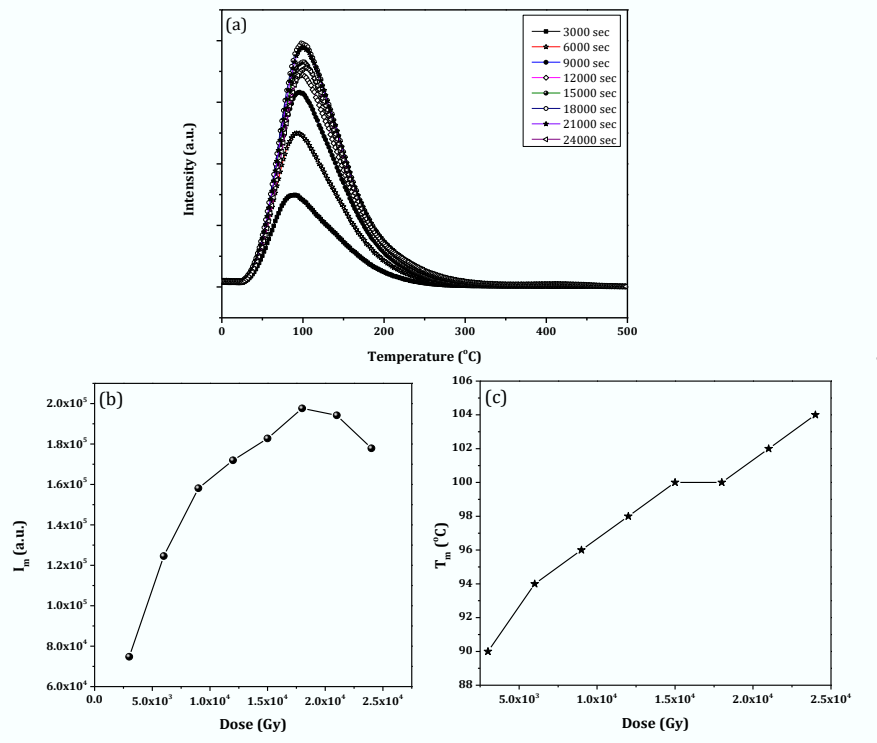

Figure 5.2: Dose response curves of the $SrSiO_3/SiO_2$ phosphors prepared at Sr/Si molar ratio of 2:1 by hydrothermal method (a). (b) and (c) are the plots of maximum intensity I_m and temperature at maximum intensity T_m both as functions of irradiation dose.

5.3.3. Heating rate response

TL measurements of a 2:1 molar ratio $SrSiO_3/SiO_2$ phosphor prepared by hydrothermal method were acquired at various linear heating rates in the range 0.5 to 9 $^oC.s^{-1}$, after irradiation dose of 1.8 kGy for the purpose of studying the effect of heating rate on its glow curve and the acquired spectra are presented in **figure 5.3**. **Figure 5.3** (a) and (b) represent plots (both measured and the normalized data) of TL response curves which show the behaviour of T_m as the heating rate was varied. **Figure 5.3** (c) and (d) are the plots of both peak T_m and TL I_m against heating rate respectively. There was no structural change in the glow curve observed at various heating rates in figure 5.3. Instead, it was noted in figure 5.3 (a) to (c), that T_m shifted towards higher temperature values with the increasing heating rate β.

This phenomenon is well known as the temperature lag effect [12], in which the temperature lag between the heating element and the sample are different. In other words, the temperature recorded by TL reader, which is that of the heating element, is actually not the same as that of the sample, instead, it is higher [13]. Also, the TL intensity I_m and the area under the curve as shown in **figure 5.3** (d) were observed to decrease as heating rate was increased. These two observed decreases are evidence of thermal quenching on the studied peak [13].

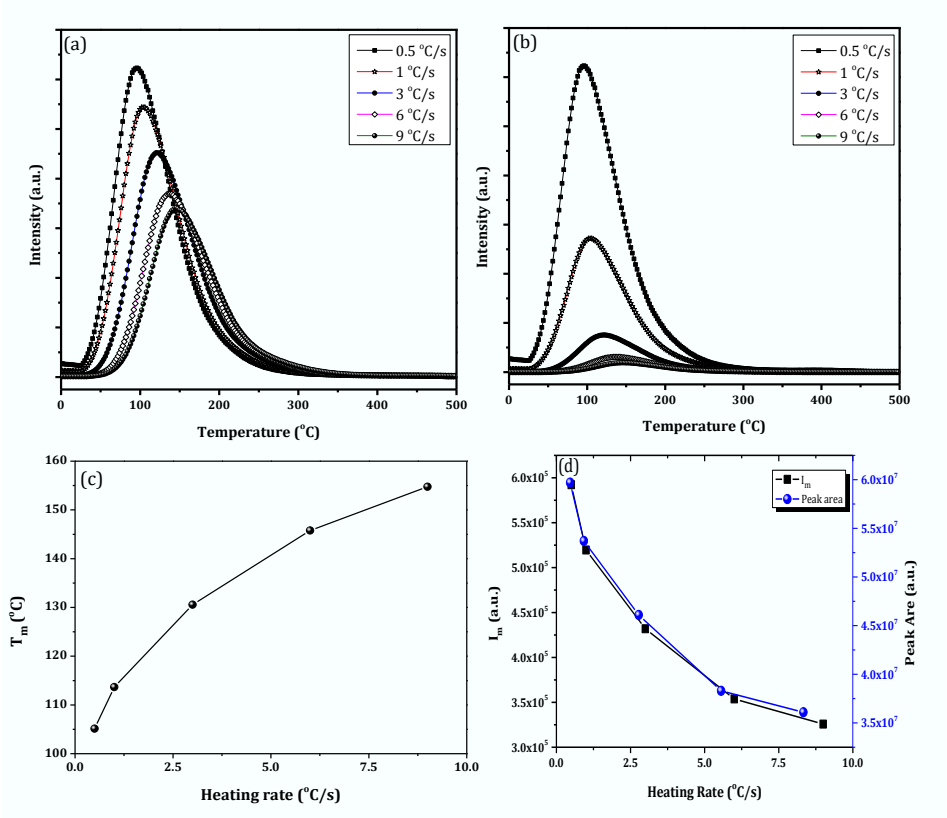

Figure 5.3: Heating rate response curves from raw and normalized data (a) and (b) respectively of the $SrSiO_3/SiO_2$ phosphors prepared at Sr/Si molar ratio of 2:1 by hydrothermal method. (c) is a plot of temperature at maximum intensity T_m as a function of heating rate. (d) is a plot of both maximum intensity I_m and Peak area as functions of heating rate.

5.3.4. Kinetic analysis on a glow curve

5.3.4.1 . The Initial Rise Method

The initial rise method, is the simplest experimental aproach that was first suggested by Garlick and Gibson to calculate the trap depth, a parameter that is independent of the order of kinetics involved in this method [14]. It was also used in this chapter to calculate the activation energy of the trap that is responsible for the 100 °C glow peak shown in figure 5.4 (a). This method is based on the approximation that the rate of change of trapped charges on the initial rise part of a TL glow curve, i.e. $T \ll T_m$ (temperature at maximum intensity) is negligible, such that the TL intensity I is proportional to $\exp(-E/kT)$, which can be expressed as in equation 5.1 [14,15].

$$I(T) = A.\exp\left(-E/kT\right) \tag{5.1}$$

where A is a constant, $I(T)$ is the TL intensity at any temperature T, E is the thermal activation energy and k is Boltzmann's constant. If In(T) is ploted against 1/T over the initial rise part of the TL glow curve, then a straight line having a slope $-E/k$ is obtained, from which the value of the activation energy E can be calculated. In this chapter, the first 11 data points representing portions of the TL glow curve which correspond with both 10 and 15% of the maximum TL intensity were used as shown in **figure 5.4**. Figure 5.4 (b) is plot of In(TL) vs 1/T using the entire data points of the whole glow curve in figure 5.4 (a), whereas **figure 5.4** (c) and (e) represent plots of In(TL) vs 1/T using all data points of 10 and 15 % of maximum TL intensiy respectively. **Figure 5.4** (d) and (f) represent only the linear parts of **Figure 5.4** (c) and (e) respectively.

The calculated values of E from this method are 0.693 and 0.733 eV for 10 and 15 % of maximum intensity respectively, which indicate that the trap associated with the peak investigated in this chapter is a shallow trap. Also, the initial rise method is commonly known to be sensitive to the number of data points and the portion of the initial rising part of a thermoluminescence glow curve used for ploting the In(TL) vs 1/T graph, hence the difference in E values for 10 and 15 % of maximum TL intensity. That is to say, theoretically, the initial rise method is valid only for temperatures that correspond to a thermoluminescence intensity which is lower than 10 – 15 %, the so called 15 % rule of thumb [16]. In this chapter, judging from the R-square value of both plots (d) and (f) which must be close to one for accurate results, 0.733 eV is a more accurately calculated value of E.

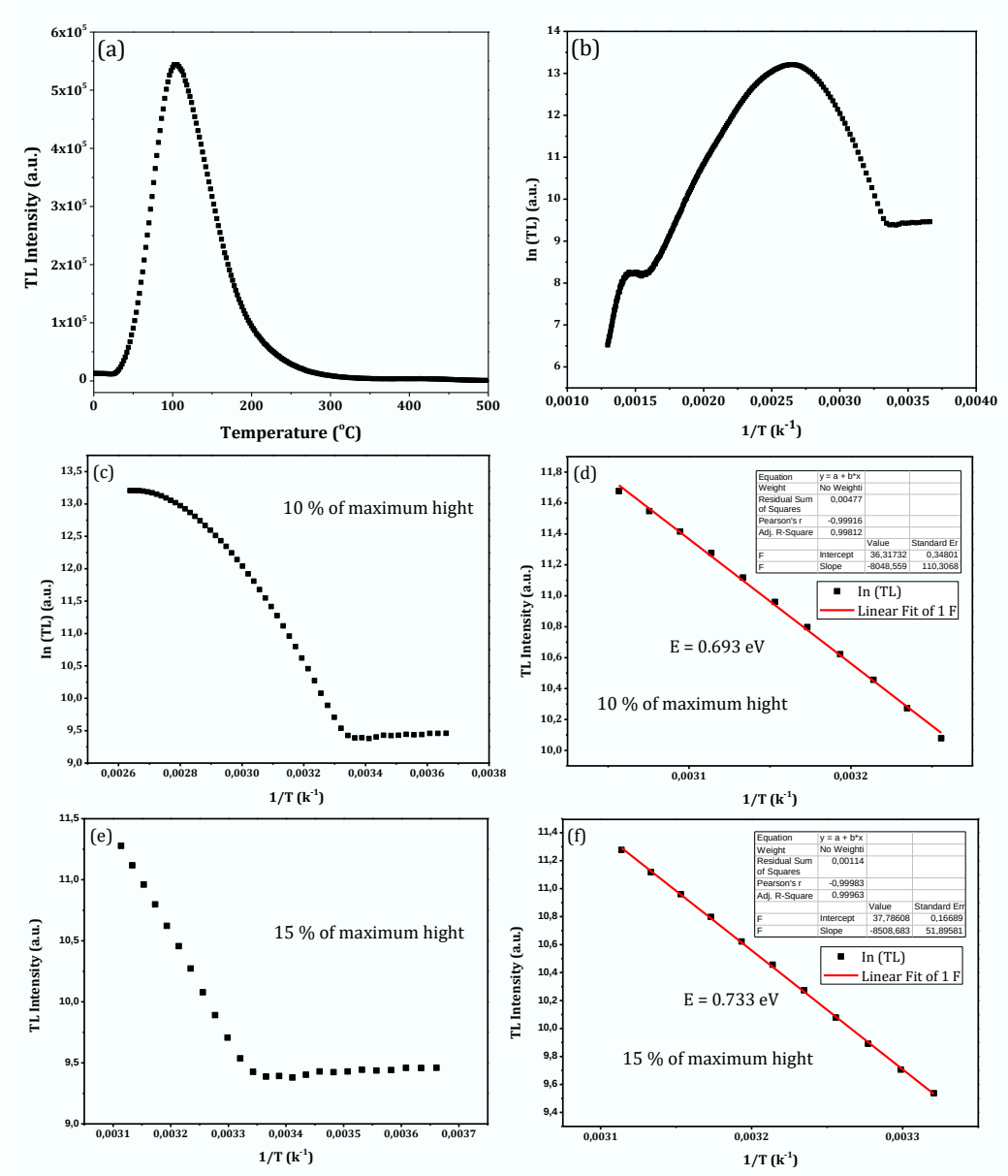

Figure 5.4: glow curve of a 2:1 Sr/Si molar ratio $SrSiO_3/SiO_2$ phosphor prepared by hydrothermal method plotted as ln(I) vs. 1/T for calculation of the activation energy by the initial rise method. (a) is a recorded 100 °C TL glow peak, (b) is a plot of the whole data plotted as ln(I) vs. 1/T, (c) and (d) are plots of 10 % of maximum TL intensity, and (e) and (f) are plots of 15 % of the maximum TL intensity.

5.3.4.2. Chen's Peak Shape Method.

Chen's peak shape method was used to estimate the order of kinetics from the shape of the TL glow curve of the prepared phosphor as shown in **figure 5.5**. This method is based on the measurement and calculation of the full width at half

maximum of the peak (ω = T_2 – T_1), the half width at higher temperature side (δ = T_2 - T_m), and the half width at lower temperature side (τ = T_m – T_1) as depicted in **figure 5.5** [17]. From the defined parameters above, the so-called geometrical factor or symmetry factor μ_g can be calculated as in equation 5.2.

$$\mu_g = \frac{\delta}{\omega} = \frac{T_2 - T_m}{T_2 - T_1} \tag{5.2}$$

From equation 5.2, the order of kinetics can be determined from the shape of the TL glow curve and the value of μ_g. The value of μ_g should be close to 0.42 and 0.52 for first and second order respectively [17,18]. In this chapter the value of μ_g was found to be 0.605, suggesting that the studied peak could be of second order kinetic [19].

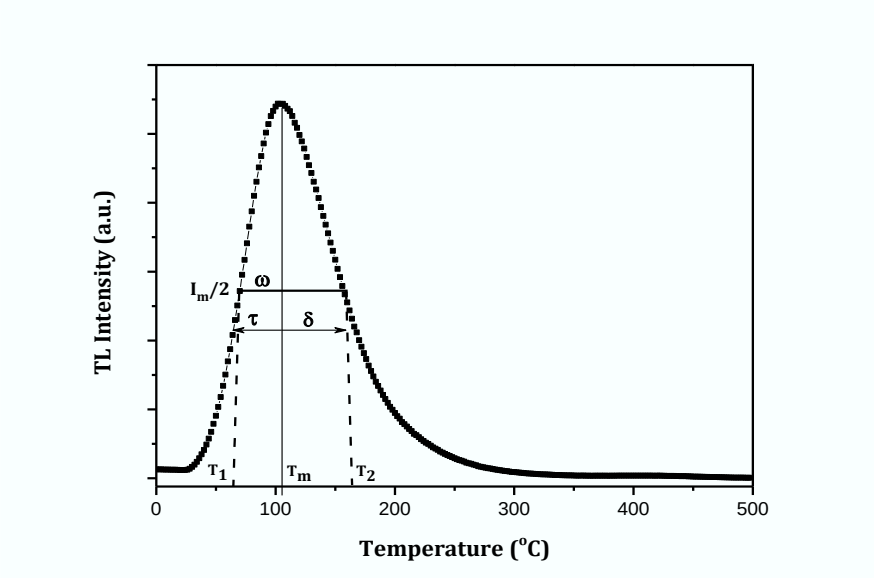

Figure 5.5: A Schematic representation of the peak shape method used for evaluation of the kinetic order.

5.3.4.3. The Variable heating rate method.

The variable heating rate (VHR) method was also used for the calculation of activation energy *E* from the thermoluminescence glow curve of the prepared

phosphor. This is a well-known method that was proposed by Bohum, Porfianovitch and Booth for the evaluation of the activation energy from the first order peak [20,21,22]. The method is based on the fact that, when a linear heating rate β is changed to faster values, both the temperature corresponding to maximum TL intensity T_m and the maximum thermoluminescence intensity I_m change as well. T_m shifts to higher values while I_m shifts to lower values, as evident in **figure 5.6.** The activation energy is then evaluated according to equation 5.3, after repeating the measurement of a TL peak to obtain two temperature maxima T_{m1} and T_{m2} at two different heating rates β_1 and β_2 [17].

$$E = k\frac{T_{m1}T_{m2}}{T_{m1}-T_{m2}}\,In\left[\frac{\beta_1}{\beta_2}\left(\frac{T_{m2}}{T_{m1}}\right)^2\right] \qquad (5.3)$$

K is the Boltzmann's constant. This method was also used in this chapter for evaluation and comparison of the activation energy calculated by other methods, and the activation energy value calculated with this method also presented in Table 5.1, was found to be 0.768 eV.

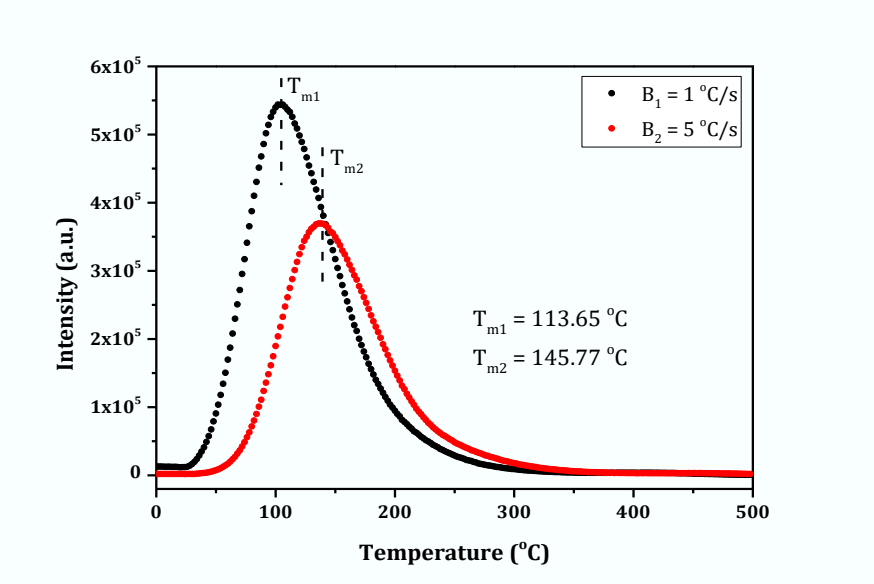

Figure 5.6: The plot of change in both the temperature at maximum intensity T_m and maximum intensity I_m with the heating rate.

5.3.4.4. The Hoogenstraaten's Method

Hoogenstraaten used the variation of heating rate in a slightly different way from the Bohum-Porfianovitch-Booth method discussed in section 5.3.4.3 to evaluate the activation energy *E* and the frequency factor *s* [23]. He suggested the use of several linear heating rates according to equation 5.4,

$$In\left(\frac{T_m^2}{\beta}\right) = \left(\frac{E}{K}\right)\frac{1}{T_m} + In\left(\frac{E}{sk}\right) \qquad (5.4)$$

and a plot of $In\left(\frac{T_m^2}{\beta}\right)$ as a function of $1/T_m$, which according to theory should give a straight line with a slope E/K, from which the activation energy *E* can be calculated. The intercept of this plot at $1/T_m = 0$ gives a value of $In(E/sk)$ from which *s* value can be calculated by replacing E/K with the value obtained from the slope [24]. Although this method was developed strictly for first order kinetics, it has been shown by several researchers to yield results with good accuracy and simplicity regardless of the order of kinetics [17,24]. For these reasons, the Hoogenstraaten method was also adopted in this chapter as demonstrated in **figure 5.7** to calculate the activation energy through the use of several heating rates, and the value obtained also presented in table 5.1, was 0.736 eV.

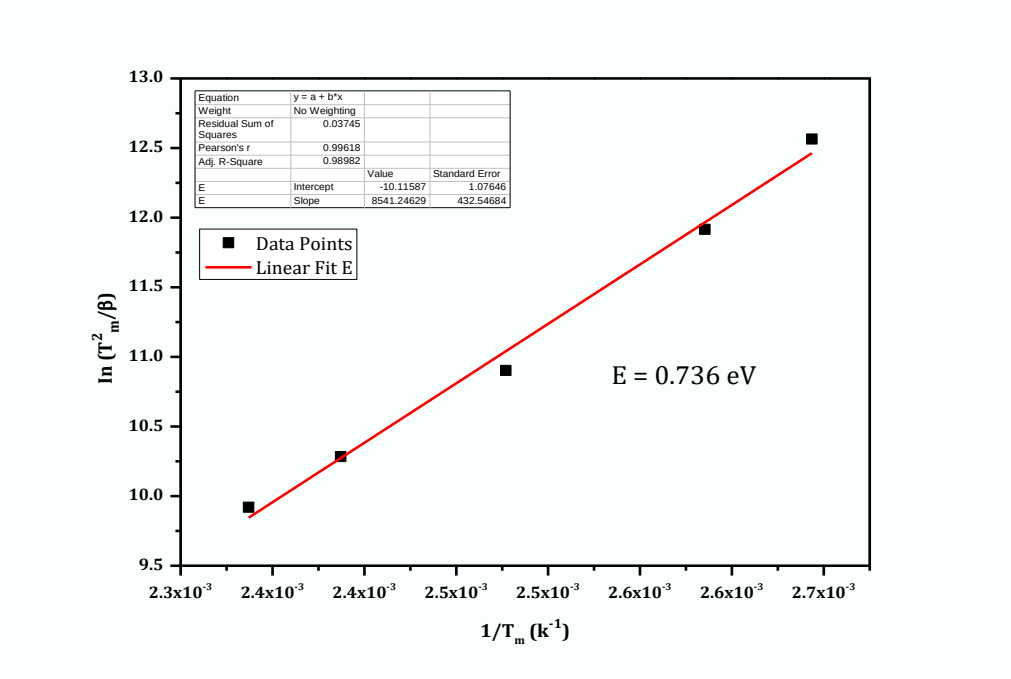

Figure 5.7: *The Hoogenstraaten's Method plotted for calculation of activation energy E.*

Table 5. 1: *Calculated activation energies for a single peak in the 2:1 Sr/Si molar ratio $SrSiO_3/SiO_2$ phosphor prepared by hydrothermal method.*

Method	E (eV)	Q-squared	Frequency factor s (s^{-1})
Initial rise 10 %	0.693	0.989	
Initial rise 15 %	0.733	0.996	
Booth-Bohun-Parfianovitch	0.768		
Hoogenstraaten	0.736	0.989	2.09×10^8

5.4. Conclusions

Thermoluminescence properties of the $SrSiO_3/SiO_2$ phosphor measured after beta irradiation were reported. TL dosimetric properties of this phosphor were also investigated. The TL glow curve measured at 1 $^oC/s$ following beta irradiation at various doses appeared as a simple and single curve. The TL intensities of this sample increased with increasing beta radiation doses. The

obtained variable heating rate results showed that the temperature at maximum intensity increased with the increase of heating rate. The TL kinetic parameters order of kinetic *b*, activation energy (*E*) and frequency factor (*s*) were obtained using the initial rise method, variable heating rate and peak shape method. All these methods yielded comparable activation energy estimates. The observed linearity in the range 0.3 to 2.4 kGy showed that this phosphor can be a potential candidate for the application of personal or environmental dosimetry.

REFERENCES

1. M.Oglakci, M.Topaksu, Y.Alajlani, N.Can, E.Ekdal Karali, Thermal quenching and evaluation of trapping parameters of thermoluminescence glow-peaks of beta irradiated $NaBaBO_3$: Tb^{3+} for TLD applications, Journal of Luminescence Volume 244, (2022) 118731.
2. R.R.Dawam, F.B.Masok, S.B.Fierkwap, Thermoluminescence of secondary peak on synthetic quartz: Influence of annealing time on kinetic parameters and some dosimetric features, Journal of luminescence 233 (2021) 117918.
3. Mahmoud Bakr, and Mohamed Omer, Determination of Thermoluminescence Kinetic Parameters of La_2O_3 Doped with Dy^{3+} and Eu^{3+}, Materials 2020, 13, 1047.
4. D. Joseph Daniel, O. Annalakshmi, U. Madhusoodanan, P. Ramasamy, Thermoluminescence characteristics and dosimetric aspects of fluoroperovskites ($NaMgF_3$:Eu^{2+}, Ce^{3+}), JOURNAL OF RARE EARTHS, Vol. 32, No. 6, Jun. 2014, P. 496.
5. R. Chen, J.L. Lawless, V. Pagonis, On the various-heating-rates method for evaluating the activation energies of thermoluminescence peaks, Radiation Measurements 150 (2022) 106692.
6. R. Cren And S. A. A. Winer, Effects of Various Heating Rates on Glow Curves, Journal of Applied Physics 41, 5227 (1970).
7. Hoogenstraaten, W., 1958. Electron traps in zinc-sulphide phosphors. Philips Res. Rep. 13, 515–693.
8. M.L. Chithambo, V. Pagonis, F.O. Ogundare, Spectral and kinetic analysis of thermoluminescence from manganiferous carbonatite, J. Lumin. 145 (2014) 180–187.
9. T. Rivera Montalvo , C. Furetta , G. Kitis , J. Azorín & R. M. Vite, Radiat. Eff. Defects Solids 159 (2004) 217-222.

10. M. P. Chougaonkar, Munish Kumar and B. C. Bhatt, Testing of Phosphors for their use in Radiation Dosimetry: Detailed Procedure and Protocol, International Journal of Luminescence and Applications Vol. 2(Special Issue: III) November-2012 ISSN: 2277 – 6362.
11. M.S. Rasheedy, A.M.A. Amry, On the frequency factor obtained in case of thermoluminescence second order kinetics, J. Lumin. 63 (1995) 149 –154.
12. Balci-Yegena, M. Yüksela, N. Kucukb, Y. Karabulutc, M. Ayvacikli. Can, M. Topaksu, Thermoluminescence dose and heating rate dependence and kinetic analysis of ZnB_2O_4:0.05Dy^{3+} phosphor, Nuclear Inst, and Methods in physics Research B 416 (2018) 50-54.
13. T. Rivera Montalvo , C. Furetta , G. Kitis , J. Azorín & R. M. Vite, Radiat. Eff. Defects Solids 159 (2004) 217-222.
14. G. F. J. GARLICK and A. F. GIBSON, The Electron Trap Mechanism of Luminescence in Sulphide and Silicate Phosphors, 1948 Proc. Phys. Soc. 60, 574-590.
15. N.S. Rawat , M.S. Kulkarni, D.R. Mishra, B.C. Bhatt, C.M. Sunta, S.K. Gupta, D.N. Sharma, Use of initial rise method to analyze a general-order kinetic thermoluminescence glow curve, Nuclear Instruments and Methods in Physics Research B 267 (2009) 3475–3479.
16. V. Pagonis, G. Kitis and C. Furetta. Numerical and Practical Exercises in Thermoluminescence. Springer, 2006.
17. R. Chen, S.A.A. Winer, Effects of various heating rates on glow curves. J. Appl. Phys. 41(13), 5227–5232 (1970).
18. Dinesh KumarS.M. RaoSupreet Pal Singh, Structural, optical and thermoluminescence study of Dy^{3+} ion doped sodium strontium borate glass, Journal of Non-Crystalline Solids, 464 (2017) 51 – 55.
19. Szymon Swiontek, Marcin Sroda and Wojciech Gieszczyk, Ceramics, Glass and Glass-Ceramics for Personal Radiation Detectors, Radiation Detectors. Materials 2021, 14, 5987.
20. A. Bohum, Czech. J. Phys. 4 (1954) 91.
21. I.A. Porfianovitch, J. Exp. Theor. Phys. USSR 26 (1954) 696.

22. A.H. Booth, Canad. J. Chem. 32 (1954) 214.
23. W. Hoogenstraaten, Philips Res. Rep. 13 (1958) 515.
24. Th Subodh Chandra Singh, P S Mazumdar and R K Gartia, A critical appraisal of methods of various heating rates for the determination of the activation energy of a thermoluminescence peak, J. Phys. D: Appl. Phys. 23 (1990) 562-566.

CHAPTER 6

Photoluminescence and thermoluminescence properties of Manganese doped $BaAl_2O_4$ phosphor

6.1. Introduction

Phosphorescence is defined as a luminescence phenomenon which is emitted by phosphor materials as a result of a radiative forbidden transition of a photo-excited electron between states of distinct spin multiplicities (i.e., from a triplet excited state to a singlet ground state) [1]. At elevated temperatures, thermal quenching is a process through which the decay of phosphorescence phenomenon usually tends to shorten and fall in the order of milliseconds, due to non-radiative transitions, which usually weaken luminescence efficiency [1]. Thermoluminescence, on the other hand, is referred to as a long-lasting luminescence phenomenon, which is observed when a sample which was pre-exposed to some form of ionizing radiation such as ultraviolet light, X-rays, and radioactive radiations emit light following stimulation by heating the sample.

In other words, exposing the sample to ionizing radiation only fills the localized metastable energy levels, also known as traps within the forbidden gap, near the conduction band of the crystal structure with electrons. Heating up the sample triggers the release of electrons from these traps to recombine with holes at or near the valence band with an emission of light of a particular wavelength [2]. Phosphors exhibiting these types of luminescence phenomena have recently received a tremendous attention due to their potential applications in a wide and diverse scope, which include traffic signs, emergency signage, display, decorations, in vivo imaging, sensors, radiation detectors etc. [3,4,5].

In light of these applications, compounds with spinel structures are known, among other classes of host materials to have attracted a great attention of researchers recently, particularly spinel aluminate compounds because of their high luminescence intensity, long afterglow, chemical stability, etc. [6]. $BaAl_2O_4$ is a spinel compound having a stoichiometry of XY_2O_4 form, where X represents the divalent alkaline earth metal ions (Ba^{2+}) and Y the trivalent Al^{3+} ions. The configuration of atoms in their crystal lattices is in such a way that O^{2-} atoms are positioned at the corners forming a close-packed structure (CCP) [7]. Being a normal spinel compound, $BaAl_2O_4$ has its alkaline earth metal ions occupying the tetrahedral sites and Al atoms occupying octahedral sites.

$BaAl_2O_4$ phosphor can be obtained through several synthesis routes. Solid state [8], co-precipitation [9], microwave, sol-gel [10] and combustion [11] are among others which have been reported and widely explored in recent years, with combustion being the simplest and safest method which takes only a few minutes to complete [7]. Mn^{2+} ions can emit light with various wavelengths, depending on the type of spinel matrix in which they are incorporated. For instance, they can emit a yellow luminescence which is a combination of both green and red emission parts of the spectrum due to its d^5 transitions, in particular, the $^4T_1 \rightarrow {}^6A_1$ transition.

This transition is very sensitive to its surroundings, i.e. the number of ligands coordinated to it. A green emission can be observed from Mn^{2+} ions occupying tetrahedral sites in a phosphor material. These sites are known to have weak crystal field strengths, because of which the $^4T_1 \rightarrow {}^6A_1$ transition of Mn^{2+} splits less and emits phosphorescence with shorter wavelengths. On the contrary, a red emission at longer wavelengths can be observed, when Mn^{2+} ions residing in octahedral sites of a spinel matrix experiences strong ligand-field because of high coordination number, which has an effect of decreasing the $^4T_1 \rightarrow {}^6A_1$ transition energy [12].

This means separately, a green or red, or a combination of the two emissions can be obtained from Mn^{2+} ions for different applications if a careful selection of a

host matrix is done. A variety of green-emitting phosphors such as $Ba_3Si_6O_{12}N_2:Eu^{2+}$ [12], $Lu_3Al_5O_{12}$: Ce^{3+} [13], $Gd_2O_2S:Tb^{3+}$ [14], $BaTiO_3:Er^{3+}$ [15] have been developed in the past for a number of diverse applications such as phosphor converted LEDs, biological imaging, temperature sensing etc. However, these are rare-earth activated phosphor materials, and it is common knowledge that, upon comparison to rare-earth based phosphors, rare-earth free phosphor materials are more economic and safe to use. In this chapter, optical properties of a rare-earth free, Mn doped $BaAl_2O_4$ green emitting spinel phosphor are investigated. The phosphorescence spectra (upon blue light excitation) and phosphorescence decay curves were studied. Thermoluminescence glow curves were also studied extensively on the prepared spinel phosphor to explore its potential usage in dosimetry applications. The XPS acquisitions were also performed, the spectra from which confirmations of oxidation states of manganese in the prepared spinel phosphor were obtained.

6.2. Experimental

6.2.1. Sample preparation

A rapid conventional combustion method was used to synthesize the Nano-crystalline, $BaAl_2O_4$: 2%Mn phosphor. Both metal nitrates and urea in solid state were used as reactants and fuel, respectively. 3.0 g of barium nitrate ($Ba(NO_3)_2$, 8.4 g of aluminium nitrate $Al(NO_3)_3.9H_2O$, 4.5 g of Urea (CH_4N_2O) and 0.058 g of manganese nitrate ($Mn_2N_6.4H_2O$), all in their analytical grade were mixed in a fixed stoichiometry based on $Ba_{(0.98)}Al_2O_4:Mn^{2+}_{(0.02)}$ nanophosphor. These precursors were mixed in a crucible until a homogeneous mixture was obtained. The homogeneous mixture was constantly stirred until a paste-like mixture was obtained. A crucible containing the homogeneous mixture was transferred into a pre-heated muffle furnace which was set at 600 ^oC. Shortly after, the mixture boiled, underwent dehydration, and decomposed with the release of gases, which finally combusted spontaneously. After completion of this combustion process (~5 minutes), a porous and greenish nanopowder was obtained and allowed to

cool to room temperature naturally, and ground in an agate mortar to fine final product.

6.2.2. Characterization

X-ray diffraction (XRD) spectrometer equipped with Cu K (30 kV, 15 mA, λ = 1.54 Å) radiation was used at room temperature to investigate the phase and crystallinity of the $BaAl_2O_4$: 2%Mn nanophosphor. The Scans were performed between 10° and 80°, using 0.05° steps and a 0.002°/s scan rate. The morphology of the prepared nanophosphor was studied using the Field emission Scanning electron microscope (FE-SEM). The presence of all elements comprising the sample were confirmed using the Energy-dispersive X-ray spectroscopy (EDS). The oxidation states of Mn in the prepared phosphor was confirmed using X-ray photoelectron spectroscopy (XPS). The phosphorescence excitation and emission spectra were aquired at room temperature with the use of a Jobin Yvon/SPEX Fluorolog®-3 spectrofluorometer, which uses a 450 W Xenon flashing lamp as a photon source and collects phosphorescence through an R928 PMT detector operated at 950 V in a continuous mode. The phosphorescence spectra were collected using a 0.2 s integration time, 3.5 nm bandpass both in excitation and emission paths.

The decay curve of the phosphor was also collected at room temperature from a Jobin Yvon/SPEX Fluorolog®-3 spectrofluorometer by exciting the samples with a Xenon flashing lamp (pulse duration = 20-30 μs) and collecting signals using an R928 PMT detector at 950 V in a photon-counting mode. For the decay curve measurement, the sample was excited at 428 nm, where it optimally absorbs, while monitoring the emission at 512 nm. For steady state and time correlated measurements, a double excitation monochromator (330 nm blazed, 1200 grooves/mm) with a built-in chopper and a double emission monochromator (500 nm blazed, 1200 grooves/mm) were used. Thermoluminescence measurements were carried out from the 512 nm emission using the BG-39 (2 nm) filter.

6.3. Results and discussion

6.3.1. X-ray diffraction studies

Figure 6.1 (a) and (b) presents the X-ray diffraction patterns of the as-prepared $BaAl_2O_4$ and $BaAl_2O_4$: 2%Mn spinel phosphors respectively. Both diffraction patterns in (a) and (b) match well with the hexagonal phase of $BaAl_2O_4$ according to the JCDPS data file no (17-0306). The diffraction peaks marked with a hash (#) symbol in **Figure 6.1** (a) and (b) show traces of $BaAl_{12}O_{19}$ impurity phase in both spinel phosphors. This impurity phase could be a result of a high temperature that is usually attained locally during the combustion synthesis, which tends to induce the $BaAl_{12}O_{19}$ phase which usually starts to emerge at elevated temperatures [11]. The incorporation of Mn ions in $BaAl_2O_4$ did not affect its structure as evident in **Figure 6.1** (b).

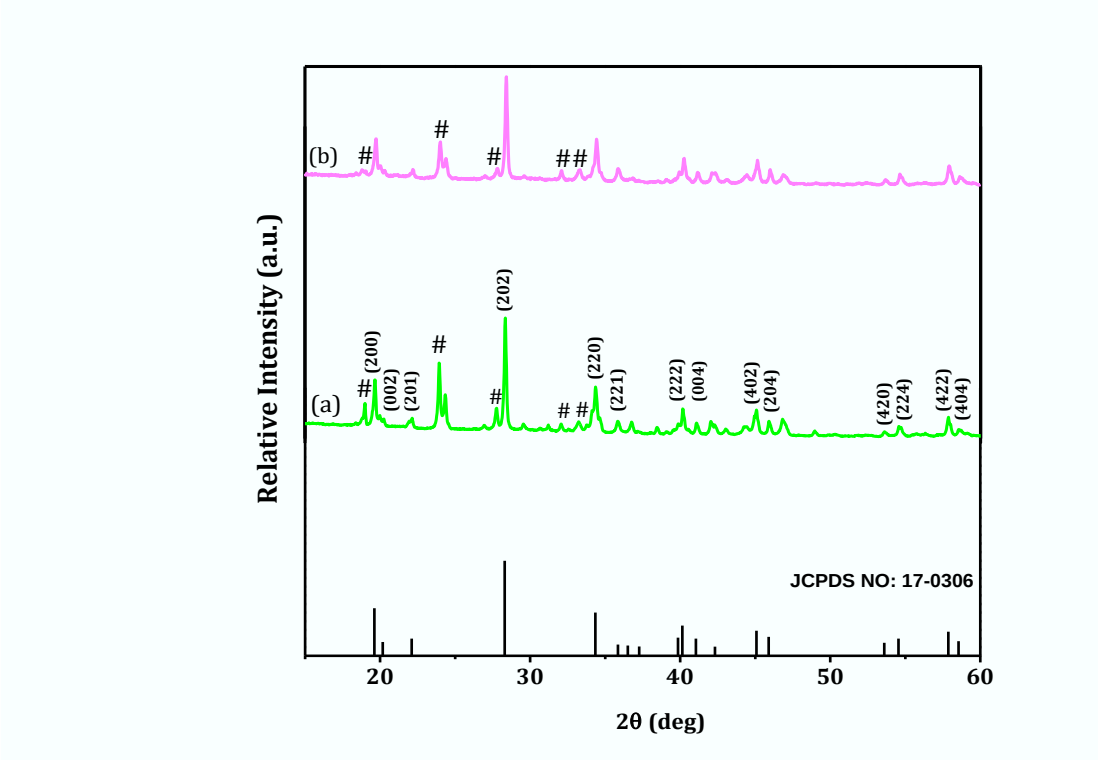

Figure 6.1: Powder X-ray diffraction patterns of the as-prepared undoped $BaAl_2O_4$ (a), and $BaAl_2O_4$: 2%Mn spinel phosphors (b), along with $BaAl_2O_4$ standard file at the bottom.

6.3.2. Scanning electron microscopy and EDX studies

The SEM measurements were carried to acquire the micrographs in order to investigate the surface morphology of the as-prepared $BaAl_2O_4$: 2%Mn spinel phosphor. These micrographs were taken at different magnifications as presented in **Figure 6.2**. Evident from **Figure 6.2** (a) is that the prepared phosphor is of the nano-sheet structure. A higher magnification in **Figure 6.2** (b) reveals an uneven morphology within the sheets with both one (rods) and two (hexagonal sheets) dimensional particles. The heterogeneity of this morphology could be associated with the uneven distribution of both divalent and trivalent ions in the sample. It could also be ascribed to an uneven distribution of temperature and mass flow during combustion process [16]. Pores and voids are a result of gases which escape during the combustion synthesis process.

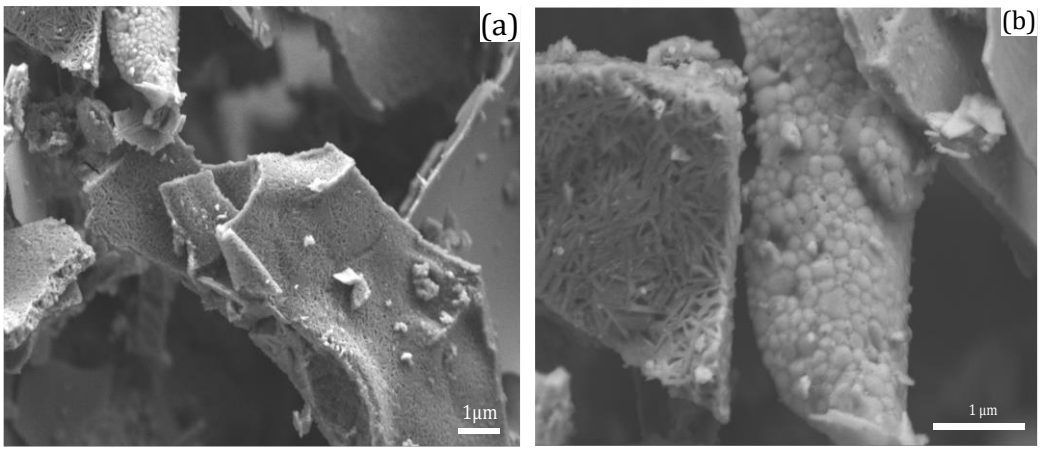

Figure 6.2: Field Emission Scanning Electron Microscope (FE-SEM) images of $BaAl_2O_4$: 2%Mn Phosphor acquired at different magnifications (a) X 9 500 and (b) X 22 000.

Figure 6.3 (a) shows an FE-SEM image together with EDS spectra acquired to confirm the presence of each element in the as-prepared $BaAl_2O_4$: 2%Mn spinel phosphor. The EDS spectra in **Figure 6.3** (a) and (b) are of hexagonal plates and rods particle shapes respectively, and they all confirm the presence of Ba, Al, O,

and Mn in the $BaAl_2O_4$: 2%Mn nanophosphor. It is noted in **Figure 6.3** that Al/Ba ratio is less in table (a) than in table (b). This could be a confirmation of an impurity phase observed in **Figure 6.1**. A similar observation was reported by Wagner and O'keeffe on barium hexaaluminate matrix. A small amount of manganese in Tables 1 and 2, together with low intensities in **Figure 6.3** (a) and (b) are a confirmation that manganese was only incorporated into the $BaAl_2O_4$ host matrix as an impurity.

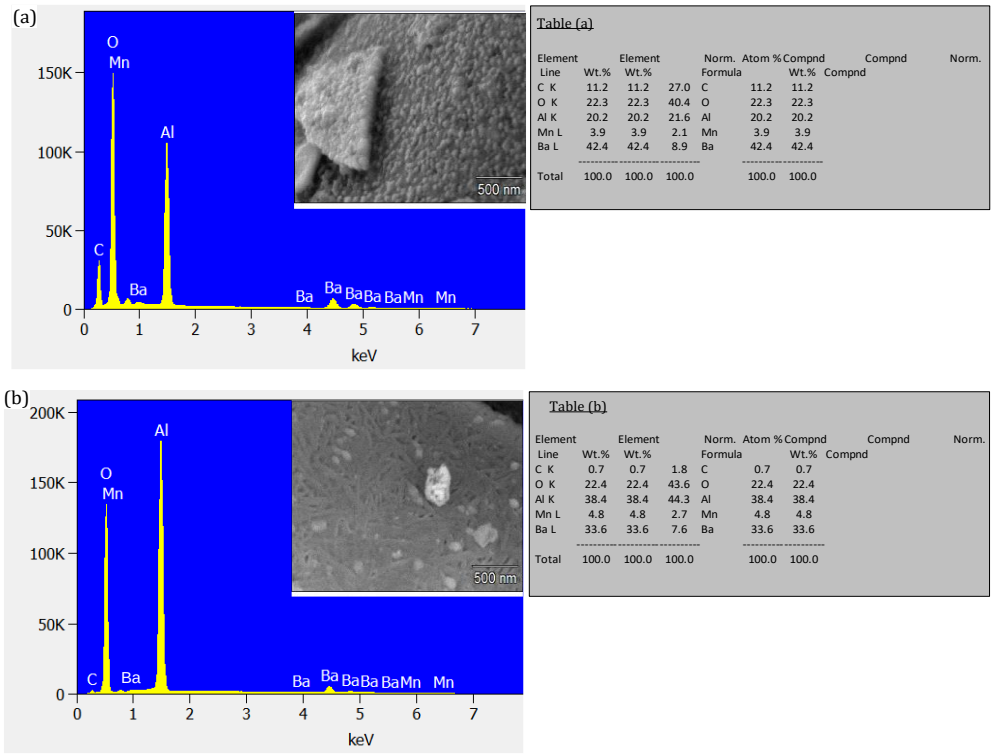

Figure 6.3: EDS spectrum from Ba-rich sites, together with its FE-SEM electron image and table1 showing quantitative results of each element in $BaAl_2O_4$: 2%Mn Phosphor (a). EDS spectrum from Ba-deficient sites, together with its FE-SEM electron image and table 2 showing quantitative results of each element in $BaAl_2O_4$: 2%Mn Phosphor (b).

6.3.3. X-ray photoelectron spectroscopy studies

Elemental analysis on the surface of $BaAl_2O_4$: 2%Mn spinel phosphor was performed after the XPS survey spectrum acquisition presented in **Figure 6.4** (a). As evident in **Figure 6.4** (a), the presence of Ba, Al, O, and Mn were confirmed by

their respective characteristic photoemission peaks. This agrees well with EDS results in **Figure 6.3**. The characteristic photoemission peak of C at 284 eV is due to the carbon tape used during the experiment. Due to a small fraction (2 mol%) of manganese in the $BaAl_2O_4$: 2%Mn spinel phosphor, the characteristic emission peak of Mn was to a lesser extent resolved. The high-resolution spectra in **Figure 6.4** (b), (c), (d), and (e) were also acquired for individual elements Ba 3d, Al 2p, O 1s, and Mn 2p respectively, for doing chemical analysis on the surface of $BaAl_2O_4$: 2%Mn spinel phosphor. As shown in **Figure 6.4** (b), two prominent peaks at 777.5 eV and 792.8 eV which can be attributed to the $3d_{5/2}$ and $3d_{3/2}$ spin-orbit splitting components of Ba respectively were observed. In **Figure 6.4** (c) and (d), two symmetric peaks centered at 71.5 eV and 534.1 eV which are ascribed to Al 2p and O 1s respectively were observed.

Two broad and weak peaks centered at 643.0 and 656.0 eV as shown in **Figure 6.4** (e), were also observed, and these peaks compare well with the reported binding energy values of spin-orbit splitting components Mn $2p_{3/2}$ and Mn$2p_{1/2}$ of Mn^{2+} respectively [17]. Also, a weak peak at 641.4 eV which compare well with the reported characteristic emission peak of Mn^{4+} was also detected [17]. Since the phosphor material in this chapter was synthesized by combustion method, which is a redox kind of a reaction between fuel and a metal nitrate, and Mn is in a 3+ state in the starting materials, it can then be suggested that part of the Mn^{3+} was reduced to a Mn^{2+} by the fuel used, while the other was oxidised to Mn^{4+} during synthesis.

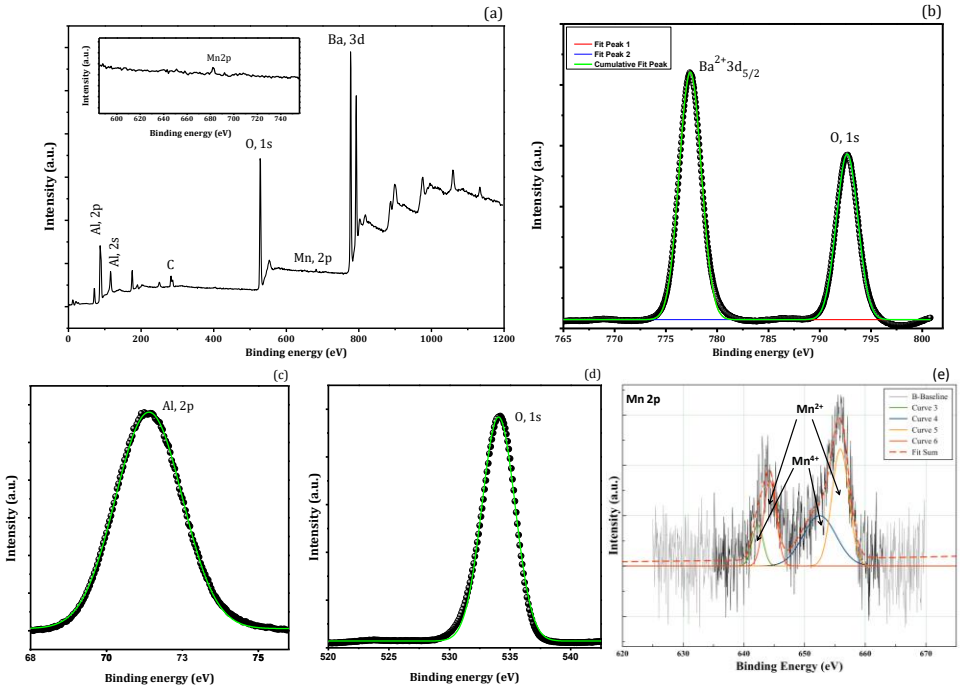

Figure 6.4: XPS survey spectrum of $BaAl_2O_4$: 2%Mn spinel Phosphor (a), along with deconvoluted high-resolution XPS spectra of Ba 3d (b), Al 2p (c), O 1s (d), and Mn 2p (e).

6.3.4. Steady state photoluminescence and Phosphorescence decay curves

Presented in **Figure 6.5** (a) is a phosphorescence excitation spectrum (left) monitored at 512 nm emission wavelength and the emission spectrum (right) of the as-prepared $BaAl_2O_4$: 2%Mn phosphor acquired at room temperature. A weak charge transfer band (CTB) $Mn^{2+} \rightarrow O^{2-}$ peaking at 282 nm [18,19], together with five other bands peaking at 362 nm, 386 nm, 426 nm, 450 nm, and 488 nm, which are ascribed to ${}^6A_1 \rightarrow {}^4E(D)$, ${}^6A_1 \rightarrow {}^4T_2(D)$, ${}^6A_1 \rightarrow [{}^4A_1(G), {}^4E(G)]$, ${}^6A_1 \rightarrow {}^4T_2(G)$, and ${}^6A_1 \rightarrow {}^4T_1(G)$ transitions of Mn^{2+} ions respectively are evident on the excitation spectrum in **Figure 6.5** (a).

The emission spectrum presented on the right hand side of **Figure 6.5** (a) shows a prominent peak at 512 nm, which is attributed to the ${}^4T_1 \rightarrow {}^6A_1({}^6S)$ transition of Mn^{2+} ion [20,21], together with a very weak band peaking at 685 nm, which matches well with the reported Mn^{4+} ion emission from the octahedral sites due

to the $^2E_g \rightarrow {}^4A_{2g}$ transition [22,23], the magnification of which is shown in **Figure 6.5** (c). This emission is reported to be a result of Mn^{4+} ion substituting Al^{3+} ion in the octahedral sites due to comparable ionic radii of the two ions Al^{3+} (r = 0.535 Å) and Mn^{4+} (r = 0.530 Å) [24,25,26]. Furthermore, the detection of Mn^{4+} emission agrees well with the XPS results in **Figure 6.4**, which suggests that part of Mn^{3+} was oxidized to Mn^{4+} during the synthesis process. The excitation spectrum of these Mn^{4+} ions is also shown in **Figure 6.5** (b), in which broad bands cantered at 362, 433 and 483 nm attributed to the $^4A_{2g} \rightarrow {}^4T_{2g}$, $^4A_{2g} \rightarrow {}^2T_{2g}$, and $^4A_{2g} \rightarrow {}^4T_{1g}$ transitions respectively were observed.

Figure 6.5 (d) presents a phosphorescence decay curve of the $BaAl_2O_4$: 2%Mn spinel phosphor monitored at 512 nm. The curve was best fitted using the bi-exponential model in equation 6.1, and the fitting parameters are also shown in **Figure 6.5** (d).

$$I(t) = A + B_1 \exp(-t/T_1) + B_2 \exp(-t/T_2) \qquad (6.1)$$

$\boldsymbol{I}$ represents the phosphorescence intensity, A is a background offset, B_1 and B_2 are both pre-exponential functions relating to how much of an emitting species there is in a material, t is time, and T is the lifetime of phosphorescence. As evident from the SEM micrographs, the prepared phosphor is composed of both nanorods and nanosheets. This means that the Mn ions are emitting from two unlike environments in the $BaAl_2O_4$: 2%Mn phosphor, therefore due to the heterogeneity of the $BaAl_2O_4$: 2%Mn spinel system and the multiexponential decay nature of the Mn ions, the average lifetimes are necessary to determine the average amount of time it takes for Mn ions in their excited states in the $BaAl_2O_4$: 2%Mn spinel phosphor. As such, the amplitude-average lifetime [24] in equation 6.2 was used to calculate the average lifetime τ_{ave} of Mn^{2+} ions in their excited states, and the value of 4.88 ms was obtained.

$$\tau_{ave} = \sum_{i=1}^{n} B_i T_i \qquad (6.2)$$

where B and T still have the same meanings as in equation 6.1.

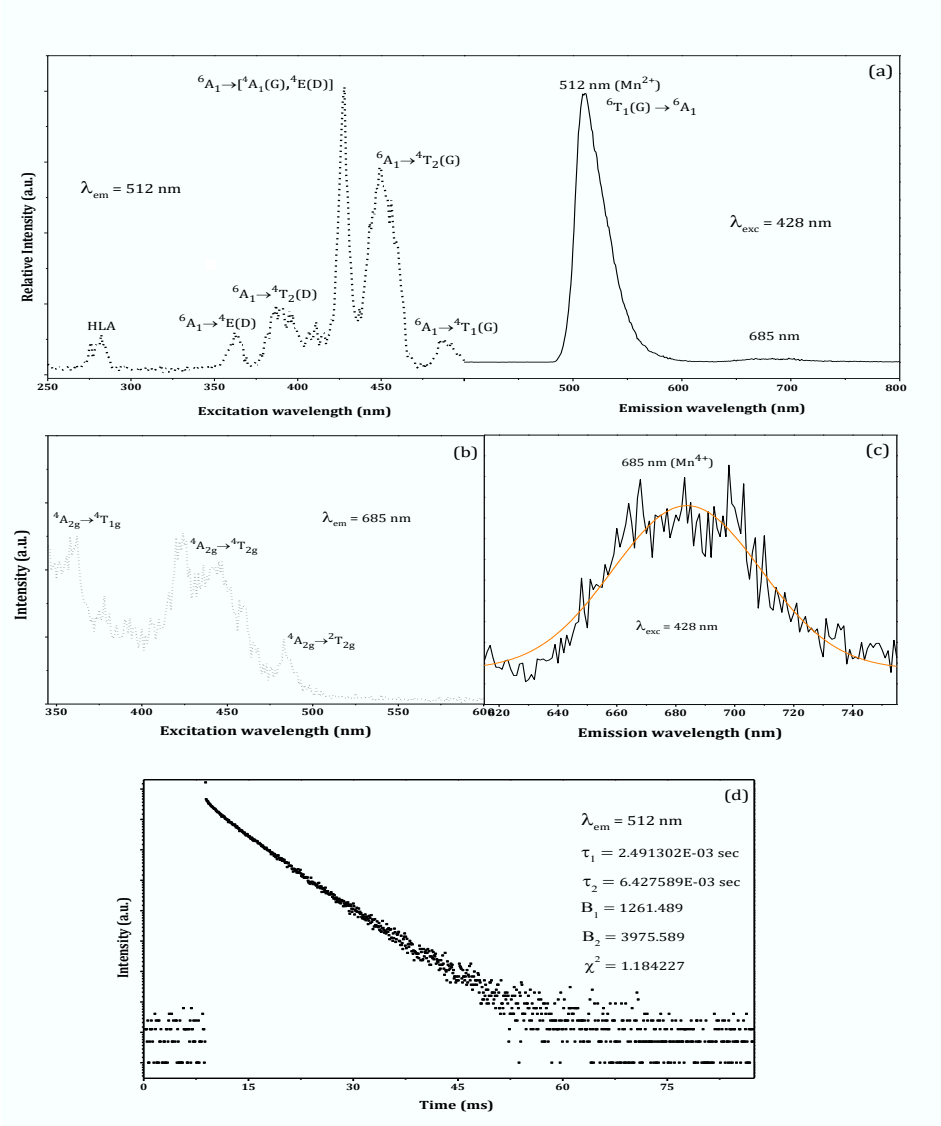

Figure 6.5: Phosphorescence excitation spectrum (left), and emission spectrum (right) of Manganese ions in the $BaAl_2O_4$: 2%Mn spinel phosphor acquired at room temperature, both plotted on a linear scale. (b) the excitation spectrum associated with the 685 nm emission of Mn^{4+} ions. (c) is a magnification of the 685 nm of Mn^{4+} emission observed in (a), also plotted on a linear scale. (d) is a decay curve associated with the 512 nm emission of $BaAl_2O_4$: 2%Mn phosphor acquired at room temperature, plotted on a logarithmic scale.

The quality of green phosphorescence emitted by the $BaAl_2O_4$: 2%Mn spinel phosphor was aslo evaluated from the Commission International del' Eclairage (CIE) 1931 chromaticity coordinates (x, y). The coordinates obtained from the emission spectra after a 428 nm excitation are presented in figure 6.6. The CIE coordinates of this spinel phosphor were found to be (0.150, 0.730), which correspond with a color temperature calculated using equation 4.1 to be 8231 K.

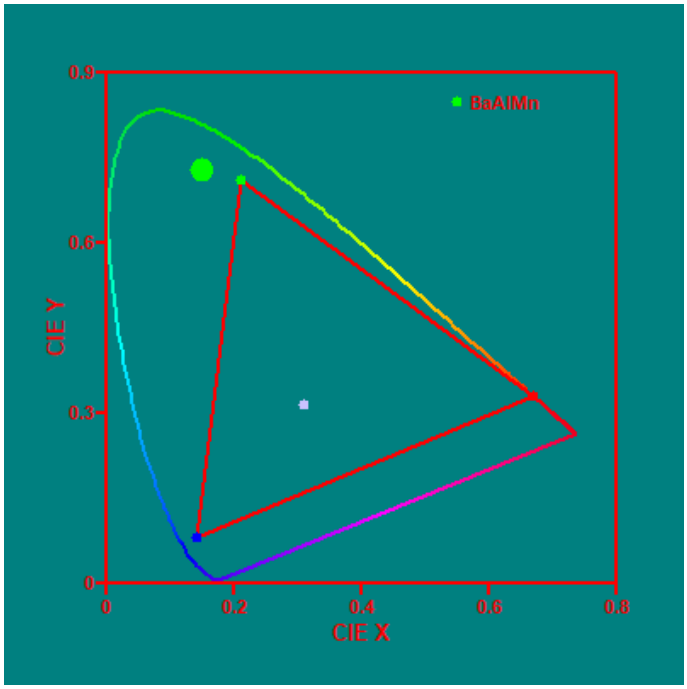

Figure 6.6: The CIE 1931 chromaticity coordinates of $BaAl_2O_4$:2%Mn phosphor prepared by combustion method. The white circle inside the red plot triangle represents white light. CIE coordinates presented here were calculated using the software GoCIE obtained from http://www.geocities.com/krjustin/gocie.html.

6.3.5. Thermoluminescence Studies

6.3.5.1. *General properties of a glow curve of $BaAl_2O_4$: 2%Mn spinel phosphor*

Figure 6.7 (a) presents a glow curve of $BaAl_2O_4$: 2%Mn spinel phosphor material acquired at a constant heating rate of 2.5 $^oC/s$ after a beta irradiation of 180 Gy. Evident on this glow curve is at least one prominent peak at around 114 ^oC labelled peak (I), together with two weak ones at about 186 ^oC and 292 ^oC labelled peak (II) and peak (III) respectively. These two peaks are of very weak intensities and do not show high sensitivity at low doses, as such, all the analysis in this

section were performed only on the prominent peak. Furthermore, due to the complexity of this glow curve, it was necessary to isolate the individual peaks mentioned above before the analysis on the main peak (peak I) was carried out. The isolation of peaks was carried out using partial thermal cleaning method [28,29].

Using this method, a sample irradiated to 180 Gy at ambient temperature was heated at a linear heating rate of 2.5 ^{o}C/s to a temperature of 165 ^{o}C, which is just beyond the peak maximum of the first peak to remove it (empty traps responsible for it), followed by cooling back to ambient temperature. The sample was then re-heated to 500 ^{o}C with the same heating rate within the remaining temperature range of the remaining peaks without irradiation to record the whole glow curve. The obtained glow curve was then composed of the remaining two peaks (I and II) as presented in the insert I of **Figure 6.7** (a). The same procedure was followed with the sample heated to a cleaning temperature of 250 ^{o}C to separate the peaks in the insert 1 of **Figure 6.7** (a) and remain with the one in the insert 2 of **Figure 6.7** (a).

Also noticed after isolation of peak (I) by thermal cleaning method, was that this peak looks broad and with a decrease in Intensity. This peak could be a combination of several components embedded within one peak, making it appear as one broad peak. This behaviour was reported to be due to the presence of a sequence of electron traps in a thermoluminescent material [30].

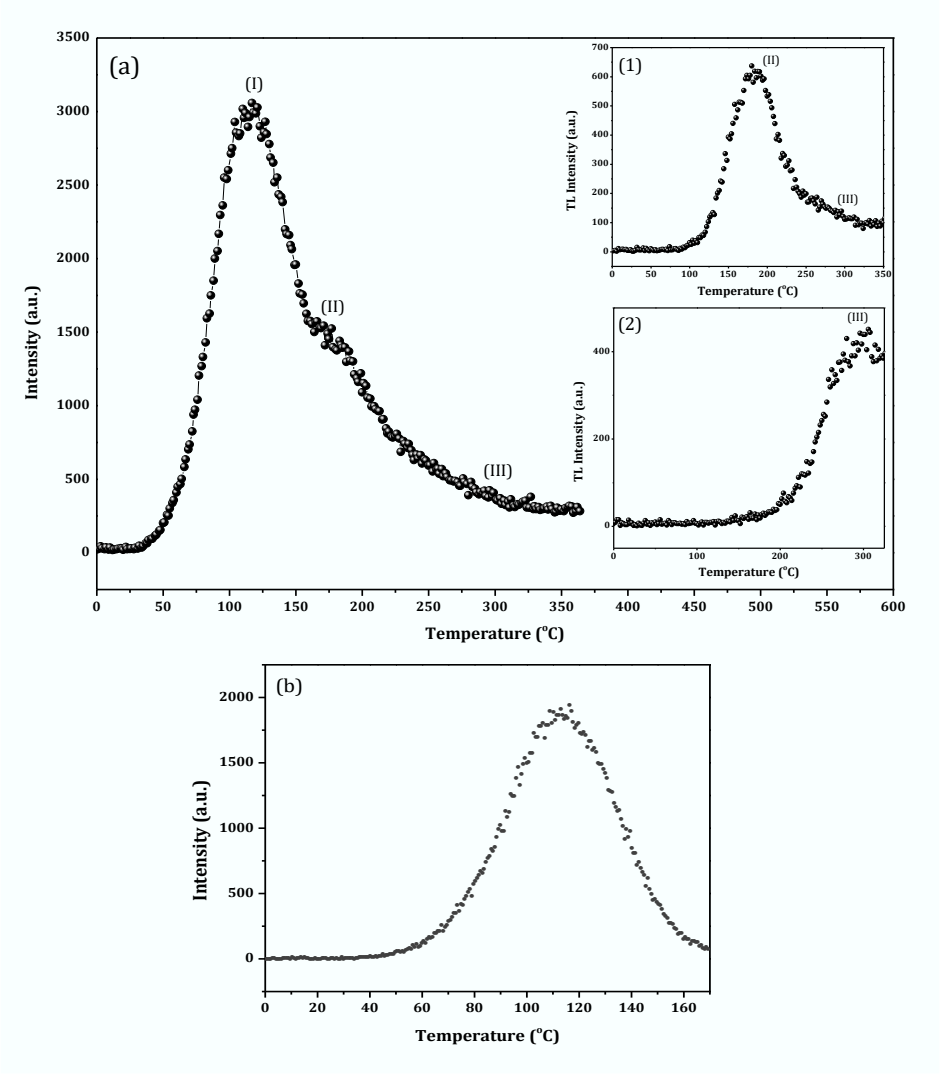

Figure 6.7:A glow curve of $BaAl_2O_4$: 2%Mn spinel phosphor acquired at a constant heating rate of 2.5 °C/s after a beta irradiation of 180 Gy (a), before thermal cleaning with all three peaks (I, II, and III) present. The insert (I) shows two remaining peaks (II and III) after removal of peak (I) by thermal cleaning. Insert (II) represent the last peak (III) after the removal of the two peaks (I and II) by thermal cleaning. A glow curve showing an isolated peak (b).

A plot of thermoluminescence response as a function of irradiation dose ranging from 30 Gy to 480 Gy is shown in **Figure 6.8**. From the acquired measurements at a constant heating rate of 2.5 °C/s, it was noted as evident in **Figure 6.8** (a) and (b) that the TL intensity increases with an increase in dose without saturation in this region. Also, a shift of the temperature at maximum TL intensity T_m to higher temperatures at low doses and to lower temperatures at higher doses are evident in **Figure 6.8** (c). This is because, as the dose is increased, so does the pre-

exponential factor, which then shifts the thermoluminescence peak to lower temperatures [31]. It is known from theory that for a first order TL glow peak, the location of temperature at maximum T_m is independent of the change in irradiation dose [32], therefore the observation of a shift in **Figure 6.8** suggest that this peak is a non-first order peak.

It is also known from literature that for a first order peak, T_m does not shift with the variation of dose [33]. It can therefore be inferred from this typical Garlick-Gibson behavior of a second order TL peak [34,35] that the studied peak in this chapter is a non-first order peak. The re-trapping process dominates the recombination one in the emission process responsible for a second order peak. In other words, a considerable amount of the released electrons tends to get re-trapped prior to recombining at recombination centers, thereby causing both a delay in thermoluminescence emission and distribution of thermoluminescence emission over a broad temperature range [35].

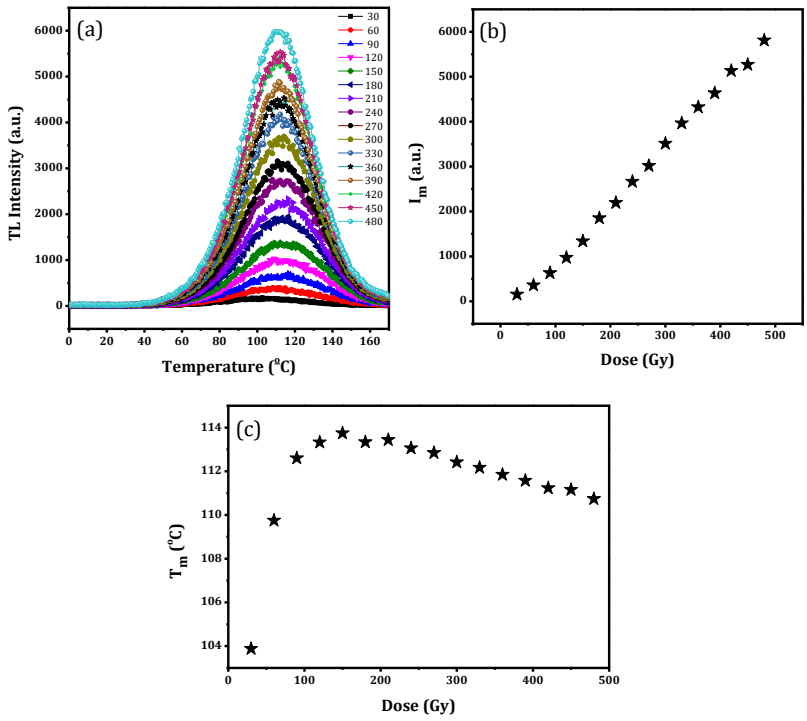

Figure 6.8: The dependence of TL Intensity I_m (a) and (b), and temperature at maximum intensity T_m (c) of $BaAl_2O_4$: 2%Mn spinel phosphor on irradiation dose at a constant heating rate of 2.5 °C/s.

Figure 6.9 presents the acquired thermoluminescence measurements of $BaAl_2O_4$: 2%Mn spinel phosphor at different linear heating rates from 0.5 to 5 $^oC/s$.These measurements were acquired in order to understand the effect of heating rate, β on the glow curve of the $BaAl_2O_4$: 2%Mn spinel phosphor. Figure 6.9 (a) and (b) presents the glow curves from both measured and the normalized data respectively. **Figure 6.9** (c) and (d) represent peak temperature at maximum intensity T_m and TL intensity at maximum I_m as a function of heating rate respectively. Evident from **Figure 6.9** (a) is that, as expected from theory, the temperature at maximum T_m shifts to higher temperatures with the increase in heating rate. Also noted in **Figure 6.9** (a) and (e) is that the TL intensity together with area under TL curve seem to increase with an increasing heating rate, which is inconsistent with thermoluminescence theory.

This inconsistency, also known as the anomalous, inverse heating-rate effect was previously observed by other researchers [36,37]. These researchers believe it to originate from a competition between non-radiative and radiative pathways in thermoluminescent materials. Based on this simultaneous thermal release of charge carriers (electrons and holes), when the heating rate is increased, the TL peak shifts to elevated temperatures, and more holes move through the valence band to the radiative recombination center, thereby contributing to the radiative transition. This then results in both the peak area and maximum intensity to increase with an increase in heating rate.

However, other researchers have a contrasting sentiment on this behaviour of the peak area and maximum intensity. For instance, Gonzalez et al. [38] reported that a true representation of a glow curve as a function of heating rate is the one in which the TL intensity is normalized to the heating rate used (TL/β). Their argument was that normalization must be done because the visual change of the total glow curve area depends only on the units used on TL axis, which is usually in arbitrary units (a.u.). So, after normalization (by dividing each TL data by its corresponding heating), it then becomes clear that the TL intensity together with

the area under TL curve decrease with the increase in the heating rate as evident in **Figure 6.9** (e).

Also, noted in **Figure 6.9** (d) is a decrease in thermoluminescence intensity of the main peak as a function of heating rate. This is a clear evidence that this peak is affected by thermal quenching, a process due to which the TL efficiency η_{TL} in equation 6.3 [2] is suppressed as temperature rises.

$$\eta_{TL} = \frac{P_r}{P_r + P_{nr}} \tag{6.3}$$

where P_r is the probability of luminescence transitions, which unlike the probability of non-radiative transitions P_{nr}, is temperature independent. At elevated temperatures, the competition between radiative and non-radiative transitions tend to favor the non-radiative transitions and this suppresses luminescence efficiency, hence a decrease in TL intensity [2].

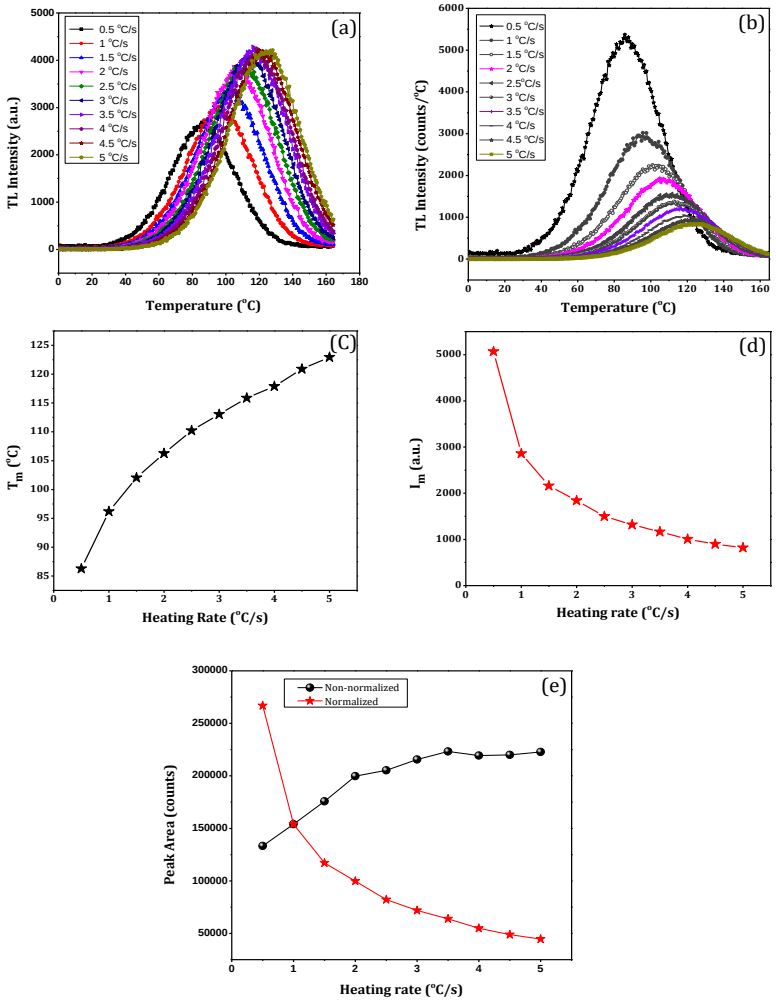

Figure 6.9: The effect of heating rate on TL glow curves for $BaAl_2O_4$: 2%Mn spinel phosphor exposed to a 180 Gy beta dose. (a) is the obtained raw experimental data, while (b) is the normalized TL data. (c) and (d) are the temperature at maximum (T_m) and TL intensity at maximum (I_m) respectively as functions of heating rate. (e) shows the peak are as a function of heating rate.

6.3.5.2. *Kinetic analysis of a TL glow curve of $BaAl_2O_4$: 2%Mn spinel phosphor*

To comment on the order of kinetics and activation energies, a glow curve was plotted for the calculations of activation energies as shown in Table 6.1 using Chen's peak shape method [35] in **Figure 6.10** (a), together with the initial rise method in **Figure 6.10** (b) and (c). In the Chen's method, the main components are the temperature at the maximum TL intensity T_m, and the temperatures (T_1 and T_2) on either side of T_m as presented in **Figure 6.10** (a). These components are used

to determine the glow curve shape parameters such as half width of the ascending part of the glow curve (τ), half width of the descending part of the glow curve (δ), and the total half width (ω). From these parameters, the value of the symmetry factor (μ), from which information about the order of kinetics of the TL glow curve can be known is then determined. In this chapter, T_1, T_2, and T_m were found from experimental data to be 357.19 K, 404.79 K, 380.82 K respectively. Once the order of kinetics is established, the activation energy E can then be determined using Chen's general formula in equation 6.4.

$$E = c_\gamma\left(\frac{kT_m^{\,2}}{\gamma}\right) - b_\gamma\left(2kT_m\right) \tag{6.4}$$

where γ stands for τ (T_m - T_1 = 286.63 K), δ (T_2 - T_m = 23.97), or ω (T_2 - T_1 = 47.60). From these parameters, the symmetry factor was calculated as $\mu = \delta/\omega$ = 0.503, which is consistent with the theoretical value for a second-order TL peak (μ = 0.52) [2,39]. It is also known that, when applying Chen's equation for second-order kinetics, c_ω, c_τ, and c_δ values are 3.54, 1.81, and 1.71 respectively, and those of b_ω, b_τ, and b_δ are 1, 2, and 0 respectively [35]. Therefore, the activation energy can be calculated from Chen's equation in terms of ω, τ and δ as shown in equation 6.5 to 6.7 and the results are shown together with the one that was calculated using the initial rise method in table 6.1.

$$E = 3.54\left(\frac{kT_m^2}{\omega}\right) - 2kT_m \tag{6.5}$$

$$E = 1.71\left(\frac{kT_m^2}{\delta}\right) \tag{6.6}$$

$$E = 1.81\left(\frac{kT_m^2}{\tau}\right) - 2\left(2kT_m\right) \tag{6.7}$$

The activation energy calculated from different methods as shown in table 6.1 has an average value of 0.84 eV. This is the depth of the shallow trap responsible for the luminescence from the $BaAl_2O_4$: 2%Mn spinel phosphor.

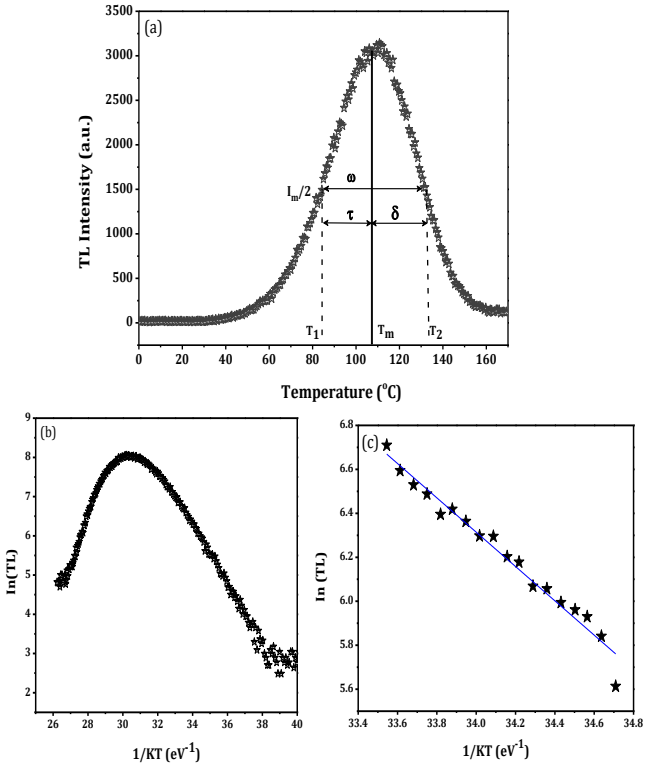

Figure 6.10: TL glow curves of $BaAl_2O_4$: 2%Mn spinel phosphor plotted for activation energy calculations using (a), the peak shape method, and (b), and (c), the initial rise method.

Table 6. 1: *Calculated Activation energies (E in eV) of the prominent peak using Chen's and the initial rise method.*

Method	E(eV)
Chen's using δ	0.891
Chen's using ω	0.863
Chen's using τ	0.826
Initial rise	0.780 ± 0.033

6.4. Conclusions

Manganese-doped $BaAl_2O_4$ spinel phosphor was synthesized using combustion method and structural, phosphorescence, thermoluminescence, and elemental

chemical composition properties were extensively investigated. SEM studies revealed the $BaAl_2O_4$: 2%Mn spinel phosphor to be of uneven morphology with both nano-rods and hexagonal sheets particles. The XPS studies revealed the characteristic emission peaks of Mn^{4+}, which suggested the oxidation of some fraction of Mn to Mn^{4+} during the synthesis. After a 428 nm excitation, the $BaAl_2O_4$: 2%Mn phosphor exhibited a strong green (512 nm) and a week red (685 nm) emissions, showing that the prepared phosphor has a potential as a green primary colour in displays technologies. Both the 512 nm and 685 nm emissions were interpreted originate from Mn^{2+} and Mn^{4+} ions respectively. Thermoluminescence studies showed a linear correlation between thermoluminescence intensity and dose, which makes $BaAl_2O_4$: 2%Mn spinel phosphor a potential candidate for dosimetry use.

REFERENCES

1. Ru-Shi Liu, Phosphors, Up Conversion Nano Particles, Quantum Dots and Their Applications**:** Volum2, Springer+Business Media, Singapore, 2016.
2. C. Furetta, Handbook of Thermoluminescence, World Scientific, 2010.
3. A. Bessie´re, S. K. Sharma, N. Basavaraju, K. R. Priolkar, L. Binet, B. Viana, A. J. J. Bos, T. Maldiney, C. Richard, D. Scherman, and D. Gourier, Chem. Mater. 26, 2014, 1365−1373.
4. T. Luan, J. Liu, X. Yuan, and J. G. Li, Res. Lett. 12, 2017, 219.
5. R. Ianoş, R. Lazău, R. C. Boruntea, Ceram. Int. 41, 2015, 3186-3190.
6. M. Ayvacikli, Spectrosc. Lett. 47, 2014, 504-511.
7. A. Salehabadi, M. Salavati-Niasari, F. Sarrami, A. Karton, Renew. Energy. 114, 2017, 1419-1426.
8. H.Roh, I.Cho, J. An, C. M. Cho, T. H. Noh, D. K. Yim, D. Kim, K. S. Hong, Ceram. Int. 38, 2012, 443–447.
9. B. Cheng, L. Fang, Z. Zhang, Y. Xiao, and S. Lei, J. Phys. Chem. C. 115, 2011, 1708–1713.
10. R.J. Wiglusz, T. Grzyb, Opti. Mater. 36, 2013, 539–545.
11. L. C.V. Rodrigues, J. Hölsä, J. M. Carvalho, C. C.S. Pedroso, M. Lastusaari, M. C.F.C. Felinto, S. Watanabe, H. F. Brito, Physica B 439, 2014, 67–71.
12. Chenxia Li, Hong Chen, Shiqing Xu, Optik 126, 2015, 499–502.
13. M.J.Lee1S.H.Park1Y.H.Song1E.K.JiU.B.HumayounD.B.LeeD.H.Yoon, Materials Letters 161, 2015, 708–711.
14. Can He, Zhiguo Xia, Quanlin Liu, Optical Materials 42, 2015, 11-16.
15. Dhananjay Kumar Singh, J. Manam, Ceramics International 44, 2018, 10912–10920.
16. H.W. Nesbitt And D. Banerjee, J. Am. Mineral. 83(3-4), 1998, 305–315.
17. Z. C. Feng, Handbook of Solid-State Lighting and LEDs, CRC Press, 2017.
18. X Li, X Tang, Z Wang, Z Zou, J Zhang, Z Ci, Y Wang, Persistent luminescence properties and trap characteristics of an orthosilicate phosphor: LiGaSiO4:Mn2+, J. Alloy. Compd. 721, 2017, 512–519.

19. R.J. Xie, Y.Q. Li, N. Hirosaki, H. Yamamoto, Nitride Phosphors and Solid-State Lighting, CRC Press, New York, 2016.
20. C. Karr, Infrared and Raman Spectroscopy of Lunar and Terrestrial Minerals Academic Press, New York, 2013.
21. R. Cao, Z. Shi, G. Quan, T. Chen, S. Guo, Z. Hu, P. Liu, J. Lumin. 188, 2017, 577–581.
22. A Fu, L Zhou, S Wang, Y Li, DYES PIGMENTS 148, 2018, 9–15.
23. V. Singh, V. Natarajan & Dong-Kuk Kim, Radiat Eff Defects, 2008, 199-206.
24. D. Chen, Y. Zhou, W. Xu, J. Zhong, Z. Ji and W. Xiang, J. Mater. Chem. C 4, 2016, 1704-1712.
25. A Fu, L Zhou, S Wang, Y Li, Dyes Pigm. 148, 2018, 9–15.
26. A Sillen and Y Engelborghs, J. Photochem. Photobiol. 67(5), 1998, 475–486.
27. K.H Nicholas and J. Woods , Br. J. Appl. Phys. 15, 1964, 783.
28. A Necmeddin Yazici, J. Phys. D: Appl. Phys. 38, 2005, 3860.
29. Sunil Thomas, M.L. Chithambo, Radiation Measurements 120, 2018, 83-88.
30. R. Chen, J.L. Lawless, V. Pagonis, Radiat. Meas. 115, 2018, 1–6.
31. A.J.J. Bos, Radiat. Meas. 41, 2007, S45–S56.
32. M.S. Rasheedy, A.M.A. Amry, J. Lumin. 63, 1995, 149 –154.
33. R Chen, S. W. S. McKeever, Theory of Thermoluminescence and Related Phenomena, World Scientific, Singapore, 1997.
34. S. W. S. McKeever, Thermoluminescence of Solids, Cambridge University Press, Newyork, 1988.
35. A. Mandowski, A.J.J. Bos, Radiation Measurements 46, 2011, 1376-1379.
36. R. Chen, V. Pagonis, Radiation Measurements 106, 2017, 20-25.
37. E. Cruz-Zaragoza, P.R.Gonza´lez, J.Azorı´n, C. Furetta, Appl. Radiat. Isot. 69, 2011, 1369–1373.
38. M.L. Chithambo, V. Pagonis, F.O. Ogundare, J. Lumin. 145, 2014, 180–187.
39.

CHAPTER 7

Summary and Conclusion

The undoped $SrSiO_3/SiO_2$ and manganese doped $BaAl_2O_4$ phosphors were synthesized, and their luminescence properties were studied and evaluated for white phosphorescence, dosimetry, and persistent luminescence applications. The prepared phosphors were proven by FTIR and XRD measurements to be of a mixed-phase nature with grain size averaged by Scherrer equation to be below 34 nm. The SEM measurements on the prepared phosphors were carried out and silicate phosphors revealed spherical nono-particles with agglomeration and non-uniform distribution of particle size, while aluminate phosphors showed mixed shapes with rods and hexagonal phases with barium-rich and barium-deficient lattice sites. The EDS measurements demonstrated an even distribution Sr, Si, and O in the silicate phosphors and Ba, Al, and O in the aluminate phosphor. Photo and thermoluminescence properties of the aluminate and silicate phosphors prepared at different Sr/Si molar ratios were investigated. An intense white room temperature phosphorescence (495 and 687 nm) with CIE color coordinates 0.260, 0.330 and 0.270, 0.330 was obtained from the silicate samples of 1:1 and 2:1 molar ratio prepared by coprecipitation method. These emissions close to natural white light prove these two samples to be good candidates for applications in solid state lighting and signaling. A green phosphorescence at 512 nm was observed on the aluminate phosphor which originated from the $^4T_1 \rightarrow {}^6A_1({}^6S)$ transition of Mn^{2+} ion. This phosphorescence with color temperature of 8231 K also makes this phosphor a potential candidate for solid state lighting and persistent luminescence. Thermoluminescence studies also showed a linear correlation between TL and dose, proving the prepared silicate phosphors to have a potential in dosimetry applications. Upon beta irradiation of the 2:1 Sr/Si molar ratio sample prepared by hydrothermal method at different doses, TL intensity increased linearly with increasing beta radiation doses, proving

potential dosimetry application in this phosphor. The emission of this phosphor was also found to fall within a 400-500 nm emission range, which makes it a potential candidate in dosimetry application. The TL kinetic parameters in this phosphor, order of kinetic *b*, activation energy (*E*) and frequency factor (*s*) were obtained using the initial rise method, variable heating rate and peak shape methods.

Key Terms:

Alkaline silicates, Intrinsic defects, Photoluminescence, Phosphorescence, Phermoluminescence, Decay curve, Thermal quenching, inverse heating-rate effect, Energy transfer, Thermal cleaning.

Future Prospects

Tremendous interest was aroused recently by silicate phosphors emitting blue, green, red and a combination of these three colors due to their potential usage in LEDs, fluorescent lamps, signaling etc. A common way of obtaining these types of materials is by doping host materials with rare-earth and transition metals which are environmentally unfriently. Moreover, reare-earths are costly and require chemical refinement and purification prior to their usage, which comes with a price of increasing their production cost, which in the end increases the cost of rare-earth based materials such as WLEDs. For these reasons, the search for rare-earth free phosphors emitting the colors mentioned above is crucial.

Luminescence from these types of materials can be optimized through optimizing a distribution of defects in them during synthesis processes. It would be interesting in this study to investigate the behavior of Si-O defects, together with oxygen vacancies as quenchers in the prepared materials at further lower strontium content. Furthermore, it would be of much interest to further improve the white light from the 1:1 and 2:1 molar ratio samples with CIE coordinates of 0.270, 0.330 and 0.260, 0.330 respectively due to their closeness to the neutral white light (0.330, 0.330). Apart from modulation of reaction conditions such as reaction time, reaction temperature, and PH of the solution, it would be interesting to utilize additives such as surfactants with different functional groups (hydroxyl groups, amine groups, thiol groups etc.) to control the surface energy of the prepared materials and thereby control the distribution of the Si-O and oxygen vacancies during synthesis. It would be also interesting to further utilize these surfactants to modulate the shapes of these two phosphors in order to control the interaction between the defects mentioned above and thereby improve the white light from them.

Acronyms

TL	Thermoluminescence
PL	Photoluminescence
PMT	Photomultiplier tube
WLEDs	White light emitting diodes
XRD	X-ray diffraction
FTIR	Fourier transform infrared spectroscopy
SEM	Scanning electron microscope

PUBLICATIONS

- Dependence of manganese phosphorescence on crystal lattice sites of spinel aluminate hosts.
- Photoluminescence and thermoluminescence properties of Manganese doped $BaAl_2O_4$ phosphor.